Winter 1-1-2012

New MRI Techniques for Nanoparticle Based Functional and Molecular Imaging

Lingzhi Hu
Washington University in St. Louis

WASHINGTON UNIVERSITY IN ST. LOUIS
Department of Physics

Dissertation Examination Committee:
Samuel A. Wickline, chair
Mark S. Conradi
Joel Garbow
James G. Miller
Stuart A. Solin
Dmitriy Yablonskiy

New MRI Techniques for Nanoparticle Based Functional and Molecular Imaging

by

Lingzhi Hu

A dissertation presented to the
Graduate School of Arts and Sciences
of Washington University in
partial fulfillment of the
requirements for the degree
of Doctor of Philosophy

December 2012

Saint Louis, Missouri

Contents

List of Figures

List of Tables

Acknowledgement

First and foremost I offer my sincere gratitude to my advisor, Dr. Samuel Wickline. I attribute this thesis to his enormous encouragement and support. He led me to this exciting interdisciplinary research field and mentored me in various aspects – medicine, biology, medical imaging, physics, language, presentation skills and more. Most importantly, he is always open-minded and supportive and provides substantial guidance for me every time when I started exploring new research projects. I appreciate all his contributions of time, ideas, and funding to make my PhD experience productive and unforgettable. I'm also deeply thankful for his flexibility and openness to allow me to explore the outside by myself which could broaden my horizon and prepare me for future challenges.

I am very grateful for all the help that Dr. Junjie Chen gave me during my PhD research. He is a very hands-on scientist and knowledgeable mentor, who provided me valuable advices on general research directions and specific experimental details. His working spirit will always inspire me to develop solid laboratory skills and conduct concrete scientific investigations.

I would also like to offer my deep appreciation to Dr. Mark Conradi. My original understanding of MR physics comes from his excellent MR classes. He is always open to help me with the toughest challenges of MR physics that I encountered in my research. I am also thankful for him to show me how to explain the most complicated physics in an understandable and vivid language.

Special thanks to Drs. Gregory Lanza and Shelton Caruthers. It is a great pleasure to work with them and their expertise in molecular imaging is very helpful for the success of my study. Moreover, I really appreciate them for guiding and supporting me to explore my future development.

I would like to thank Dr. Dmitriy Yablonskiy for his kind support for my application of American Heart Association Fellowship. He is very knowledgeable about the MR physics theory, and my knowledge about MR relaxation was significantly enhanced through the very educational discussions with him. Special thanks to Dr. Solin Stuart for serving on my three-person academic committee and always giving valuable suggestions after every committee meeting. I also thank Dr. James Miller for serving on my thesis committee.

I would also like to thank all the members in BMRL, especially Drs. Joe Ackerman, Joel Garbow and Bill Spees, who all provided me generous help and advice during the development of the *in vivo* MR techniques.

Several fellow researchers that I would like to thank: Frank Hockett, Lei Zhang, Xiaoxia Yang, Dr. Hua Pan, Jacob Myerson, Dr. Josh Hood, Ralph Fuhrhop, Angana Senpan, Kirk Hou, Mike Scott, Matt Goette, Grace Hu, Huiying Zhang, John Stacy Allen, Todd William, Yajian Cheng, Dr. Carsten Schirra, Taylor Thompson, Dr. Kezheng Wang and Cordelia Caradine among many others. All the achievements in this dissertation are teamwork.

In the end, and most importantly, I would like extend my great gratitude to my family. My parents born me and raised me with unconditional love and always encouraged me to face new challenges. My wife always supports me with her love and care, no matter in good times or bad. They are always the motivation for me to move forward. To them I dedicate this thesis.

Abstract

Although in clinical use for several decades, magnetic resonance imaging (MRI) is undergoing a transition from a qualitative anatomical imaging tool to a quantitative technique for evaluating myriad diseases. Furthermore, MRI has made great strides as a potential tool for molecular imaging of cellular and tissue biomarkers. Of the candidate contrast agents for molecular MRI, the excellent bio-compatibility and adaptability of perfluorocarbon nanoparticles (PFC NP) has established these agents as a potent targeted imaging agent and as a functional platform for non-invasive oxygen tension sensing. Direct readout and quantification of PFC NP can be achieved with fluorine (^{19}F) MRI because of the unique ^{19}F signal emanating from the core PFC molecules. However, the signal is usually limited by the modest accumulated concentrations as well as several special NMR considerations for PFC NP, which renders ^{19}F MRI technically challenging in terms of detection sensitivity, scan time, and image reconstruction.

In the present dissertation, some of the pertinent NMR properties of PFC NP are investigated and new ^{19}F MRI techniques developed to enhance their performance and expand the biomedical applications of ^{19}F MRI with PFC NP. With the use of both theoretical and experimental methods, we evaluated J-coupling modulation, chemical shift and paramagnetic relaxation enhancement of PFC molecules in PFC NP. Our unique contribution to the technical improvement of ^{19}F MRI of small animal involves: (1) development of general strategies for RF ^{1}H/^{19}F coil design; (2) design of novel MR pulse sequences for ^{19}F T1 quantification; and (3) optimization of imaging protocols for distinguishing and visualizing multiple PFC components ("multi-chromatic" ^{19}F MRI).

The first pre-clinical application of our novel ^{19}F MRI techniques is blood vessel imaging and rapid blood oxygen tension measurement *in vivo*. Blood vessel anatomy and blood oxygen tension provide pivotal physiological information for routine diagnosis of cardiovascular disease. Using our novel "Blood (flow)-Enhanced-Saturation-Recovery (BESR)" sequence, we successfully visualized reduced flow caused by thrombosis in carotid arteries and jugular veins, and we quantified the oxygen tension in the cardiac ventricles of the mouse. The BESR sequence depicted the expected oxygenation difference between arterial and venous blood and accurately registered the response of blood oxygen tension to high oxygen concentration in 100% oxygen gas. This study demonstrated the potential application of PFC NP as a blood oxygen tension sensor and blood pool MR contrast agent for angiography.

Another pre-clinical application investigated was functional kidney imaging with ^{19}F MRI of circulating PFC NP. Conventional functional kidney imaging typically calls for the injection of small molecule contrast agents that may be nephrotoxic, which raises concerns for their clinical applications in patients with renal insufficiency. We demonstrated that our ^{19}F MRI technique offers a promising alternative functional renal imaging approach that generates quantitative measurement of renal blood volume and intrarenal oxygenation. We successfully mapped the expected heterogeneous distribution of renal blood volume and confirmed the presence of an oxygenation gradient in healthy kidneys. We validated the diagnostic capability of ^{19}F MRI in a mouse model of acute ischemia/reperfusion kidney injury. We also employed ^{19}F MRI as a tool to test the therapeutic efficacy of a new nanoparticle-based drug, i. e. PPACK (D-phenylalanyl-L-prolyl-L-arginine chloromethyl ketone) PFC NP, which was postulated to inhibit microvascular coagulation during acute kidney injury. Based on our preliminary ^{19}F MRI findings, we observed that PPACK PFC NP effectively reduced coagulation in our animal

model, as evidenced by lesser accumulation of particles trapped by the clotting process. This finding suggests the potential for ^{19}F MRI to be used as a drug monitoring tool as well in common medical emergencies such as acute kidney failure.

1 Introduction

1.1 Quantitative molecular and functional imaging via MRI

Magnetic Resonance Imaging (MRI) has been widely adopted as a powerful diagnostic imaging modality because of its superior soft tissue contrast and good safety profile compared to other imaging approaches that employ ionizing radiation. In last two decades, researchers have explored the transition of MRI from a tool for strictly anatomical depiction to a reporter of more complex functional and molecular information. These new imaging techniques together with so called “smart” contrast agents are designed to provide new disease biomarkers that identify early disease stages and generate quantitative diagnostic matrices for disease detection, staging, prognosis and therapeutic evaluation (1-3).

Molecular imaging in particular, entails the use of functionalized targeting ligands that complex MR contrast agents to specific biochemical epitopes expressed on cell membranes. A wide variety of targeting ligands already have been synthesized and deployed as components of molecular contrast agent systems for noninvasive visualization of relevant biological signatures in cancer and cardiovascular diseases (e.g., target for fibrin (4), angiogenesis (5), growth factor (6) and endothelial adhesion molecule (7) et al).

In contrast to molecular MRI, functional MRI is focused on the systematic behavior and physiological/pathological change of tissue and organ physiology in response to disease states or external stimuli. To this end, the development of MRI techniques and “functional” MR contrast agents might afford new opportunities for direct and noninvasive readout of essential physiological indexes such as diffusion (8), perfusion (9), PH (10) and blood oxygenation (11), among others.

Because molecular and functional imaging provide different but complementary windows into the same pathological processes, interest is growing for devising potent platforms that permit *both* molecular and functional readouts to delineate the underlying biological state of cancer and cardiovascular disease in a more comprehensive manner (12-13). In terms of the candidate contrast imaging nuclei for use with MRI, functional and molecular MRI might be divided into two general categories: proton and non-proton imaging. Proton imaging would take advantage of intrinsic or contrast-induced relaxation modulation of ^{1}H spins, which can then inform about the localized expression of biological markers or alternatively reflect specific functional parameters revealed through the interaction of the contrast agent with important tissue water compartments. Non-proton MRI would be useful for *directly* detecting clinically relevant elements that exhibit net nuclear spins and could generate magnetization in an external magnetic field, which then interact with tissues. As the default imaging paradigm, proton MR with paramagnetic or superparamagnetic agents is technically translatable, but ^{1}H based molecular and functional applications often suffer from omnipresent ^{1}H background signal, which may hinder unambiguous identification of the expected molecular target or tissue functionality since the background signal is admixed and heterogeneous. In contrast, non-proton contrast MRI might be better suited to registering the specific presence of a disease biomarker or tissue function, because there might be less interfering background signal. However, as an unavoidable tradeoff, non-proton contrast MRI is typically more technically challenging because of the lower gyromagnetic ratio and the inherently lower natural abundance of relevant exogenous contrast-producing atoms as compared to ^{1}H spins (14).

1.1.1 Proton molecular and functional MRI

The distinctive power of ^{1}H MRI originates from the wide selection of contrast mechanisms that can be readily manipulated and engineered by modifying the chemistry of contrast agents, pulse sequences and/or imaging protocols. These contrast mechanisms might be either endogenous or induced by administrating extraneous contrast agents.

Currently, there are several relevant endogenous-contrast based functional imaging approaches that are in or entering clinical use. Among them, diffusion weighted (tensor) MRI takes advantage of water diffusion in soft tissue to produce an MRI readout that generates a detailed mapping of tissue microstructures that establish restricting boundaries to water diffusion (8). Arterial spin labeling (ASL) utilizes special pulse sequences to magnetically label arterial blood flow (15). It is widely studied as an alternative method to traditional perfusion imaging techniques, which otherwise might employ potentially nephrotoxic contrast agents. Blood-Oxygenation-Level-Dependent (BOLD) MRI permits non-invasive detection of neural activation and metabolism by measuring T2* contrast generated by deoxygenated hemoglobin (11).

Exogenous contrast agents are usually engineered for specific applications and exhibit well characterized biochemical properties. The contrast mechanisms of ^{1}H functional and molecular imaging usually entails one of several approaches to modulate local relaxation. Superparamagnetic iron oxide (SPIO) particles generate local magnetic field inhomogeneities that can be visualized using T2*-weighted gradient echo sequences (16). Paramagnetic contrast agents such as Gd and Mn affect proton relaxation in proportion to their absolute concentration, which can be represented by the signal intensity of T1-weighted images (17). Several other contrast mechanisms (such as T1ρ (18) and CEST (19)) are intriguing but eventual clinical adoption of these methods remains under investigation. However, for purposes of molecular

imaging, it is clear that all ^{1}H based imaging techniques would require an extra scan to acquire a pre-contrast baseline view since only relative changes in signal are examined upon contrast localization, making these approaches highly susceptible to position shifts between the two scans, which poses difficulties for fiducial image coregistration.

1.1.2 Non-proton molecular and functional MRI

In addition to protons, other nuclei exhibit net nuclear spins. Most of these nuclei (e.g., ^{31}P and ^{23}Na) have much lower gyromagnetic ratios (^{31}P: 108.4×10^{6} rad•s^{-1}•T^{-1}, ^{23}Na: 70.8×10^{6} rad•s^{-1}•T^{-1}) and therefore dramatically different resonant frequencies from ^{1}H (267.5×10^{6} rad•s^{-1}•T^{-1}). Despite their relatively low MR sensitivity, ^{31}P and ^{23}Na are widely exploited as endogenous non-proton nuclei for functional imaging of tissue metabolism because they are key elements of important organic and inorganic molecules that are naturally present in animals and humans (20-21).

With respect to our interest in fluorinated agents for imaging that will be examined in depth in this thesis, the gyromagnetic ratio of the ^{19}F nuclear spin (251.8×10^{6} rad•s^{-1}•T^{-1}) is very close to that of ^{1}H. Because the MRI signal is proportional to the gyromagnetic ratio, at similar concentration levels ^{19}F spins can generate comparable MR signals to those for ^{1}H spins, both being much stronger than that of other MR-active imaging nuclei. Moreover, because there is no ^{19}F background in human body (and animals) under physiological conditions, ^{19}F imaging can be performed without the need for a pre-scan. This unique feature of ^{19}F MRI renders it a promising imaging approach with extraordinary specificity. Finally, because ^{19}F atoms can be readily engineered into various organic molecules by substituting ^{1}H, ^{19}F MRI with the use of appropriately functionalized contrast agents represents a versatile molecular imaging paradigm for quantifying biomarker expression at the cellular and tissue level (22).

1.2 Perfluorocarbon nanoparticle as a MRI contrast agent

Perfluorocarbon (PFC) based nanoparticles (NPs) are a class of highly adaptable delivery vehicles for targeted molecular imaging and a functional platform for noninvasive oxygen tension (pO_2) sensing. PFC comprises ^{19}F-containing molecules that are derived from hydrocarbons by substitution of ^{1}H with ^{19}F atoms. The PFC component has been clinically approved as blood substitute for over 20 years and exhibits a good bio-safety profile because it is biologically inert and not metabolized *in vivo*. The nominal size of a PFC NP is 200-250 nm in diameter and the half life in the blood stream is 2-4 hours. The particles are cleared predominatly by the liver and spleen and the PFC components are vaporized through the lung. In addition to applications in diagnostic imaging, PFC NPs also have been developed as a potential vehicle for drug delivery (23-26).

PFC NP formulation consists of a hydrophobic core of PFC molecules encapsulated within a phospholipid surfactant monolayer coating. A variety of PFC compositions can be used to form the PFC core based on a generalized synthetic procedure. Conventional ^{1}H imaging contrast agent (such as Gd chelates), fluorescence imaging moieties, drugs, and important targeting ligands can be conjugated covalently or noncovalently to the surface of the lipid layer to functionalize the PFC NPs. Therefore, PFC NPs serve as excellent candidates for molecular and functional imaging of both ^{1}H and ^{19}F MRI, although in this dissertation we will focus on examining applications of PFC NP for ^{19}F MRI.

1.2.1 Targeted molecular imaging using ^{19}F MRI of PFC NP

Targeted PFC NPs actively bind to molecular biomarkers at disease sites and can be imaged with the use of ^{19}F MRI. It has been shown that ^{19}F MRI can report sparse distributions of PFC

NP even at very low concentrations (i.e., picomolar nanoparticle levels) (27). As compared to imaging PFC NP that incorporate Gd atoms as a contrast agent, when imaging the fluorine core elements with ^{19}F MRI one can avoid potential renal damage or nephrogenic systemic fibrosis that can be attributed to the systemic toxicity of the lanthanide components (28).

Applications of molecular ^{19}F MRI have been demonstrated in multiple preclinical animal models simulating either cardiovascular disease or cancer in human. For example, tumor angiogenesis could be successfully depicted by ^{19}F MRI of $\alpha_v\beta_3$ integrin targeted PFC NP (29). The same particle containing fibrin targeting ligands binds to unstable or disrupted atherosclerotic plaques where rupture exposes the arterial wall to clot formation. In this particular application, ^{19}F MRI offers a quantitative readout of local particle concentration and confirms the expected heterogeneous accumulation of PFC NPs throughout the vascular wall (30). Moreover, in cases of very advanced plaques with endothelial barrier disruption, PFC NP without any targeting ligands passively penetrate into these plaques to reveal highly permeable and disrupted lesions that might portend eventual heart attack or stroke (31). Furthermore, advanced MR pulse sequences (e.g., diffusion weighted ^{19}F sequence (32)) in association with other targeting moieties (e.g., adhesion molecules such as vascular cell adhesion molecule, or VCAM (7)) may extend ^{19}F molecular imaging to early detection of inflammatory vascular disease.

1.2.2 Cell tracking using ^{19}F MRI of PFC NP

Another important application of PFC NP for^{19}F imaging is cell tracking. Multiple cells types can be labeled with PFC NP for *in vivo* tracking after injection as tissue regenerative therapies in preclinical models, e.g., heart ischemia (33), lung injury (34) and organ transplant (35), among others. Among all cell types, the macrophage is the most widely studied because of its critical

role in vascular inflammatory processes. Macrophages can be labeled with PFC NP either through in vitro incubation or *in vivo* labeling in blood stream. Macrophages internalize PFC NPs through endocytosis and then actively home to the disease regions without any observable loss of cellular functionality. ^{19}F MRI enables a noninvasive measurement of the macrophages recruitment, which is an essential component of plaque inflammation (36). In addition to macrophages, various stem cells (37) and immune dendritic cells (38) have been labeled with PFC NP. Accordingly, *in vivo* tracking of stem cells labeled with unique, no background fluorine signatures could provide a useful imaging approach for monitoring on-going trials of stem-cell therapy.

1.2.3 PFC NP as an oxygen sensor

Because of the long residence time (2-3 hours) in blood stream, PFC NP can be employed as a blood pool contrast agent in near steady state conditions. Conventional study of neat PFC molecule has revealed that the relaxation time of ^{19}F (or, R1 = 1/T1) is linearly correlated with local oxygen tension. In these studies, PFC was administrated directly into solid tumors followed by ^{19}F T1 measurement to generate oxygenation mapping. It has been demonstrated in previous reports that ^{19}F MRI of PFC NP was more sensitive to detect tumor hypoxia as compared with conventional BOLD MRI (39).

Functional ^{19}F imaging with PFC NP also has been validated in other organs. For example, ^{19}F MRI of PFC NP has been utilized as a non-invasive method to evaluate oxygen tension in livers and spleens, because most PFC NPs are trapped by reticuloendothelial system after being cleared from the blood stream (40). As another interesting application of functional imaging with PFC NP, Duong et al proposed a new method for measuring arterial and venous blood fraction in mouse brain (41) by combining absolute quantification of ^{19}F concentration and ^{19}F T1.

1.2.4 PFC NP as a ^{1}H molecular imaging contrast agent

Applications of PFC NP containing large quantities of Gd (100-200,000 atoms as chelates) for use as a ^{1}H contrast agent for molecular imaging have been extensively investigated in preclinical models of cancer and cardiovascular disease, among which angiogenesis imaging appears most promising (42). In this case, targeting the PFC NP to the $\alpha_v\beta_3$ integrin, which is present in large quantities on newly forming blood vessels in cancers and atherosclerosis, facilitates active binding to locations where new blood vessels are sprouting. Because the Gd payload is situated on the surface of PFC NP, a direct inner-sphere dipole-dipole interaction occurs between Gd and the water molecules in the vicinity of the $\alpha_v\beta_3$-integrin targeted sites. The magnitude of the relaxation effect is dependent on the chemical structure of the Gd chelates, and those chelates with very short lipid linker segments (Bis-oleate-DTPA) that partially hide the Gd at the particle surface manifest lesser effects than do those with longer lipid linker chain (e.g., DOTA-DPPE) that allow more flexible exposure to surrounding waters. (43). Conventional T1-weighted spin echo or gradient echo sequences can be employed to visualize accumulation of particles *in vivo*. Other combinations of targeting ligands (e.g., $\alpha_5\beta_1$ (44) and Robo4 (45)) and imaging agents on PFC NP (e.g Mn (46)) have been formulated and validated in preclinical disease models.

1.3 Technical challenges of ^{19}F MRI

Although ^{19}F MRI of PFC NP has undergone rapid growth in last 10 years and presents a promising future for eventual deployment in clinical settings, this new imaging paradigm is still in its early technical development stages and will benefit from further technical advances to bridge the gap between laboratory investigations and clinical utility. Compared to ^{1}H MRI, ^{19}F

manifests no appreciable background signal, and so the signal strength for ^{19}F MRI is limited by the modest doses of fluorine that can be administered as PFC NP. Therefore, it is critical to improve imaging methodologies to enhance the detection limits for PFC NP that typically are present in low concentrations. Moreover, accurate quantification of PFC NP *in vivo* requires robust imaging methods immune to potential field inhomogeneities associated with the imaging system (B0, B1 and sensitivity), because the spatial distribution of PFC NP for molecular imaging is generally heterogeneous, as a consequence of the individual expression patterns of the targeted pathological epitopes, which are typically sparse in tissue. Finally, in contrast to ^{1}H atoms in water, ^{19}F atoms in PFC experience a more complicated chemical environment, which might result in multiple chemical shifts and scalar coupling (J-coupling) between different groups, all of which complicates the imaging objective.

1.3.1 Signal to Noise Ratio (SNR)

There are two major factors limiting the potential MR signal strength for ^{19}F MRI: one is the total number of ^{19}F nuclei present in the targeted tissue and the other is the Boltzmann distribution which leaves only a small portion of all the ^{19}F nuclei generating observable magnetization. Several approaches have been pursued to improve SNR in ^{19}F MRI. It is well accepted that improving the sensitivity of ^{19}F RF coils is the most straightforward approach to increase image quality. It is necessary to design application-specific RF coils which are suitable to particular imaging animals and organs and thus avoid RF loss on redundant components (low filling factor) of the RF coils. Moreover, improving electronic design of RF coils and enhancing the quality factor (Q value) of RF circuits might also substantially improve the receive sensitivity. Besides RF coils, pulse sequences also are targets for optimizing ^{19}F imaging. It has been shown that different pulse sequences might yield over 3-fold better SNR for the same

imaging subject (47). Therefore, it is essential to design or choose appropriate pulse sequences that are suitable for specific ^{19}F imaging applications. Recently, researchers have reported several pioneering trials to develop hyperpolarization technique for ^{19}F spins (48). Theoretically, by hyperpolarizing ^{19}F spins, ^{19}F spins could break the thermal equilibrium state (Boltzmann distribution) and produce several orders of magnitude stronger MR signals.

1.3.2 Quantitative methodology

^{19}F MRI is quantitative in principle because ^{19}F spin density is linearly correlated to the PFC NP concentration and ^{19}F relaxation directly reflects oxygenation. However, in most *in vivo* applications, many other factors might come into play and affect the measurement accuracy of ^{19}F MRI. For example, ^{19}F quantification might suffer from field inhomogeneity of the transmit and receive coils. Moreover, the measured ^{19}F signal might not only reflect ^{19}F concentration but be convoluted with other factors that might induce changes of ^{19}F T1 and T2 et al. Similar to ^{1}H MRI, ^{19}F also is susceptible to imaging artifacts, such as motion and eddy current artifacts, all of which compromise image quality and generate unexpected errors for quantification (29). Therefore, in order to achieve reliable and reproducible ^{19}F MRI measurements across different applications, it is necessary to implement robust correction methods and optimized artifact-resistant pulse sequences.

1.3.3 J-coupling and chemical shift

PFC molecules are more complicated than water in terms of their NMR properties. PFC can exhibit multiple chemical shifts, and ^{19}F atoms from different chemical groups can also have strong interactions with each other. Therefore, imaging ^{19}F spins in PFC molecule can be more challenging than is ^{1}H imaging. For example, chemical shifts might cause shift artifacts along the readout gradient direction, and special reconstruction algorithms are needed to correct for these.

Moreover, J-coupling between different chemical groups in PFC molecule causes "T2-shortening like" behavior in spin echo-based MRI, i.e., J-modulation, which significantly reduces the detectable signal intensity for ^{19}F imaging. However, once the underlying physics of these special NMR features of PFC NP are accounted for, we can avoid the resultant artifacts or even take advantage of these properties and expand ^{19}F MRI to additional applications (49).

1.4 Dissertation objective and organization

1.4.1 Overarching objective

The objectives of this dissertation are three fold. (1) We aimed to understand the physical and chemical properties of PFC NP that are related to its applications as a ^{19}F MRI contrast agent. We will build up physical models that apply quantum mechanical principles to investigate the spin dynamics of ^{19}F nuclear spins in an external magnetic field, and to examine the interaction between ^{19}F spins and other nuclear spins and electron spins. (2) Based on the theoretical frame work of ^{19}F spin dynamics and MRI engineering, we seek to implement novel MRI imaging techniques including pulse sequences, RF coils, imaging protocols and chemical modifications to enhance and expand the use of PFC NP-based functional and molecular ^{19}F MRI in preclinical animal models. (3) With the newly developed ^{19}F MRI techniques, we will devise and validate new biomedical applications of ^{19}F functional MRI in small animal models. These applications include a novel ^{19}F MRI based rapid blood oxygenation measurement method and a new comprehensive diagnostic approach for evaluating kidney endothelial damage based on ^{19}F MRI of circulating PFC NP. We anticipate that these preclinical studies should demonstrate the superior diagnostic capability of ^{19}F MRI and can be readily translated to real world clinical applications.

1.4.2 Organization

Following the introduction, in Chapter 2, we present a general coupled resonator model and validate this model as a universal strategy for building $^{1}H/^{19}F$ dual frequency RF coils. We also summarize and investigate the general requirements for designing transmit and receive coils for ^{19}F MRI and validate our methods in phantom and *in vivo* studies. This chapter has been published in Journal of Magnetic Resonance Imaging, Volume 34, Issue 1, pages 245–252, July 2011

In Chapter 3, we establish physical models and propose theoretical treatments for the NMR properties of PFC NP. We investigate the effect of oxygenation on the absolute quantification of PFC concentration *in vivo* and in phantoms. In this part, we propose general criteria for achieving consistent and highly sensitive PFC quantification that is robust against oxygenation effects on relaxivity. Using a density matrix calculation and Hamiltonian time-evolution, we investigate theoretically the J-coupling induced amplitude modulation effect in PFC NP and develop a method to suppress the potential imaging artifacts associated with this effect. In the end, we study the chemical shift effect of PFC NP, from which we propose a "multi-chromatic" ^{19}F MRI technique for selectively imaging of multiple PFC NPs separately in the same imaging subject.

In Chapter 4, we examine the interaction between ^{19}F spins inside PFC NP with paramagnetic ions on the surface or in the surrounding solution. In this part, the paramagnetic relaxation enhancement effect of Gd on ^{19}F is calculated theoretically with the use of quantum perturbation theory. We observe that short-linker paramagnetic chelates that are covalently conjugated to the surface of PFC NP may significantly enhance ^{19F} relaxation and this effect is modulated by cellular endocytosis and particle lipid breakdown mechanisms in endosomes as a

probe of cellular activation. This chapter has been published in Journal of Magnetic Resonance Imaging, Volume 34, Issue 3, pages 653–661, September 2011

In Chapter 5, we exploit PFC NP as a blood pool contrast agent for angiography and blood oxygenation sensing. We demonstrate the application of PFC NP as a blood oxygen tension probe with the use of a novel blood-flow enhanced saturation recovery (BESR) pulse sequence. Compared to the traditional Look-Locker sequence, the BESR sequence is insensitive to B1 and B0 field inhomogeneity and pulsatile blood in-flow effects. Compared to traditional invasive measurements using cardiac catheterization, the BESR sequence provides a simple and rapid method for non-invasive assessment of blood oxygenation *in vivo*. This chapter has been published in Magnetic Resonance in Medicine, DOI: 10.1002/mrm.24436.

In Chapter 6, we develop a new ^{19}F functional MRI technique for kidney imaging. We first validate the feasibility and durability of our technique for measuring renal blood volume and intrarenal oxygenation in healthy kidneys. The measured regional intrarenal blood volume and oxygenation appears to be consistent with prior experimental observations. In a mouse model of ischemia-reperfusion acute injury, ^{19}F MRI of PFC NP is shown to delineate reduced blood volume at cortico-medullary junction and vascular leakage at medulla as a consequence of endothelial damage. Finally using ^{19}F MRI as a treatment evaluation tool, we confirm the treatment effect of a novel PFC NP based anti-clotting drug for inhibiting intrarenal coagulation during acute kidney injury. This chapter is under revision for Magnetic Resonance in Medicine.

In the last Chapter, we summarize these findings throughout the dissertation, and discuss future work for PFC NP based functional and molecular ^{19}F MRI.

1.5 References

1. Winter PM, Caruthers SD, Wickline SA, Lanza GM. Molecular imaging by MRI. Curr Cardiol Rep 2006;8(1):65-69.
2. Wickline SA, Neubauer AM, Winter PM, Caruthers SD, Lanza GM. Molecular imaging and therapy of atherosclerosis with targeted nanoparticles. J Magn Reson Imaging 2007;25(4):667-680.
3. Fox MD, Raichle ME. Spontaneous fluctuations in brain activity observed with functional magnetic resonance imaging. Nat Rev Neurosci 2007;8(9):700-711.
4. Lanza GM, Lorenz CH, Fischer SE, Scott MJ, Cacheris WP, Kaufmann RJ, Gaffney PJ, Wickline SA. Enhanced detection of thrombi with a novel fibrin-targeted magnetic resonance imaging agent. Acad Radiol 1998;5 Suppl 1:S173-176; discussion S183-174.
5. Anderson SA, Rader RK, Westlin WF, Null C, Jackson D, Lanza GM, Wickline SA, Kotyk JJ. Magnetic resonance contrast enhancement of neovasculature with alpha(v)beta(3)-targeted nanoparticles. Magn Reson Med 2000;44(3):433-439.
6. Yang L, Mao H, Wang YA, Cao Z, Peng X, Wang X, Duan H, Ni C, Yuan Q, Adams G, Smith MQ, Wood WC, Gao X, Nie S. Single chain epidermal growth factor receptor antibody conjugated nanoparticles for in vivo tumor targeting and imaging. Small 2009;5(2):235-243.
7. Southworth R, Kaneda M, Chen J, Zhang L, Zhang H, Yang X, Razavi R, Lanza G, Wickline SA. Renal vascular inflammation induced by Western diet in ApoE-null mice quantified by (19)F NMR of VCAM-1 targeted nanobeacons. Nanomedicine 2009;5(3):359-367.

8. Le Bihan D, Mangin JF, Poupon C, Clark CA, Pappata S, Molko N, Chabriat H. Diffusion tensor imaging: concepts and applications. J Magn Reson Imaging 2001;13(4):534-546.

9. Tofts PS, Brix G, Buckley DL, Evelhoch JL, Henderson E, Knopp MV, Larsson HB, Lee TY, Mayr NA, Parker GJ, Port RE, Taylor J, Weisskoff RM. Estimating kinetic parameters from dynamic contrast-enhanced T(1)-weighted MRI of a diffusable tracer: standardized quantities and symbols. J Magn Reson Imaging 1999;10(3):223-232.

10. Kalman FK, Woods M, Caravan P, Jurek P, Spiller M, Tircso G, Kiraly R, Brucher E, Sherry AD. Potentiometric and relaxometric properties of a gadolinium-based MRI contrast agent for sensing tissue pH. Inorg Chem 2007;46(13):5260-5270.

11. Ogawa S, Lee TM, Kay AR, Tank DW. Brain magnetic resonance imaging with contrast dependent on blood oxygenation. Proc Natl Acad Sci U S A 1990;87(24):9868-9872.

12. Choudhury RP, Fuster V, Fayad ZA. Molecular, cellular and functional imaging of atherothrombosis. Nat Rev Drug Discov 2004;3(11):913-925.

13. Benaron DA. The future of cancer imaging. Cancer Metastasis Rev 2002;21(1):45-78.

14. Levitt MH. Spin dynamics : basics of nuclear magnetic resonance. Chichester, England ; Hoboken, NJ: John Wiley & Sons; 2008. xxv, 714 p., 717 p. of plates p.

15. Williams DS, Detre JA, Leigh JS, Koretsky AP. MAGNETIC-RESONANCE-IMAGING OF PERFUSION USING SPIN INVERSION OF ARTERIAL WATER. Proc Natl Acad Sci U S A 1992;89(1):212-216.

16. Harisinghani MG, Barentsz J, Hahn PF, Deserno WM, Tabatabaei S, van de Kaa CH, de la Rosette J, Weissleder R. Noninvasive detection of clinically occult lymph-node metastases in prostate cancer. N Engl J Med 2003;348(25):2491-2499.

17. Pautler RG, Silva AC, Koretsky AP. In vivo neuronal tract tracing using manganese-enhanced magnetic resonance imaging. MagnResonMed 1998;40(5):740-748.

18. Regatte RR, Akella SVS, Borthakur A, Kneeland JB, Reddy R. In vivo proton MR three-dimensional T1p mapping of human articular cartilage: Initial experience. Radiology 2003;229(1):269-274.

19. Ward KM, Aletras AH, Balaban RS. A new class of contrast agents for MRI based on proton chemical exchange dependent saturation transfer (CEST). J Magn Reson 2000;143(1):79-87.

20. Maril N, Rosen Y, Reynolds GH, Ivanishev A, Ngo L, Lenkinski RE. Sodium MRI of the human kidney at 3 tesla. MagnResonMed 2006;56(6):1229-1234.

21. Zhang JY, Wilke N, Wang Y, Zhang Y, Wang CS, Eijgelshoven MHJ, Cho YK, Murakami Y, Ugurbil K, Bache RJ, From AHL. Functional and bioenergetic consequences of postinfarction left ventricular remodeling in a new porcine model - MRI and P-31-MRS study. Circulation 1996;94(5):1089-1100.

22. Chen J, Lanza GM, Wickline SA. Quantitative magnetic resonance fluorine imaging: today and tomorrow. Wiley Interdiscip Rev Nanomed Nanobiotechnol 2010;2(4):431-440.

23. Wickline SA, Neubauer AM, Winter P, Caruthers S, Lanza G. Applications of nanotechnology to atherosclerosis, thrombosis, and vascular biology. Arterioscler Thromb Vasc Biol 2006;26(3):435-441.

24. Pan H, Soman NR, Schlesinger PH, Lanza GM, Wickline SA. Cytolytic peptide nanoparticles ('NanoBees') for cancer therapy. Wiley Interdiscip Rev Nanomed Nanobiotechnol 2011;3(3):318-327.

25. Caruthers SD, Cyrus T, Winter PM, Wickline SA, Lanza GM. Anti-angiogenic perfluorocarbon nanoparticles for diagnosis and treatment of atherosclerosis. Wiley Interdiscip Rev Nanomed Nanobiotechnol 2009;1(3):311-323.

26. Lanza GM, Winter PM, Caruthers SD, Hughes MS, Hu G, Schmieder AH, Wickline SA. Theragnostics for tumor and plaque angiogenesis with perfluorocarbon nanoemulsions. Angiogenesis 2010;13(2):189-202.

27. Morawski AM, Lanza GA, Wickline SA. Targeted contrast agents for magnetic resonance imaging and ultrasound. Curr Opin Biotechnol 2005;16(1):89-92.

28. Aspelin P, Aubry P, Fransson SG, Strasser R, Willenbrock R, Berg KJ. Nephrotoxic effects in high-risk patients undergoing angiography. N Engl J Med 2003;348(6):491-499.

29. Keupp J, Rahmer J, Grasslin I, Mazurkewitz PC, Schaeffter T, Lanza GM, Wickline SA, Caruthers SD. Simultaneous dual-nuclei imaging for motion corrected detection and quantification of 19F imaging agents. Magn Reson Med 2011;66(4):1116-1122.

30. Morawski AM, Winter PM, Yu X, Fuhrhop RW, Scott MJ, Hockett F, Robertson JD, Gaffney PJ, Lanza GM, Wickline SA. Quantitative "magnetic resonance immunohistochemistry" with ligand-targeted (19)F nanoparticles. Magn Reson Med 2004;52(6):1255-1262.

31. Zhang H, Zhang L, Myerson J, Bibee K, Scott M, Allen J, Sicard G, Lanza G, Wickline S. Quantifying the evolution of vascular barrier disruption in advanced atherosclerosis with semipermeant nanoparticle contrast agents. PLoS One 2011;6(10):e26385.

32. Waters EA, Chen J, Yang X, Zhang H, Neumann R, Santeford A, Arbeit J, Lanza GM, Wickline SA. Detection of targeted perfluorocarbon nanoparticle binding using 19F diffusion weighted MR spectroscopy. Magn Reson Med 2008;60(5):1232-1236.

33. Flogel U, Ding Z, Hardung H, Jander S, Reichmann G, Jacoby C, Schubert R, Schrader J. In vivo monitoring of inflammation after cardiac and cerebral ischemia by fluorine magnetic resonance imaging. Circulation 2008;118(2):140-148.

34. Ebner B, Behm P, Jacoby C, Burghoff S, French BA, Schrader J, Flogel U. Early assessment of pulmonary inflammation by 19F MRI in vivo. Circ Cardiovasc Imaging 2010;3(2):202-210.

35. Hitchens TK, Ye Q, Eytan DF, Janjic JM, Ahrens ET, Ho C. 19F MRI detection of acute allograft rejection with in vivo perfluorocarbon labeling of immune cells. Magn Reson Med 2011;65(4):1144-1153.

36. Kadayakkara DK, Ranganathan S, Young WB, Ahrens ET. Assaying macrophage activity in a murine model of inflammatory bowel disease using fluorine-19 MRI. Lab Invest 2012;92(4):636-645.

37. Partlow KC, Chen J, Brant JA, Neubauer AM, Meyerrose TE, Creer MH, Nolta JA, Caruthers SD, Lanza GM, Wickline SA. 19F magnetic resonance imaging for stem/progenitor cell tracking with multiple unique perfluorocarbon nanobeacons. FASEB J 2007;21(8):1647-1654.

38. Waiczies H, Lepore S, Janitzek N, Hagen U, Seifert F, Ittermann B, Purfurst B, Pezzutto A, Paul F, Niendorf T, Waiczies S. Perfluorocarbon particle size influences magnetic resonance signal and immunological properties of dendritic cells. PLoS One 2011;6(7):e21981.

39. Mason RP, Antich PP, Babcock EE, Constantinescu A, Peschke P, Hahn EW. Non-invasive determination of tumor oxygen tension and local variation with growth. Int J Radiat Oncol Biol Phys 1994;29(1):95-103.

40. Giraudeau C, Djemai B, Ghaly MA, Boumezbeur F, Meriaux S, Robert P, Port M, Robic C, Le Bihan D, Lethimonnier F, Valette J. High sensitivity 19F MRI of a perfluorooctyl bromide emulsion: application to a dynamic biodistribution study and oxygen tension mapping in the mouse liver and spleen. NMR Biomed 2012;25(4):654-660.

41. Duong TQ, Kim SG. In vivo MR measurements of regional arterial and venous blood volume fractions in intact rat brain. Magn Reson Med 2000;43(3):393-402.

42. Winter PM, Morawski AM, Caruthers SD, Fuhrhop RW, Zhang H, Williams TA, Allen JS, Lacy EK, Robertson JD, Lanza GM, Wickline SA. Molecular imaging of angiogenesis in early-stage atherosclerosis with alpha(v)beta3-integrin-targeted nanoparticles. Circulation 2003;108(18):2270-2274.

43. Winter P, Athey P, Kiefer G, Gulyas G, Frank K, Fuhrhop R, Robertson D, Wickline S, Lanza G. Improved paramagnetic chelate for molecular imaging with MRI. J Magn Magn Mater 2005;293(1):540-545.

44. Schmieder AH, Caruthers SD, Zhang H, Williams TA, Robertson JD, Wickline SA, Lanza GM. Three-dimensional MR mapping of angiogenesis with alpha5beta1(alpha nu beta3)-targeted theranostic nanoparticles in the MDA-MB-435 xenograft mouse model. FASEB J 2008;22(12):4179-4189.

45. Boles KS, Schmieder AH, Koch AW, Carano RA, Wu Y, Caruthers SD, Tong RK, Stawicki S, Hu G, Scott MJ, Zhang H, Reynolds BA, Wickline SA, Lanza GM. MR

angiogenesis imaging with Robo4- vs. alphaVbeta3-targeted nanoparticles in a B16/F10 mouse melanoma model. FASEB J 2010;24(11):4262-4270.

46. Pan D, Caruthers SD, Hu G, Senpan A, Scott MJ, Gaffney PJ, Wickline SA, Lanza GM. Ligand-directed nanobialys as theranostic agent for drug delivery and manganese-based magnetic resonance imaging of vascular targets. J Am Chem Soc 2008;130(29):9186-9187.

47. Giraudeau C, Flament J, Marty B, Boumezbeur F, Meriaux S, Robic C, Port M, Tsapis N, Fattal E, Giacomini E, Lethimonnier F, Le Bihan D, Valette J. A new paradigm for high-sensitivity 19F magnetic resonance imaging of perfluorooctylbromide. Magn Reson Med 2010;63(4):1119-1124.

48. Bommerich U, Trantzschel T, Mulla-Osman S, Buntkowsky G, Bargon J, Bernarding J. Hyperpolarized 19F-MRI: parahydrogen-induced polarization and field variation enable 19F-MRI at low spin density. Phys Chem Chem Phys 2010;12(35):10309-10312.

49. Yu JX, Kodibagkar VD, Cui WN, Mason RP. F-19: A versatile reporter for non-invasive physiology and pharmacology using magnetic resonance. Curr Med Chem 2005;12(7):819-848.

2 General strategy for building $^{1}H/^{19}F$ RF coils

2.1 Background

Dual-nuclei $^{19}F/^{1}H$ MRI/MRS is emerging as a novel imaging technique for molecular imaging and quantification of tissue pathology that features both rapid acquisition with high spatial and temporal resolution (^{1}H) and unique, no background spectral signatures (^{19}F) (1). However, MRI of fluorinated contrast agent suffers principally from low sensitivity especially at clinical field strengths, even despite the fact that ^{19}F is a high signal nucleus, requiring millimolar quantities of contrast agent per voxel for detection (2). Because the amount of fluorine achievable by molecular targeting is limited by the concentration of epitopes that bind the contrast agent, which itself is a function of the tissue pathobiology, improvements in sensitivity and speed are better addressed with the use of specialized and dedicated RF coils. Such coils could be designed to simultaneously achieve high signal-to-noise ratio (SNR) and homogeneous acquisition for detecting and quantifying molecular biomarkers with dual-nuclei $^{19}F/^{1}H$ MRI.

Previous studies typically used single-frequency mode RF coils for $^{19}F/^{1}H$ MRI. A common approach is to use frequency tunable coils, in which case the coil must be tuned to either ^{19}F or ^{1}H frequency to maximize SNR at the cost of extra time for coil tuning and positional shifting of the imaged object (3). Alternatively, a two-coil setup with a volume coil for ^{1}H imaging and surface coil for ^{19}F imaging introduces inherent sensitivity profile differences at the two frequencies (4). Finally, the usage of auto-tuned RF coils that can switch resonant frequency with the assistance of an external computer program entails extra complexity and the associated higher cost of the imaging system (5). Thus, the use of single-frequency mode RF coils for

$^{19}F/^{1}H$ MRI imaging poses a number of limitations including challenges in simultaneously achieving high sensitivity and B1 field homogeneity, and inaccurate co-registration of $^{1}H/^{19}F$ signals due to positional artifacts caused by coil retuning (6). It has been shown that these limitations may be minimized with the use of dual-frequency mode RF coils for multi-nuclear MRI/MRS (7).

Regarding the details of coil design, the commonly used shunting method and multiple poles method for designing dual-frequency coils work well when the two resonant frequencies are well separated, e.g., for ^{1}H (42.58 MHz/T) and ^{13}C (10.71 MHz/T). However, such methods are not well suited for designing $^{19}F/^{1}H$ MRI coils (8-9) because the gyromagnetic ratio of ^{19}F (40.08 MHz/T) is close to that of ^{1}H (10). Several dual-frequency strategies have been proposed for MRI/MRS at close frequencies but each has limitations. A universal matching circuit for multi-nuclei NMR has been proposed (11), but it requires multi-port inputs for multi-frequency. Alternatively, several dual-frequency strategies for close and well-separated frequencies have been proposed based on the special resonant property of a birdcage resonator (12-14). In these works, the two crossed cages or two different modes of a birdcage are utilized to achieve the double resonance, so these techniques are only suitable for coils with birdcage geometry, and could lead to different B1 field distributions at the two frequencies. Recently, a novel $^{19}F/^{1}H$ dual-frequency solenoid coil with identical field distribution at two frequencies at 3 T has been proposed by researchers at Philips Research based on the coupled resonator model (15). However, it remains unknown whether this concept establishes a general RF design approach for such RF coils considering the various geometrical and electrical parameters required to fit the needs of diverse experimental situations (16).

In the present work we seek to develop the coupled resonator model as a universal technique to design and fabricate $^{19}F/^{1}H$ dual-frequency coils in diverse configurations. Due to the different impedances at the two resonant frequencies, matching for a dual-frequency coil remains a critical challenge in practical application. Accordingly, the electrical properties of the coupled resonator model were considered and a numerical calculation was executed to prove that a series capacitive matching network is theoretically effective in matching the coupled resonator to 50 Ohm at both ^{19}F and ^{1}H frequencies (9,17). A $^{19}F/^{1}H$ dual-frequency birdcage RF coil for in vivo imaging at 4.7 T was implemented to illustrate the feasibility of the model. Finally, for an experiment requiring high imaging SNR within a short acquisition time, an actively-decoupled $^{19}F/^{1}H$ dual-frequency saddle coil was built. We show that using the saddle coil for ^{19}F and ^{1}H excitation and using an actively-decoupled surface coil on ^{19}F frequency for both ^{19}F and ^{1}H signal receiving, the two-coil setup can achieve homogeneous excitation with high sensitivity for ^{19}F MRI while retaining sufficient SNR from ^{1}H signal for anatomy images.

2.2 Material and Methods

2.2.1 Coupled resonator model

In the present coupled resonator model, the RF sample coil is connected to a secondary inductor and capacitor (LC) resonator with a coupling capacitor in series (Figure 2.1a). For nuclei with close resonance frequencies, such as ^{1}H and ^{19}F, the inductance of a MR sample coil can be treated as a constant value. Following the theoretical analysis proposed by Haase et al (18), when the secondary resonator is built with identical frequency to the sample coil, two possible oscillating modes are formed within the circuit, namely in-phase and anti-phase modes. When resonating at the in-phase mode, the two resonators of the circuit have equal electrical

potentials, and thus the voltage and current across the coupling capacitor always remains zero. In this case, the coupling capacitor can be virtually removed and then the equivalent circuit of the coupled resonator can be drawn as Figure 2.1b with the resonant frequency

$$\omega_{hi} = \gamma_H B = 1/\sqrt{LC_{t1}}\,. \qquad [1]$$

In contrast, for the anti-phase mode, the electric potential at both sides of the coupling capacitor is opposite, so the voltage at the middle point of coupling capacitor remains zero. For circuit analysis, a virtual short wire can be added between the ground and the middle point of the coupling capacitor (Figure 2.1c), and thus it gives rise to a different resonant frequency

$$\omega_{lo} = \gamma_F B = 1/\sqrt{L(C_{t1} + 2C_c)}\,. \qquad [2]$$

Given the gyromagnetic ratios of ^{1}H and ^{19}F, when

$$C_c / C_{t1} = 0.064\,, \qquad [3]$$

the two frequencies of the coupled resonator correspond to ^{1}H and ^{19}F frequencies, in agreement with the analytic calculation of transfer impedance (19).

2.2.2 Impedance matching

Impedance matching is critical in dual-frequency coil design, because the circuit impedance could be different at the two resonant frequencies. For the coupled identical resonator model (Figure 2.1d), specifically, by inverting the admittance of the parallel components, the impedance of the coupled resonator is

$$Z_{hi} = \frac{X_L + r_1}{1 + (X_L + r)X_{C_{t1}}} \qquad [4]$$

at high frequency or in-phase mode; and

$$Z_{lo} = \frac{X_L + r_1}{1 + (X_L + r)(2X_{C_c} + X_{C_{t1}})} \qquad [5]$$

at low frequency or anti-phase mode.

In the proposed dual-frequency coil design (Figure 2.1d), the coupled resonator is connected to the MR scanner at the end of the secondary resonator in series with a capacitor matching circuit. In this case, a small detuning of two resonators, which renders them slightly off-resonance, is able to introduce an extra degree of freedom and compensate for the impedance difference (18). To show the coupled resonator can always be matched to 50 Ohm with the use of appropriate values for tuning, coupling and matching capacitors, we numerically calculated several realistic circuit examples corresponding to various combinations of internal resistances of the sample coil and secondary resonator. With no loss of generality, we assumed that the sample coil with an inductance 32 nH, which is equal to the inductance of the secondary resonator, is designed to work at 4.7 T for dual-frequency ^{19}F and ^{1}H imaging. A custom-developed program in Mathematica (Wolfram, USA) was used to seek for the appropriate values of C_{t1}, C_{t2}, C_c, and C_m to match the circuit at both frequencies (188 MHz and 200 MHz). In the program, the preset values of C_{t1}, C_{t2}, C_c were first calculated according to Eqs. 1-3; then C_m was set to be a qualitatively correct value according to Eqs. 4-5; finally, a nonlinear root-seeking algorithm was carried out to vary all the capacitances around their preset values to successively achieve impedance matching.

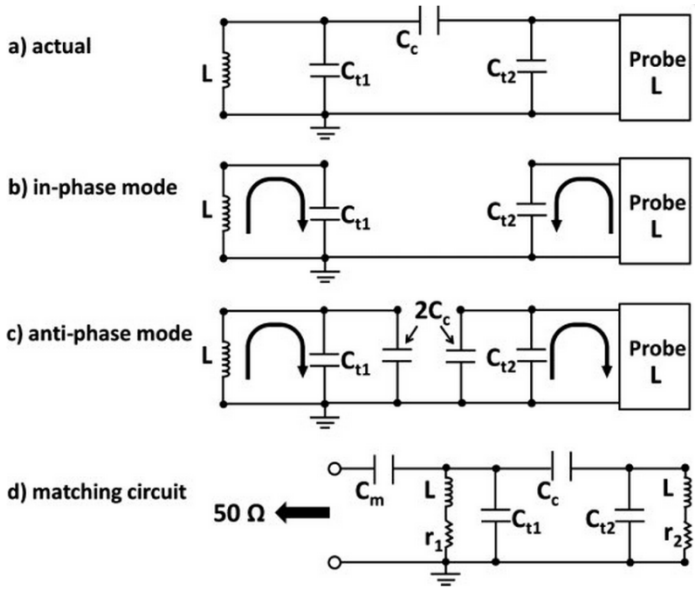

Figure 2.1 Schematic diagram of a coupled resonator circuit. (a) the resonator formed by capacitor C_{t2} and probe (with inductance L) is capacitively coupled, by capacitor C_c, to the secondary resonator formed by capacitor C_{t1} and inductor L. (b & c) the equivalent circuit of in-phase and anti-phase mode. (d) coupled resonator is capacitively matched to 50 Ohm with C_m

.

2.2.3 Implementation of two typical designs of volume coils for ^{1}H/^{19}F MRI at 4.7 T

To prove the general application of the concept, two typical designs of ^{19}F/^{1}H volume coils were implemented. The first design was a transmit/receive birdcage coil for the whole body imaging and the second design was an actively-decoupled saddle coil that can be used with other actively-decoupled ^{19}F surface coils for high resolution cardiovascular imaging. Both coils were designed to work on a Varian 4.7 T small animal scanner, with ^{19}F and ^{1}H resonant frequencies of 188 MHz and 200 MHz, respectively.

The high-pass 8-leg birdcage coil (Figure 2.2a) was built with adhesive copper tape on an acrylic tube of 50 mm diameter and 128 mm length. The whole coil was placed in a copper

shield with a diameter 135 mm and then the 1st resonant mode of the birdcage coil was tuned to 200 MHz (20). The secondary resonator was built with a tunable capacitor in parallel with a custom-made inductor, which has a diameter of 4 mm and the same inductance with the sample coil. The secondary resonator was positioned >5 cm away from the sample coil to minimize inductive coupling between two circuits. The coupling between the sample coil and secondary resonators was implemented with another tunable capacitor in series with a fixed value capacitor on the other port for the purpose of balancing. The secondary loop also was tuned to resonance at 200 MHz. The value of coupling capacitor was then adjusted to over-couple these two resonators giving rise to the second distinct frequency at 188 MHz (20). The feed point for this coil was located at the secondary resonator input and the whole circuit was matched to 50 Ohm with a tunable capacitor and fixed value capacitor.

The actively-decoupled saddle coil (Figure 2.2b) was made with adhesive copper tape on an acrylic tube of 70 mm diameter and 40 mm length. Four fixed value capacitors were evenly distributed along the coil to maintain the constant current distribution within the coil. The end of the coil was connected to fixed value capacitors in parallel with a variable capacitor. The secondary resonator was built with a custom made inductor in parallel with a fixed value capacitor and variable capacitor. The coupling and matching circuit configuration was the same as the dual-frequency birdcage and uses variable capacitors in series with fixed value capacitors. The actively decoupling method for the saddle coil was the same as mentioned in previous study (9). In order to enable the decoupling switching circuit to be compatible with the dual-frequency circuit, an RF choke (RFC) and PIN diode were inserted in the leg of the sample coil and controlled by a separate coaxial cable.

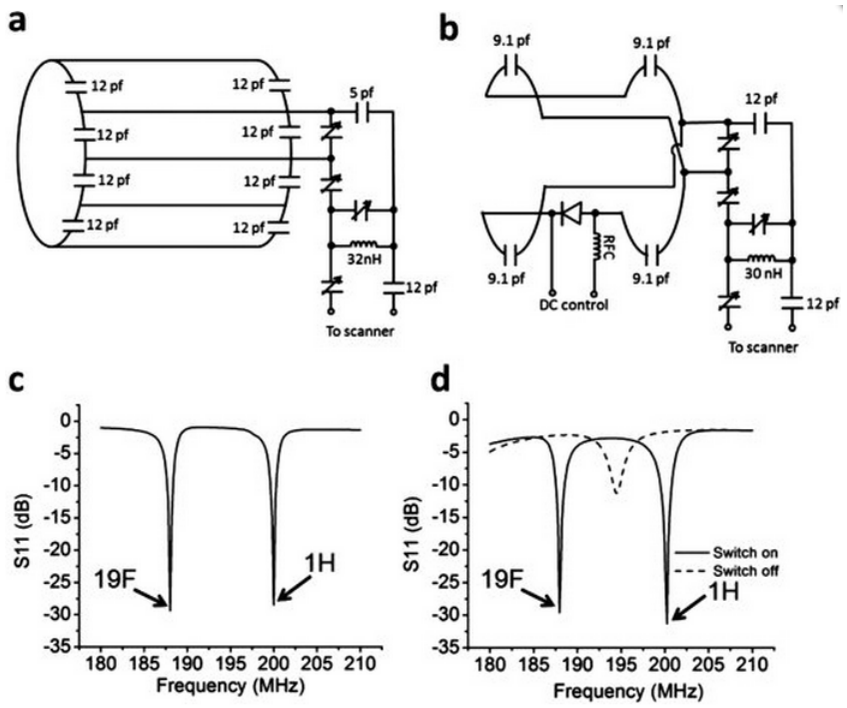

Figure 2.2 RF coil circuits and evaluation. (a) dual-frequency transmit/receive high-pass birdcage coil for 4.7 T. (b) dual-frequency actively-decoupled saddle coil for 4.7 T. (c) S_{11} of dual-frequency birdcage coil. (d) S_{11} of actively-decoupled dual-frequency saddle coil when switched on and off.

2.2.4 Bench test of electromagnetic performance

Laboratory bench tests were performed on a network analyzer (Hewlett Packard 8751A). For the tuning and matching procedure, there are a total of four variable capacitors to be adjusted for each coil. Tuning capacitors for the sample coil and secondary resonator were first adjusted to tune the two resonators to essentially the ^{1}H frequency. Then the coupling and matching capacitors were adjusted to achieve the second frequency at 188 MHz, followed by matching the dual-frequency coil impedance to 50 Ohm. The coil return loss (S_{11}) of two coils was by using a 50 ml tube filled with saline to mimic the electrical load of a live mouse. The quality factors (Q) were measured from S_{11} as described in (9). S_{21} measurement of the B1 fields produced by the

sample coils was performed with a 10 mm shielded loop for signal pick up. For the actively-decoupled saddle coil, transmission properties were measured when the coil was switched to "on" and "off" state, respectively.

2.2.5 Phantom and *in vivo* imaging

A ^{1}H image of a 50 ml tube was acquired with the dual-frequency birdcage coil or actively-decoupled coil pair (with dual-frequency transmit saddle coil and single-frequency ^{19}F surface coil), respectively. Image acquisition parameters were: pulse sequence, gradient echo; TR, 20 ms; TE, 4 ms; number of average, 1; in plane resolution: 0.4 mm * 0.4 mm; slice thickness, 0.2 mm. Normalized intensity profile was calculated along the axial direction of acquired images.

To evaluate the induced signal loss in the secondary resonator, we compared the SNR of the same phantom by setting the coil under single and double-frequency modes. Specifically, the actively-decoupled circuit of the saddle coil was manually shorted to operate the coil in transmit/receive mode. The single-frequency mode was achieved by removing the secondary resonator circuit. A 50 ml tube filled with saline and 10% perfluoro-15-crown-5-ether (CE) emulsion was imaged with a gradient echo sequence. The formulated CE emulsion is composed of 20% (or 40%) (v/v) of CE (Exfluor Research Corp., USA), 2.0% (w/v) of a surfactant commixture, and 1.7% (w/v) glycerin, with water comprising the balance (21).

The imaging quality with the transmit/receive dual-frequency birdcage coil was evaluated for whole body mouse ^{19}F imaging on the Varian 4.7 T small animal scanner. A C57Bl/6 mouse was anesthetized with a standard dose of ketamine/xylazine followed by intravenous injection of 4ml/kg CE emulsion (20% v/v). Multi-slice axial ^{1}H and ^{19}F images of the mouse body were acquired. ^{19}F MRI parameters were: pulse sequence, gradient echo; TR, 40 ms; TE, 4 ms; number of average, 1024; in plane resolution, 1.8 mm * 1.8 mm; slice thickness, 10 mm.

The efficiency of the actively-decoupled dual-frequency saddle transmit coil was demonstrated by ^{19}F angiography in a mouse (22). An actively-decoupled ^{19}F surface coil was used for receiving. Specifically, a Swiss Webster mouse was anesthetized with ketamine/xylazine as above followed by intravenous injection of 40% v/v perfluoro-15-crown-5-ether (CE) NP (5ml/kg). 2D time-of-flight and whole projection gradient echo sequences were used to acquire the ^{1}H and ^{19}F image of blood vessel in the neck, respectively (23). $^{1}H/^{19}F$ imaging parameters were: TR, 80 ms; TE, 4 ms; number of average, 4 for ^{1}H imaging and 512 for ^{19}F imaging; voxel resolution, 0.27 mm*0.27 mm*0.4 mm for ^{1}H imaging and 0.8 mm*0.4 mm*10 mm for ^{19}F imaging; 90 degree pulse width at 45 dB RF output power, 280 μs for ^{1}H and 310 μs for ^{19}F.

2.3 Results

Photographs of dual-frequency $^{1}H/^{19}F$ volume coil, the associated surface receive coil and the 4.7 T small animal MRI scanner that that was employed in this study are shown in Figure 2.3.

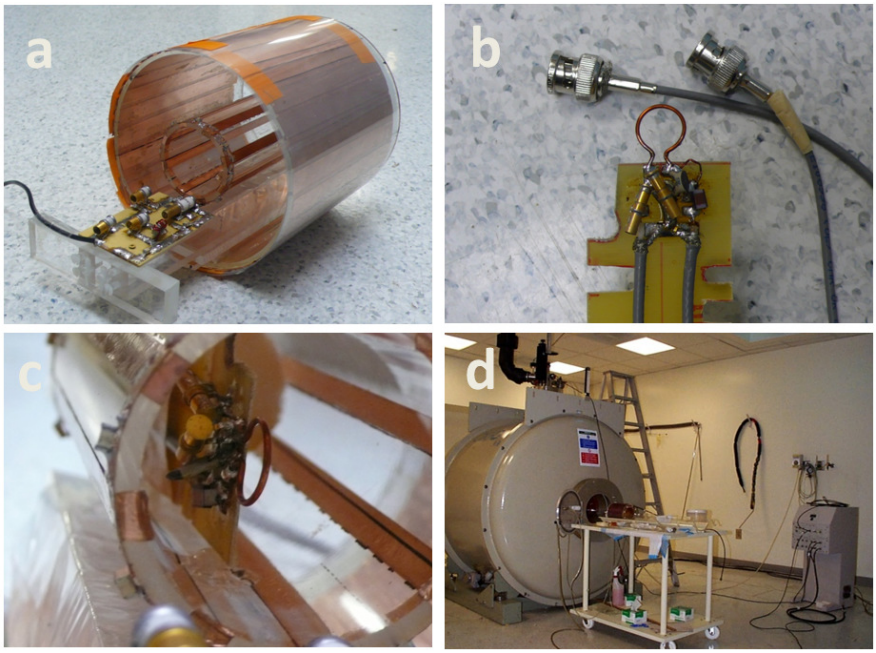

Figure 2.3 Photographs of RF coils and 4.7 T small animal scanner. (a) Double-tuned high pass birdcage coil of 50 mm in diameter placed in a copper shield with a diameter of 135mm. (b) Active decoupling surface coil as a possible choice as receiving probe. (c) Geometric and active decoupling were utilized to reduce the interference between two coils. (d) Probes were tested on Varian 4.7-Tesla ANOVA console.

2.3.1 Numerical calculation of impedance matching

Numerical solutions for the tunable capacitors to optimize impedance matching were obtained using the root-seeking program. For various combinations of internal resistances of the sample coil and secondary resonator, the calculated relative capacitances are listed in Table 1. Although the numerical results exhibited small variations (<3 pF) from the analytic solutions of the ideal coupled resonator model, they were found to closely approximate the preset analytic values, indicating that the fundamental physical features of the coupled resonator are represented in a realistic coil design.

Table 1 Nonlinear Root-Seeking of Capacitance Values for Impedance Matching

Name of variable capacitance	Preset values	Capacitance when r_1=1 Ω, r_2=0.25 Ω	Capacitance when r_1=1 Ω, r_2=1 Ω	Capacitance when r_1=0.25 Ω, r_2=0.25 Ω	Capacitance when r_1=0.25 Ω, r_2=1 Ω
C_{t1} (pf)	19.79	16.91	15.78	17.87	16.55
C_{t2} (pf)	19.79	19.48	19.54	19.65	19.60
C_c (pf)	1.27	1.25	1.39	1.30	1.40
C_m (pf)	2.00	3.44	4.36	2.13	3.39

*Inductances of both sample coil and secondary resonator are 32 nH. Resonant frequencies are 188 MHz and 200 MHz.

2.3.2 Tuning, matching, and sensitivity profile

Figure 2.2c&d depict the S_{11} of two dual-frequency coils at their working frequencies. All coils achieved impedance matching at both ^{1}H and ^{19}F frequencies. When the PIN diode was switched on, the saddle coil was detuned from both ^{1}H and ^{19}F frequencies. The unloaded Q values for birdcage and saddle coils were 200 and 144 at ^{1}H frequency; 106 and 95 at ^{19}F frequency. The loaded Q values for birdcage and saddle coils were 58 and 66 at ^{1}H frequency; 80 and 84 at ^{19}F frequency. Figure 2.4 shows the B1 field distribution, measured from corresponding coupling intensity in S_{21}, of the birdcage coil and saddle coil working at both ^{19}F and ^{1}H frequencies. For the birdcage coil, the fluctuation of magnetic field strength was less than 10% for > 60% area in radial direction and > 75% of area in axial direction (Figure 2.4a&b). When the saddle coil was switched on, the fluctuation of magnetic field strength was less than 10% for > 50% area in radial direction and > 50% area in axial direction (Figure 2.4c&d). Because the switch segment for actively-decoupling was inserted into the leg of the sample coil, when the sample coil was switched off the secondary resonator remains on frequency (Figure 2.2d) but does not produce any observable magnetic field in the region of interest (Figure 2.4c&d).

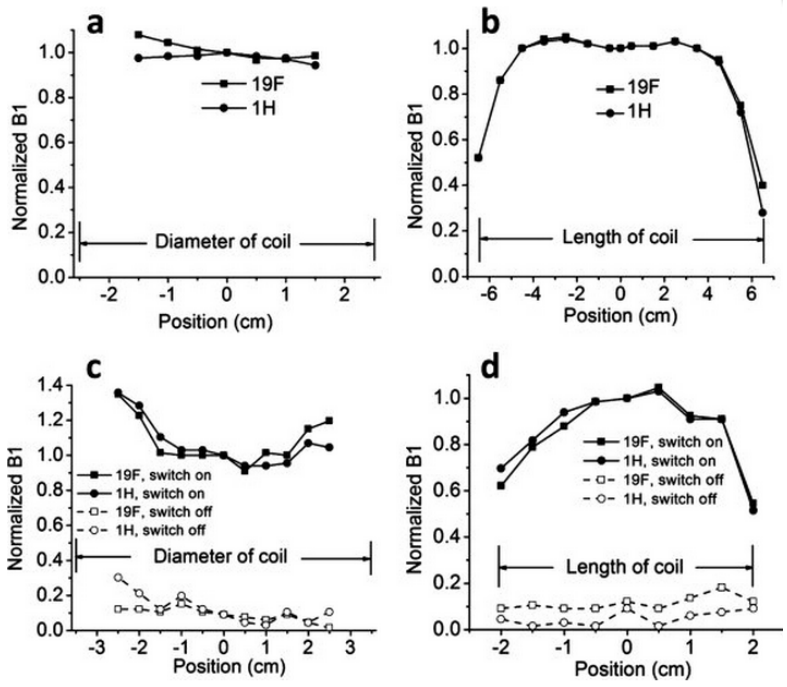

Figure 2.4 B1 field profiles of dual frequency RF coils. (a & b) normalized B1 field along the diameter and axis of the dual-frequency birdcage coil. (c & d) normalized B1 field along the diameter and axis of the actively-decoupled dual-frequency saddle coil when switched on and off.

2.3.3 $^{1}H/^{19}F$ imaging

The 90° pulse width of the single-frequency version of the saddle coil was 230/250 μs for $^{1}H/^{19}F$ frequencies. In comparison, the 90° pulse width of the dual-frequency version of the saddle coil was 300/310 μs for $^{1}H/^{19}F$ frequencies. Good homogeneity can be visually appreciated from the image intensity profile of phantom images , although dual-frequency circuit caused 50% and 25% loss of image SNR for ^{1}H and ^{19}F (Figure 2.5a-c). High sensitivity (SNR>10) was observed for the *in vivo* ^{1}H and ^{19}F imaging within the field of view (Figure 2.5d-f). The two imaging slices from the mouse body acquired with the dual-frequency birdcage coil show a high level of ^{19}F signal in the liver and heart (Figure 2.5d&e), reflecting the ^{19}F signal of

CE NP in the liver and the ventricular blood-pool. Figure 2.5f shows a coronal slice of "maximal intensity projection" of the ^{1}H and ^{19}F angiograms, wherein blood vessel geometry can be evaluated clearly. Note that the voxel size for ^{19}F imaging is greater than the diameter of mouse blood vessels; in this case larger blood vessels (jugular veins) would yield a stronger signal in a single voxel due to partial volume effects.

2.4 Discussion

Impedance matching at both frequencies is achieved by incorporating appropriate degrees of freedom (number of independent variable capacitors) within the circuit, despite the added complexity of calculating an analytical solution from the ideal coupled resonator model. Specifically, the impedance matching at two separate frequencies embeds two equations in the complex number domain or four equations in the real number domain. Thus, four independently tunable capacitors are sufficient to guarantee the existence of solutions for a good matching.

It is worth mentioning that the matched quality factor (Q) measured from S_{11} does not necessarily provide a useful measurement for a dual-frequency RF coil based on the coupled resonator. The Q value of the coil is affected by losses associated with the sample coil and the secondary LC circuit (9). In this case, alternative metrics can be exploited to assess the performance of the dual-frequency coil, e.g., imaging sensitivity test and measurement of the pulse width with given power and flip angle.

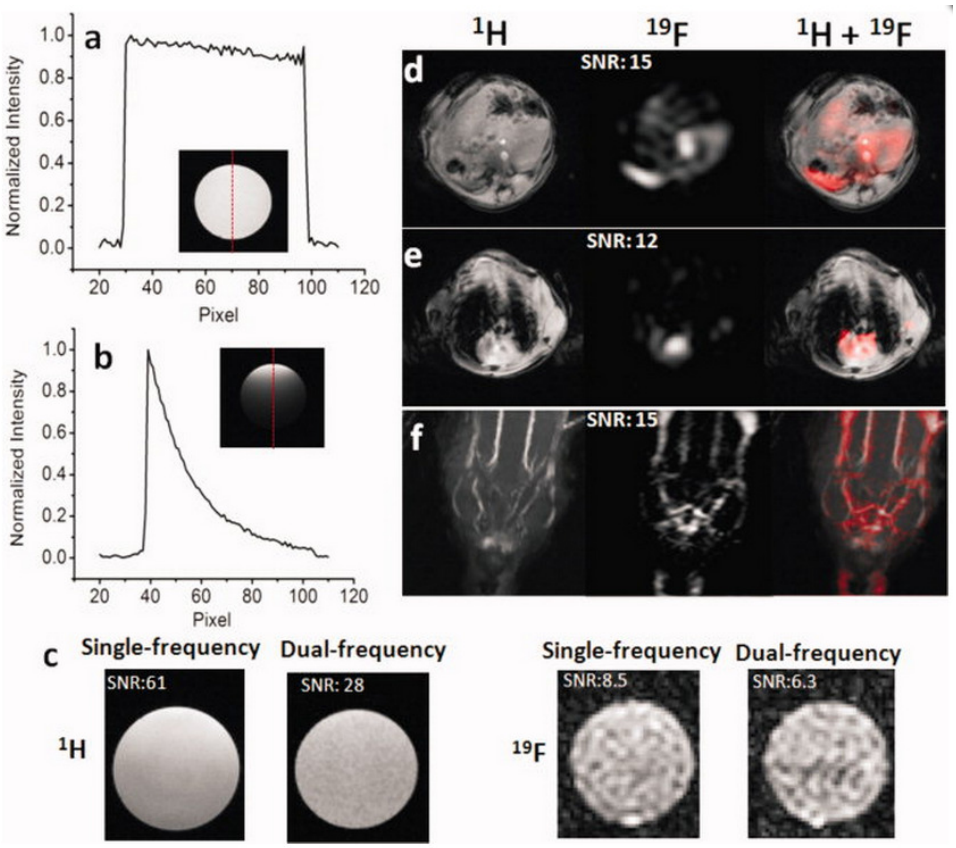

Figure 2.5 Phantom and *in vivo* test of RF coils. Sensitivity profile of proton images of a 50 ml tube filled with saline acquired with dual-frequency birdcage coil (a) and a single tuned surface receive coil in conjugation with an actively-decoupled dual-frequency saddle transmission coil (b). (c) comparison of imaging quality of single-frequency and dual-frequency versions of the same saddle coil. ^{1}H and ^{19}F images acquired with dual-frequency birdcage coil show the PFC signal in liver (d) and cardiac blood pool (e). (f) ^{1}H and ^{19}F angiography show the carotid artery and jugular vein images. Image SNR was calculated by averaging SNR in manually selected region of interest.

For certain cases of imaging of fluorinated contrast agents, which requires an extensive field of view for the ^{1}H imaging portion, the actively-decoupled saddle coil can be used as a transmit coil for ^{19}F imaging, and as a transmit/receive coil for ^{1}H imaging. In this case, a constant DC

bias is utilized to keep the volume coil on resonance for the ^{1}H image, and thus no retuning procedure is needed to switch between two imaging nuclei.

Finally, the limitations of coupled resonator paradigm for designing dual-frequency coils can be considered as follows. For well separated frequencies, the frequency-dependant inductance of the sample coil will be significantly different at two working frequencies. However, it is difficult to implement a small copper loop inductor that has the same frequency-dependent inductance as the sample coil, and thus it will hinder the equivalence of sample coil and secondary resonator. The "in-phase" and "anti-phase" modes, as described previously, will not form as expected. Therefore, the strategy of using the coupled resonator model to fabricate a dual-frequency MRI coil is only suitable for close Larmor frequencies, e.g., $^{19}F/^{1}H$ and $^{13}C/^{23}Na$.

In conclusion, the present work describes a generalized strategy for designing $^{19}F/^{1}H$ dual-frequency coils based on the coupled resonator approach. The tested birdcage and actively-decoupled saddle coil at 4.7 T, as well as previously reported solenoid coil and open coil at 3 T (15,19), demonstrated that this coil design can be readily adapted to diverse coil structures at different fields strengths. A unique feature of this design is that it preserves the B1 field homogeneity of the RF coil at both resonant frequencies. By minimizing the susceptibility effect on image co-registration, this coil design enables direct co-registration of ^{19}F and ^{1}H images for localizing delivered ^{19}F agent. Because the size of the inductor in the secondary resonator is much smaller than the sample coil and it is positioned distal to the sample coil to minimize mutual uncontrolled inductive coupling between the two resonators, the secondary resonator inductor did not induce detectable perturbations of the magnetic field of the sample coil, nor loss of filling factor (16). Finally, the nonlinear root-seeking procedure proposed in the current work can effectively calculate numerical solutions for the appropriate values of tunable capacitors. In

conclusion, in view of the anticipated utility of simultaneous ^{1}H and ^{19}F imaging and the potential availability of molecular imaging contrast agents with high ^{19}F content this strategy may facilitate ultimate clinical adoption of such molecular imaging approaches given the availability of multispectral imaging systems (1).

2.5 References

1. Wickline SA, Mason RP, Caruthers SD, Chen J, Winter PM, Hughes MS, Lanza GM. Fluorocarbon agents for multimodal molecular imaging and targeted therapeutics. In: Weissleder R, Ross BD, Rehemtulla A, Gambhir SS, editors. Molecular Imaging: Pmph Usa; 2010. p 542-573.
2. Lanza GM, Winter PM, Neubauer AM, Caruthers SD, Hockett FD, Wickline SA. 1H/19F magnetic resonance molecular imaging with perfluorocarbon nanoparticles. Curr Top Dev Biol 2005;70:57-76.
3. Cron GO, Beghein N, Ansiaux R, Martinive P, Feron O, Gallez B. 19F NMR in vivo spectroscopy reflects the effectiveness of perfusion-enhancing vascular modifiers for improving gemcitabine chemotherapy. Magn Reson Med 2008;59(1):19-27.
4. Ikehira H, Girard F, Obata T, Ito H, Yoshitomi H, Miyazaki M, Nakajima N, Kamei H, Kanazawa Y, Takano H, Tanada S, Sasaki Y. A preliminary study for clinical pharmacokinetics of oral fluorine anticancer medicines using the commercial MRI system 19F-MRS. Br J Radiol 1999;72(858):584-589.
5. de Alejo RP, Garrido C, Villa P, Rodriguez I, Vaquero JJ, Ruiz-Cabello J, Cortijo M. Automatic tuning and matching of a small multifrequency saddle coil at 4.7 T. Magn Reson Med 2004;51(4):869-873.

6. Tomanek B, Volotovskyy V, Gruwel MLH, McKenzie E, King SB. Double-frequency birdcage volume coils for 4.7T and 7T. Concept Magn Reson B 2005;26B(1):16-22.

7. Brix G, Schlicker A, Mier W, Peschke P, Bellemann ME. Biodistribution and pharmacokinetics of the (19)F-labeled radiosensitizer 3-aminobenzamide: assessment by (19)F MR imaging. Magn Reson Imaging 2005;23(9):967-976.

8. Hu SL, Reimer JA, Bell AT. Single-input double-tuned circuit for double resonance nuclear magnetic resonance experiments. Rev Sci Instrum 1998;69(2):477-478.

9. Mispelter J, Lupu M, Briguet A. NMR probeheads for biophysical and biomedical experiments : theoretical principles & practical guidelines. London Hackensack, NJ: Imperial College Press ; Distributed by World Scientific; 2006. xiv, 596 p. p.

10. Lanza GM, Winter PM, Caruthers SD, Hughes MS, Hu G, Schmieder AH, Wickline SA. Theragnostics for tumor and plaque angiogenesis with perfluorocarbon nanoemulsions. Angiogenesis 2010;13(2):189-202.

11. Li Y, Logan TM, Edison AS, Webb A. Design of small volume HX and triple-resonance probes for improved limits of detection in protein NMR experiments. J Magn Reson 2003;164(1):128-135.

12. Lanz T, Ruff J, Weisser A, Haase A. Double tuned Na-23 H-1 nuclear magnetic resonance birdcage for application on mice in vivo. Rev Sci Instrum 2001;72(5):2508-2510.

13. Fitzsimmons JR, Beck BL, Brooker HR. Double Resonant Quadrature Birdcage. Magnet Reson Med 1993;30(1):107-114.

14. Joseph PM, Lu DF. A Technique for Double Resonant Operation of Birdcage Imaging Coils. Ieee T Med Imaging 1989;8(3):286-294.

15. Mazurkewitz P, Leussler C. Double Resonant Transmit Receive Solenoid Coil For MRI. US Patent 2009.

16. Doty FD, Entzminger G, Kulkarni J, Pamarthy K, Staab JP. Radio frequency coil technology for small-animal MRI. Nmr Biomed 2007;20(3):304-325.

17. Alecci M, Romanzetti S, Kaffanke J, Celik A, Wegener HP, Shah NJ. Practical design of a 4 Tesla double-tuned RF surface coil for interleaved 1H and 23Na MRI of rat brain. J Magn Reson 2006;181(2):203-211.

18. Haase J, Curro NJ, Slichter CP. Double resonance probes for close frequencies. J Magn Reson 1998;135(2):273-279.

19. Hockett F, Wallace K, Schmieder A, Caruthers S, Pham C, Wickline S, Lanza G. Simultaneous Dual Frequency and Open Coil Imaging of Arthritic Rabbit Knee at 3T. IEEE Trans Med Imaging 2010.

20. Jin J-M. Electromagnetic analysis and design in magnetic resonance imaging. Boca Raton: CRC Press; 1998. xiv, 282 p. p.

21. Neubauer AM, Myerson J, Caruthers SD, Hockett FD, Winter PM, Chen JJ, Gaffney PJ, Robertson JD, Lanza GM, Wickline SA. Gadolinium-Modulated F-19 Signals From Perfluorocarbon Nanoparticles as a New Strategy for Molecular Imaging. Magnet Reson Med 2008;60(5):1066-1072.

22. Neubauer AM, Caruthers SD, Hockett FD, Cyrus T, Robertson JD, Allen JS, Williams TD, Fuhrhop RW, Lanza GM, Wickline SA. Fluorine cardiovascular magnetic resonance angiography in vivo at 1.5 T with perfluorocarbon nanoparticle contrast agents. J Cardiovasc Magn R 2007;9(3):565-573.

23. van Bochove GS, Straathof R, Krams R, Nicolay K, Strijkers GJ. MRI-determined carotid artery flow velocities and wall shear stress in a mouse model of vulnerable and stable atherosclerotic plaque. Magn Reson Mater Phy 2010;23(2):77-84.

3 NMR physics of PFC NP

3.1 J-coupling of PFC NP

3.1.1 Background

In high resolution liquid NMR spectroscopy, there are two major mechanisms for spin-spin interaction. The strongest one is the direct dipole-dipole interaction between nuclear spins; and the other one is the indirect dipole-dipole interaction between nuclear spins mediated through electron spins. The first type of interaction (which will be discussed in greater detail in the next chapter) affects the NMR relaxation properties, (e.g., T1 and T2) of nuclear spins but does not lead to splitting of singlet resonant peaks into multiples because this effect is usually averaged out by fast molecular tumbling. The second type, however, generally results in peak splitting at the level of Hz for high resolution NMR. The indirect dipole-dipole interaction is also called J-coupling, or scalar coupling, because the coupling terms in the Hamiltonian of nuclear spins can be described as scalars (1-2).

In a weak coupling system, in which J-coupling constant is much smaller than the chemical shift difference among heterogeneous chemical groups, J-coupling is only related to the z component of the spins. In liquid NMR, the J-couplings in most PFC molecules (e.g., the coupling between CF_3 and CF_2, CF_2Br and CF_2 groups in perfluorooctylbromide (PFOB) molecule) are weak couplings. In most MRI scanners, because the imaging subjects are usually much larger than NMR tubes and hence pose more complicated geometry and chemical composition, B0 shimming over a larger spatial range is significantly coarser than that in NMR spectroscopy. For example, the typical full width at half maximal (FWHM) of a ^{1}H (or ^{19}F) spectrum for animal imaging at 4.7 T *in vivo* is ~100 Hz, which is an order of magnitude larger

than the J-coupling frequency. Hence instead inducing of peak splits, J-coupling in ^{19}F MRI causes amplitude modulation of ^{19}F resonant peaks, i.e., J-modulation (2-3).

J-modulation originates from the phase difference among different peaks in a J-coupling induced multiplet. Because of J-modulation, the regular T2 decay of ^{19}F nuclear spins becomes modulated into sinusoidal oscillations, the frequency of which is dependent on the J-coupling constant. Unlike field inhomogeneity, J-modulation is an intrinsic property associated with the molecular structure (independent of B0 field strength) and cannot be refocused by spin echoes. Such an oscillating behavior with regarding to the time of echo (TE) in spin echo imaging sequences dramatically shortens the apparent T2 value and reduces the detectable signal intensity in ^{19}F imaging. On the other hand however, because the J-modulated spin echo signal is completely eliminated when TE=1/2J, this unique feature might also be employed as an imaging approach for selectively switching on/off certain PFC signals by adjusting the TE (4).

In the present work, we aimed to study the relationship between RF bandwidth and J-coupling modulation in ^{19}F MRI of PFOB NP. The chemical structure and NMR spectrum of PFOB are shown in Figure 3.1. Because the CF_3 group yields a 50% higher MR signal as compared to other CF_2 groups, it is usually chosen as the central frequency for excitation and readout. The ^{19}F nuclear spins in CF_3 and the adjacent CF_2 form a typical "A_2B_3" J-coupling system with a coupling constant of 12.3 Hz (4-6). In most practical imaging applications, J-modulation of CF_3 peak in spin echo imaging could be different from that in a simple spectroscopic experiment because imaging RF pulses (i.e., excitation (90°) and refocusing (180°) pulses) usually manifest relatively limited bandwidth so as to accommodate the slice selection imaging gradients. Therefore in order to achieve consistent quantitative ^{19}F MRI of PFOB NP it

is important to understand the dependency of J-modulation of CF_3 group in PFOB on the bandwidth of RF pulses (7).

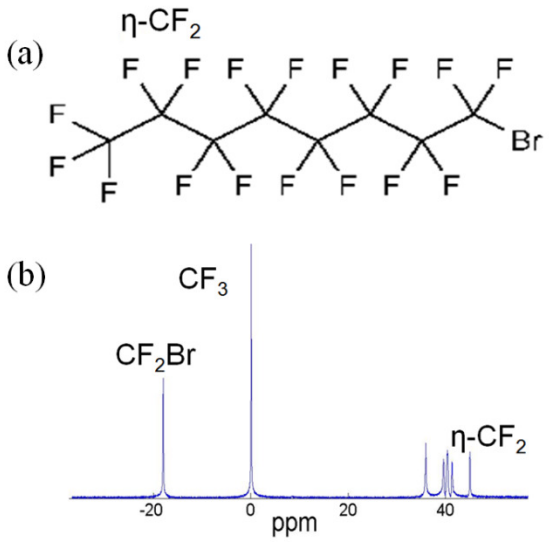

Figure 3.1 Chemical structure and NMR spectrum of PFOB. (a) Chemical structure of PFOB molecule, the J-coupling constant between CF_3 and the adjacent CF_2 group is 12.3 Hz. (b) Representative MR spectrum of PFOB.

3.1.2 Methods

Theoretical calculation

The Hamiltonian of the subsystem consisting of CF_3 and CF_2 groups in PFOB molecule can be written as

$$H = \Omega_{CF2}(I_{z1} + I_{z2}) + \Omega_{CF3}(I_{z3} + I_{z4} + I_{z5}) + 2\pi J(I_{z1}I_{z3} + I_{z1}I_{z4} + I_{z1}I_{z5} + I_{z2}I_{z3} + I_{z2}I_{z4} + Iz2Iz5, \quad [1]$$

where I_z's are the z-component of the angular moment of ^{19}F nuclear spins , Ω's denote the chemical shift for each group, and J is the coupling constant between two groups which is 12.3 Hz in PFOB. The initial state of this five spin sub-system, in the form of density matrix, before any RF pulses are played out is

$$\rho_i = I_{z1} + I_{z2} + I_{z3} + I_{z4} + I_{z5}. \qquad [2]$$

For RF pulses with finite bandwidth and centered at CF_3 frequency, the quantum operator format of a 90° pulse along x axis is

$$R_x\left(\frac{\pi}{2}\right) = e^{-f\frac{\pi i}{2}I_{x1}} \otimes e^{-f\frac{\pi i}{2}I_{x2}} \otimes e^{-\frac{\pi i}{2}I_{x3}} \otimes e^{-\frac{\pi i}{2}I_{x4}} \otimes e^{-\frac{\pi i}{2}I_{x5}}, \qquad [3]$$

where I_x's are the x-component of angular moment of ^{19}F nuclear spins, $\otimes$ denotes outer product, and $f = \vartheta(CF2)/\vartheta(CF3)$ is the flip angle ratio between CF_2 and CF_3 group caused by the power drop down at CF_2 peak from the central frequency due to the limited RF bandwidth. Similarly, the operator format of a 180° refocusing pulse along x axis is,

$$R_x(\pi) = e^{-f\pi i I_{x1}} \otimes e^{-f\pi i I_{x2}} \otimes e^{-\pi i I_{x3}} \otimes e^{-\pi i I_{x4}} \otimes e^{-\pi i I_{x5}}, \qquad [4]$$

where f factor is identical to that in 90° pulses, which is in agreement with the RF setting of our Varian small animal imaging system.

Applying the Schrodinger equation, the operator describing the time evolution of a quantum state over time t can be written as

$$U(t) = e^{-tiH}, \qquad [5]$$

where H is the Hamiltonian of the system. Therefore, in a regular spin echo imaging sequence, the density matrix of the final state of the coupled CF_3-CF_2 subsystem can be calculated as

$$\rho_f = \left[U\left(\frac{TE}{2}\right) \cdot R_x(\pi) \cdot U\left(\frac{TE}{2}\right) \cdot R_x\left(\frac{\pi}{2}\right)\right]^{\dagger} \cdot \rho_i \cdot U\left(\frac{TE}{2}\right) \cdot R_x(\pi) \cdot U\left(\frac{TE}{2}\right) \cdot R_x\left(\frac{\pi}{2}\right). \qquad [6]$$

Here we do not consider the regular T2 decay in the transverse plane. To account for T2 decay, we only need to multiply the final state function by a scalar $e^{-TE/T2}$.

As the last step in the NMR/MRI experiment, when we measure magnetization in the transverse plane, the final signal intensity of CF_3 in a spin echo sequence can be calculated by taking trace of the product of density matrix with the transverse angular momentum operator:

$$S = e^{-TE/T2} \cdot Tr[\rho_f \cdot (I_{x3} + I_{x4} + I_{x5})]. \quad [7]$$

All calculations were performed analytically in a custom-designed program written in Mathematica (Wolfram, USA).

Experimental investigation of J-modulation in ^{19}F MRI

High resolution NMR spectroscopy of PFOB NP was performed at a 7T Varian spectrometer. The sample was set spinning on an air cushion to improve B0 field homogeneity and a regular single pulse spectrum was acquired with TR = 10 s. To validate J-modulation, we performed spin echo spectroscopy of a 50 ml test tube containing 1% PFOB NP at Varian 4.7 T small animal scanner using a custom-built solenoid RF coil. In this experiment, TR=10 s, and TE was varied from 1 ms to 300 ms to capture the J-modulation profile of CF_3 peak. MR spectroscopic quantification of PFOB content in the phantom was performed using an identical spin echo sequence with another sample of CE NP as an external reference. During the experiments, the bandwidths of both the 90° and 180° RF pulses were changed to examine the dependency of J-modulation on RF bandwidth.

Application of J-modulation on selective imaging

We performed a phantom study to demonstrate the use of J-modulation for selective ^{19}F MRI where PFOB was intentionally suppressed while a different type of PFC NP was selected for imaging. We filled an NMR tube with CE NP and inserted it into a larger glass bottle (1 cm in diameter). The empty space between two containers was filled with PFOB NP. Spin echo imaging in the transverse plane of the phantom was performed at 4.7 T with TR = 2 s, TE=10 and 44 ms respectively, voxel size = 0.2 mm × 0.2 mm × 2 mm. The corresponding PFOB spectroscopy also was acquired using a spin echo spectroscopy sequence with the identical TR/TE values.

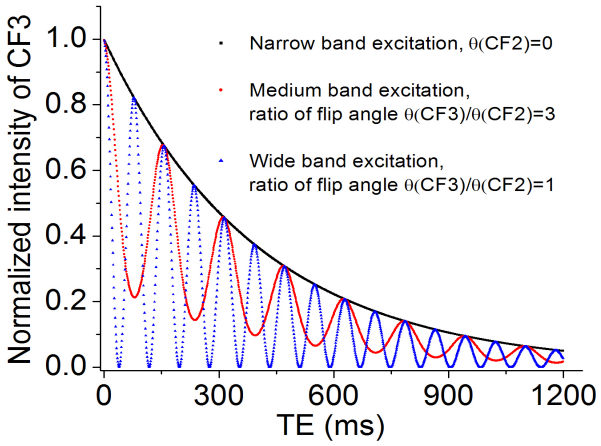

Figure 3.2 Theoretically calculated J-modulation profile of CF_3 peak in PFOB molecule for different RF bandwidth. Narrow band excitation RF pulse reduces the effect of J-coupling according to theoretical calculation.

3.1.3 Results

Theoretical calculation of the J-modulation profile for different RF bandwidths (f value) is presented in Figure 3.2. Three representative scenarios were considered. (1) Extremely narrow excitation/refocusing bandwidth: RF power was only transmitted to the CF_3 group while CF_2 group was not affected, and PFOB did not exhibit any J-modulation induced amplitude oscillation in this case. (2) Extreme wide band excitation/refocusing: both the CF_2 and CF_3 groups were fully excited and refocused. Maximal J-modulation was observed for the CF_3 peak in this case. It is notable that at certain discrete points, when $TE = (2n + 1)/2J$ ($n > 0$ is an integer), the signal intensity of the CF_3 peak was completely suppressed by J-modulation. (3) With the use of a medium RF bandwidth for excitation/refocusing, both the oscillation amplitude and the frequency of J-modulation were decreased.

Under conditions of high resolution MR spectroscopy (Figure 3.3a), we observed that J-coupling caused splitting of the CF_3 singlet into a triplet, as expected. The frequency difference

between two adjacent peaks in the triplet was J and the absolute intensity ratio among these peaks was approximately 1:2:1. By comparison, in low resolution spin echo spectroscopy, we observed that the intensity of the CF_3 peak was highly modulated when we varied TE. However, if the RF bandwidth was narrowed, or if all of the RF pulses were highly selective, the CF_3 peak did not exhibit any J-modulation effect (Figure 3.3b&c), which accorded with our theoretical calculation. The quantification of PFOB concentration with the use of a CE NP standard varied with both TE and RF pulse width (Figure 3.4). This result suggests that ^{19}F spectroscopic quantification is highly dependent on the choice of TE and pulse width. Therefore a shorter TE and a fixed choice of RF bandwidth should always be preferable in order to achieve consistent quantification.

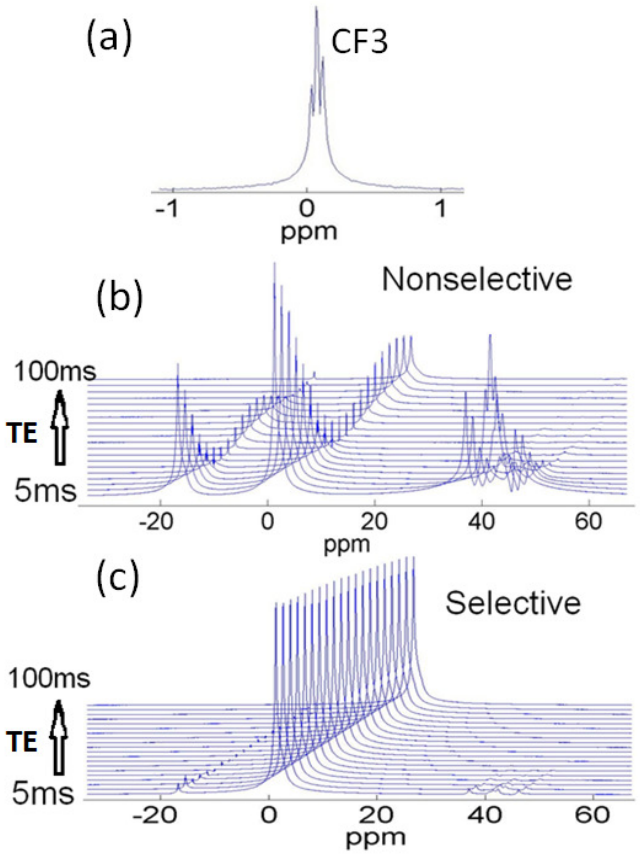

Figure 3.3 NMR spectra of PFOB under different resolution and RF bandwidth. (a) High resolution NMR spectroscopy of the CF_3 peak revealed peak split due to J-coupling. (b & c) J-modulation under nonselective and selective RF pulses.

To demonstrate the utility of J-modulation to suppress background PFOB signal, from the PFOB spectroscopy, we suggest that a choice of TE = 44 ms might lead to a much lower CF_3 signal intensity as compared with other peaks, and a total elimination of PFOB background when imaging the other PFC component (which here is CE) selectively (Figure 3.5).

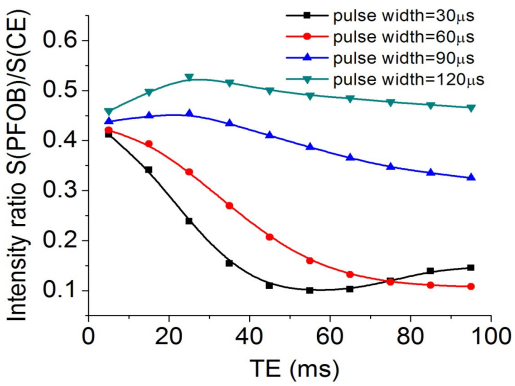

Figure 3.4 J-coupling effect on the acquired ^{19}F MR signal from a PFOB phantom relative to that of a CE standard. The relative signal strength of PFOB, reflecting ^{19}F MRI measured "quantity" of PFOB, varied at different excitation pulse width and TE, suggesting fixed pulse width (or bandwidth in the frequency domain) is required for quantitative PFOB MR spectroscopy.

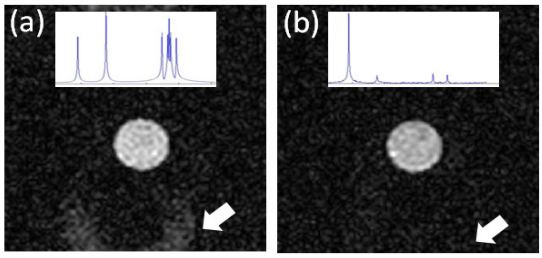

Figure 3.5 Images (and correpsonding spectra) of PFOB and CE with nonselective excitation. The center disk corresponds to CE while the outer circle rings correspond to the chemical shift of the CF_3 peak from PFOB.

3.1.4 Conclusion

In this section, we have proposed a general theoretical framework for evaluating J-modulation of PFOB in MR spectroscopy and imaging. We incorporated into our model the effect of finite RF bandwidth and theoretically proved that narrow band excitation/refocusing could reduce or even eliminate J-modulation effect in a spin echo sequence. High resolution and low resolution spectroscopy of PFOB NP confirmed the J-coupling induced peak spliting and J-

modulation of the CF_3 group. Furthermore, by carefully choosing the TE value in a spin echo imaging experiment, we could selectively switch on/off signal from the CF_3 peak in PFOB.

3.2 Oxygenation effect on the absolute quantification of ^{19}F MRI

3.2.1 Background

The unique ^{19}F MR signature of PFC NP has been exploited for conducting quantitative MRI because practically no background signal emanates from physiological tissue (8). However, the spin-lattice relaxation time (T1) of PFC emulsion is inversely correlated with oxygen concentration, which varies in different tissues (e.g., in tumor and artery). Therefore, it is necessary to choose *in vivo* acquisition parameters that minimize the oxygenation effect on quantitative ^{19}F MRI-determined regional concentrations of PFC NP (9). Additionally, acquisition parameters should be optimized to maximize the SNR, which is a general concern for *in vivo* ^{19}F MR applications. In this study, the effect of TR and TE on the accuracy of quantitative ^{19}F MR were evaluated by mathematical simulation followed by *in vivo* validation.

3.2.2 Methods

Effect of oxygenation on ^{19}F T1

In vitro measurement of ^{19}F R1 as a function of pO_2 was acquired at selected O_2 concentrations (ranging from 0% to 100% O_2 balanced with N_2) by bubbling a gas mixture into a neat PFOB sample, a PFOB NP sample, a neat CE sample, and a CE NP sample for 30 minutes at room temperature. Experiments were performed on a 4.7 Varian small animal scanner, and ^{19}F T1 measurements were made using inversion recovery spectroscopy with TR=10 s, and 10 inversion delays (TI) ranging from 3 ms to 5 s.

Simulation

Starting from the Bloch equations, simulations of spin echo spectroscopy sequences were preformed in Matlab (Mathworks, Inc.). First, the expected ^{19}F signal intensity as a function of TR and TE was simulated to assess SNR. Subsequently, two simulations were conducted by setting the ^{19}F T1 relaxation time of PFC NP to 0.9 s, thereby simulating normoxic conditions (21% [O_2]), and 0.6 s, simulating hyperoxic conditions (100% [O_2]) (10). The calculated oxygenation-induced quantification error was plotted as a function of TR and TE. The T2 for all simulations was set to be 0.3 s. The quantification fidelity was defined as $S_{normoxia}/S_{hyperoxia}$, or the ratio of signal intensity between normoxia and hyperoxia.

***In vivo* ^{19}F MRI/S**

MR experiments were performed on an 11.7T Varian INOVA MR system. Three C57/BL6 mice under room air ventilation were intravenously injected with 20% v/v CE NP emulsion (4 mL/Kg) through the tail vein. At 3-hour post injection, mice were anesthetized with a standard dose of ketamine/xylazine. A solenoid ^{19}F coil was placed on the right rear leg of the mice for *in vivo* imaging. A ^{1}H scout image of the leg was first acquired to visualize the anatomy. Subsequently, a T1-weighted spin-echo ^{19}F image (TR = 350 ms, TE = 16 ms) was acquired to visually examine the ^{19}F signal intensity, followed by ^{19}F T1 measurement using an inversion recovery spin-echo sequence (TR = 5 s, TI increases from 5 ms to 1.8 s with 0.2 s interval). Finally, quantification of regional PFC NP concentration was conducted with a previously reported ^{19}F MR spin-echo spectroscopic method (TR = 0.3, 2.0, and 3.0 s) using trifluoroacetic acid (TFA) sealed in a pipette tip as a reference standard. Two sets of images were acquired for each mouse when breathing room air (normoxia condition) or 100% oxygen

(hyperoxia condition). Other parameters for ^{19}F imaging were: RF excitation bandwidth, 350 Hz; number of average, 128; in plane resolution: 1mm × 1mm; slice thickness: whole projection.

3.2.3 Results

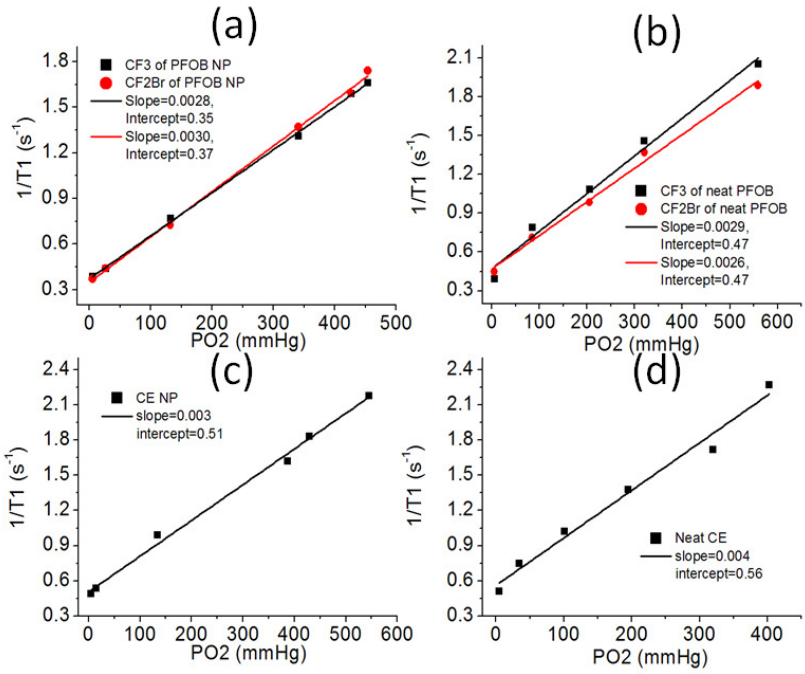

Figure 3.6 Longitudinal relaxation rate of PFC NP and neat PFC liquid as a function of pO_2 at 4.7 T.

R1 (longitudinal relaxation rate: 1/T1) of CE NP and different chemical groups in PFOB as a function of oxygen tension are summarized in (Figure 3.6). R1 of neat PFC and PFC NP were dependent on the oxygenation level, and the slope for the neat form was very close to that for the NP form of the same PFC component. Moreover, the CF_3 and CF_2Br group in PFOB also responded to oxygenation in a similar manner.

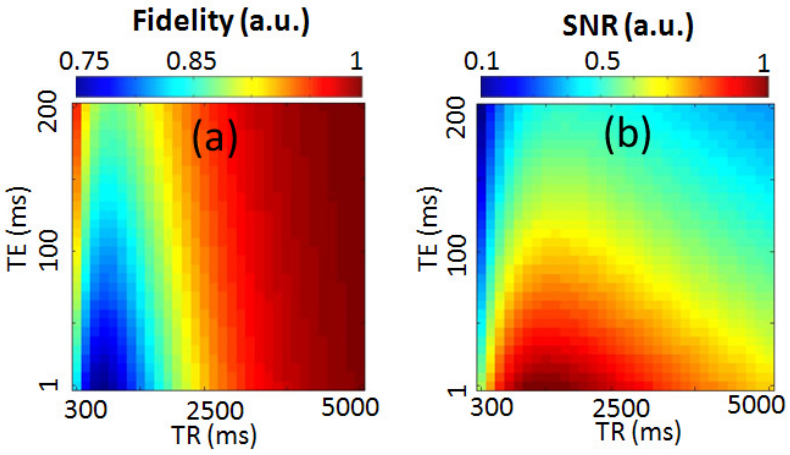

Figure 3.7 The relation between ^{19}F quantification and TR/TE (simulation result). (a) Measurement fidelity (the ratio between ^{19}F intensity under normoxia and hyperoxia) of the simulated ^{19}F signal intensity for T1 = 0.9 s (normoxia) and 0.6 s (hyperoxia) at various TR. T2 was set to be 0.3 s. (b) The normalized SNR of ^{19}F MRI as a function of TR and TE within the same data acquisition time. T1 was set to be 0.9 s and T2 was set to be 0.3 s.

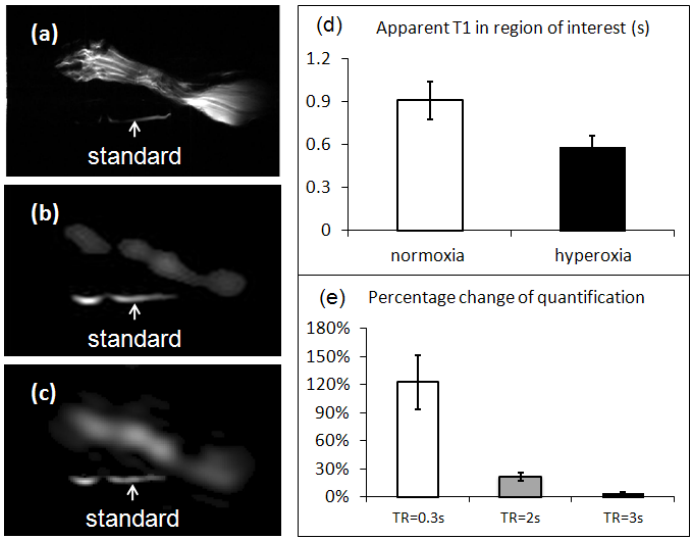

Figure 3.8 Dependence of ^{19}F quantification on TR (*in vivo* result). (a) High resolution ^{1}H image shows the position of the mouse leg and a TFA calibration standard (arrows). (b and c) T1 weighted ^{19}F image of mouse leg when the animal was under normoxia (b) or hyperoxia (c). (d)

Quantified ^{19}F T1 of CE NP in mouse leg under normoxia and hyperoxia. (e) T1 and quantification difference (in percentage) of CE NP using different TR.

Figure 3.7 shows the simulation result. The optimal parameter for achieving the highest SNR is TR≈1.5*T1. Additionally, the quantification difference between normoxia and hyperoxia conditions was less than 5% when TR ≥ 3 *T1. Figure 3.8 shows *in vivo* ^{19}F MR result of mouse leg after PFC NP treatment. T1-weighted ^{19}F signal in mouse leg under normoxia was apparently lower than that under hyperoxia. Correspondingly, a ~50% decrease of ^{19}F T1 was observed from normoxia to hyperoxia conditions. Because of the oxygenation effect on ^{19}F T1, a more than 100% quantification error of PFC NP concentration was observed when TR = 0.3 s. However, the quantification error was insignificant when TR = 3 s, i.e., ≥ 3*T1.

3.2.4 Discussion

We demonstrated that ^{19}F MRI-determined PFC NP quantity was not sensitive to local oxygenation when TR> 3*T1. Results from mathematical simulations were in agreement with those determined from *in vivo* experiments. In clinical situations, tissue oxygenation is inhomogeneous in various organs such as tumors. Thus, a long TR (over 3 times T1) should be used for *in vivo* studies to guarantee that ^{19}F MRI-determined PFC concentration accurately reflects the ^{19}F spin-density.

3.3 "Multi-chromatic" ^{19}F MRI

3.3.1 Background

Conventional ^{1}H MRI only affords a mono-chromatic readout of a single biomarker because water exhibits a single resonant frequency inside an external magnet. When the need for

simultaneous characterization of multiple biomarkers arises, alternative imaging approaches must be employed to generate multi-chromatic images to distinguish different types of biochemical targets. With unique ^{19}F signals emanating from the core, PFC NPs enable a direct and quantitative readout of biomarkers with the use of ^{19}F MRI. In contrast to organic molecules that are rich in proton atoms, PFCs exhibit a widely spread chemical shift (~100 ppm) (11). Recently, Sirinvias et al demonstrated the feasibility of manufacturing functional nanoparticles from five different PFC species (12). Because different PFC molecules manifest distinct ^{19}F spectroscopic signatures, detection and identification of each PFC could be realized in one sample containing multiple PFCs. The feasibility of imaging two PFC components individually was first discussed by Mason et al, even though the PFC itself was not functionalized as a targeting contrast agent in their study (2). The first selective bi-chromatic imaging for two different PFCs as a molecular contrast agent was demonstrated *ex vivo* by Caruthers et al (13). However, the technical requirement for imaging multiple (>3) PFC species and the potential biomedical application of multi-chromatic ^{19}F MRI with PFC NPs demands further experimental validation.

3.3.2 Methods

Multi-chromatic ^{19}F MRI with extreme narrow RF bandwidth

All NMR spectroscopy and MRI in this study were performed on an 11.7 T Varian scanner. For phantom imaging, five NMR tubes were filled with five previously studied neat PFC components, i.e., Perfluorooctyl-Bromide ($C_8F_{13}Br$, PFOB), Perfluorodecalin ($C_{10}F_{18}$, PFD), Perfluoro-12-Crown-4-Ether ($C_8F_{16}O_4$, PF-12-CE), Perfluoro-15-Crown-5-Ether ($C_{10}F_{20}O_5$, PF-15-CE or CE) and Perfluorooctane (C_8F_{18}, PFO), respectively. NMR spectra of each of these PFCs were acquired using a regular single pulse spectroscopy sequence with a

broad excitation and receiving bandwidth of 30 kHz and 40 kHz respectively. After acquiring the NMR spectra, one resonant peak of each PFC was chosen as the "signature frequency," which could be selectively imaged for ^{19}F multi-chromatic MRI. One chemical shift was selected as a signature frequency based on the following criteria: (1) the signature frequency of one PFC should not overlap with any resonant frequencies from any other PFCs; (2) the separation between any two selected signature frequencies should be as wide as possible; (3) if multiple peaks exist and meet criteria (1) and (2), the one that exhibits the strongest NMR signal should be chosen. Finally, the signature frequency of each of PFC was determined to be: 26.8 ppm for PFOB, -23.9 ppm for PFD, 1.7 ppm for PF-12-CE, 0 ppm for PF-15-CE, and 17.5 ppm for PFO, respectively.

For multi-chromatic imaging, all five NMR tubes containing the aforementioned PFC species were placed inside a 50 ml tube filled with DI water. A fast spin echo sequence (FSE) was employed to identify each PFC separately by selectively exciting and refocusing at the signature frequencies. In order to realize complete separation and avoid potential cross talk among different PFCs, we employed a sinc shape pulse with 8 ms duration for both 90° and 180° pulses in the FSE sequence. The frequency bandwidth of such a long pulse was as narrow as 700 Hz, which is sufficient to distinguish between the closest spaced signature frequencies of all five PFCs. Other imaging parameters were: echo train length = 8, TR = 2 s, TE = 20 ms, in plane resolution = 0.25 × 0.25 mm, slice thickness = 1 cm. After ^{19}F MRI, transmit and receive offset was switched to ^{1}H frequency and a regular gradient echo sequence was employed to acquire a ^{1}H image to visualize the structure of the phantom. The parameters for ^{1}H MRI were TR = 100 ms, TE = 5 ms, in plane resolution = 0.25 × 0.25 mm, slice thickness = 1 cm, flip angle = 30°.

Multi-chromatic MRI in macrophage cellular imaging

RAW 267.3 macrophage cells (n=3 for each group) were cultured in gelatin coated T75 flask to reach around 80% confluence, and a mixture of CE NP and PFOB NP was added to the culture media at concentrations of 2, 5, 10 and 20 µl/ml. The mixed PFC NP contained 75% volume fraction of plain PFOB NP and 25% of plain CE NP. After 2-hour incubation, flasks were washed with PBS for 3 times and then cells were counted, harvested and spun down to form loose pellets. ^{19}F spectroscopic quantification was performed for all cell samples with 10 µl trifluoroacetic acid (TFA, 1% volume concentration) sealed in a pipette tip as an external standard. Multi-chromatic imaging of CE NP, PFOB NP and TFA standard was performed using the protocol described previously.

***In vivo* demonstration of multi-chromatic MRI**

A Swiss Webster mouse was anesthetized with ketamine/xylazine. The left leg of the mouse was secured to the inner surface of a custom-built ^{19}F/^{1}H dual frequency solenoid coil. 10 µl of CE NP were injected into the foot pad of the left leg while 50 µl of PFOB NP was injected intramuscularly into the calf. A ^{1}H gradient echo image was firstly acquired to visualize the anatomy of the leg, with TR = 100 ms, TE = 5 ms, thickness = 1 mm, resolution = 0.5 mm× 0.5 mm. Without retuning the dual-frequency probe, ^{19}F spectroscopy was acquired at the exact same position over the whole leg. A receiving bandwidth of 40 KHz was used to cover the widely spread chemical shifts of PFOB. By selectively exciting and receiving at the signature frequency of CE and PFOB as described in previous sections, multi-chromatic ^{19}F MRI was performed to map the distribution of both PFC NPs. The detailed imaging parameters were as follows: echo train length = 8, TR= 2 s, TE = 20 ms, in plane resolution = 1 mm × 1 mm, slice thickness = 2 mm.

3.3.3 Results

NMR spectra of PFOB, PFD, PF-12-CE, PF-15-CE and PFO are shown in Figure 3.9. Signature frequencies selected for ^{19}F MRI were marked and color coded to represent the different PFCs. The closest signature frequencies between two PFCs were from PF-15-CE and PF-12-CE, which were only 800 Hz apart. Because of the extremely narrow excitation bandwidth (700 Hz) used in this study, we were able to identify and image each of the PFC species individually. MRI images of all PFC components (Figure 3.10), normalized to the maximal intensity within the region of interest (ROI), were color coded with the same color as marked in the corresponding spectra. Because we always placed the excitation and readout central frequency at the signature frequency of the PFC that we aimed to image, chemical shift artifact was not present in the ^{19}F images and all ^{19}F images automatically co-registered well with the ^{1}H background image. Moreover, the J-coupling effect was not present in these images because both the multi-echo MRI paradigms and the selective excitation suppress the indirect coupling between multiple chemical groups within a PFC molecule.

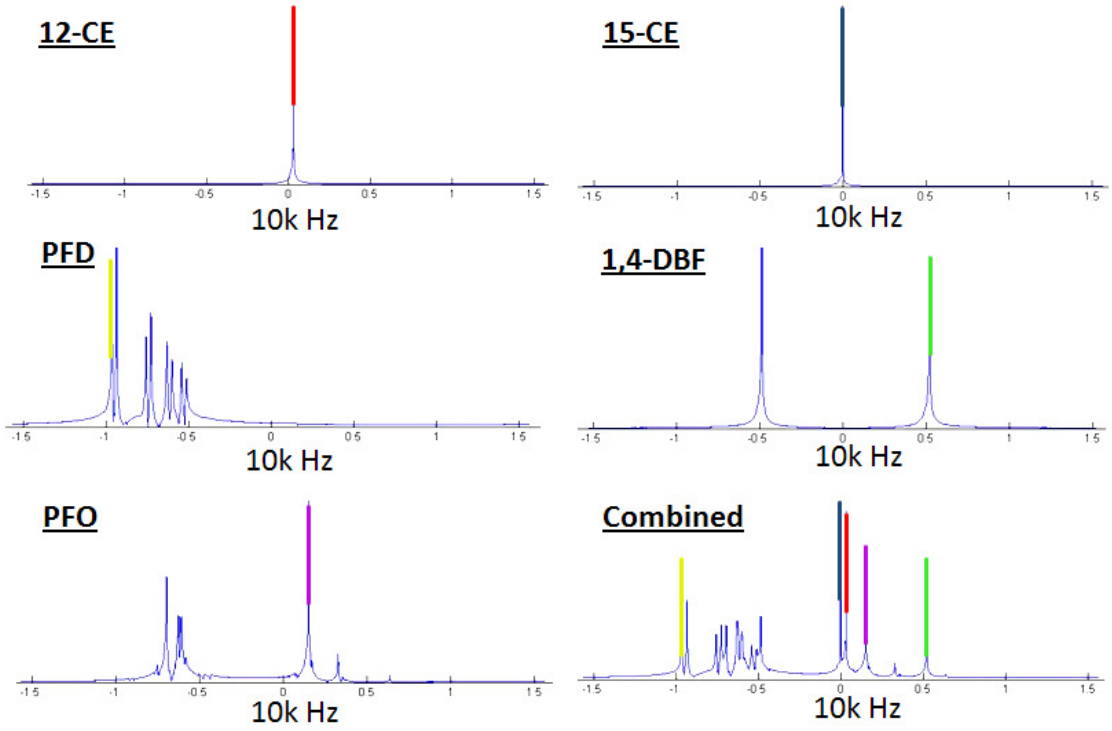

Figure 3.9 MR spectra of five PFC components. One signature frequency (color coded) of each PFC component was selected for multi-chromatic ^{19}F MRI

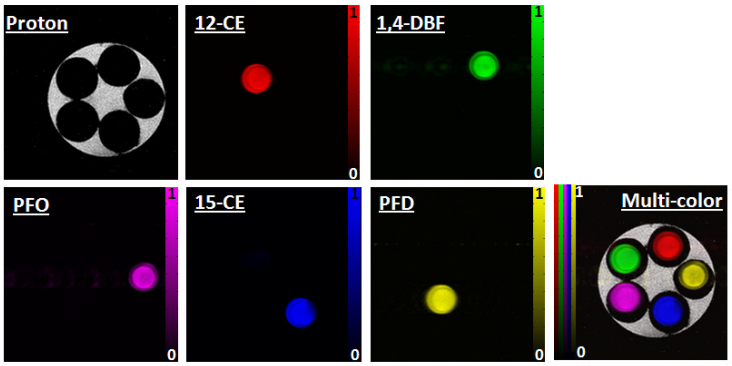

Figure 3.10 Multi-chromatic ^{19}F MRI of a phantom containing five PFC components.

***In vivo* result**

Two imaging slices from the mouse leg (Figure 3.11) revealed distinct localizations of CE NP and PFOB NP representing different injection schemes. Good separation between two

PFC NPs was achieved in the ^{19}F image, as a demonstration of the feasibility for multi-chromatic ^{19}F *in vivo*.

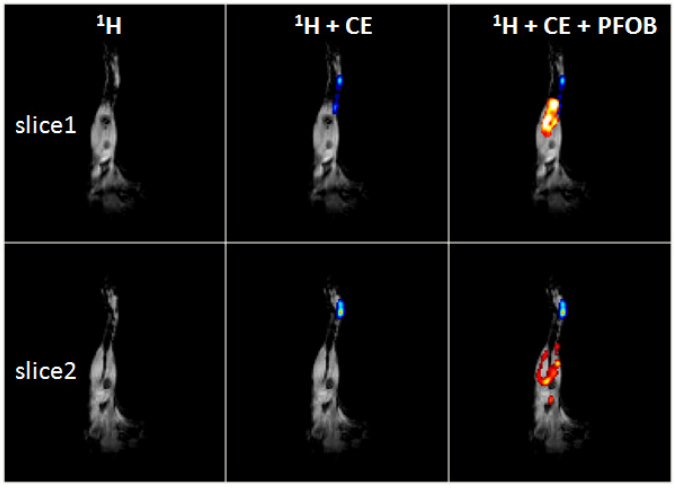

Figure 3.11 *In vivo* multi-chromatic ^{19}F MRI of mouse leg. (Blue: CE, Yellow: PFOB)

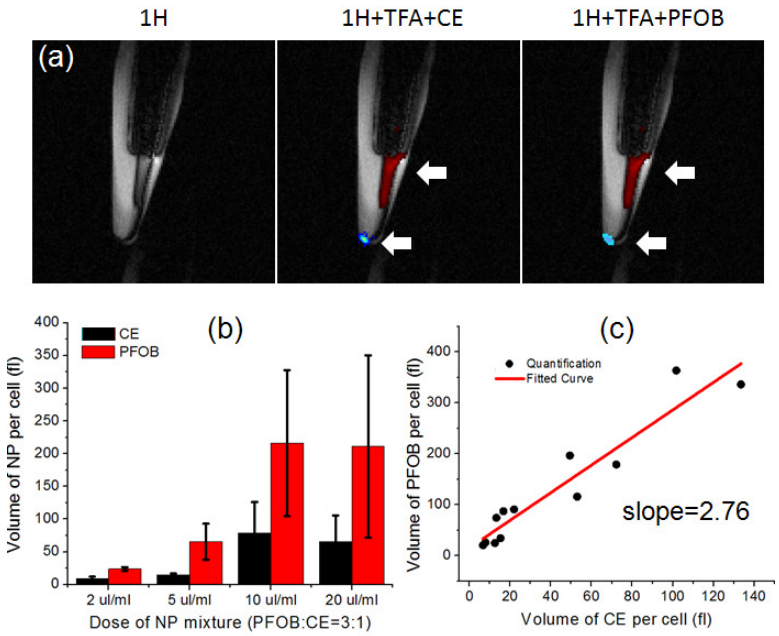

Figure 3.12 Multi-chromatic ^{19}F MRI for macrophage cellular imaging. (a) Multi-chromatic ^{19}F of macrophage pellet. (b) Quantification of both PFOB and CE NP at different incubation dose. (c) Internalized concentration of PFOB and CE NP are linearly correlated.

Cellular imaging result

Representative multi-chromatic images and spectroscopic quantification are shown in Figure 3.12a&b. The TFA standard and internalized CE and PFOB NP in cell pellet are visualized individually in ^{19}F MRI. The ^{19}F quantification revealed an increase of retained NP concentration in cells as the incubation concentration increased. However, there was no significant difference between the 10 µl/ml and 20µl/ml groups suggesting that macrophages were saturated at the high dose of PFC NP. As shown in Figure 3.12c, the retained concentration of CE NP was linearly correlated with PFOB NP and the ratio between them was identical to that in the NP mixture used for incubation (1:3). These results confirmed that macrophage cells endocytosed both NPs in the same manner if they possessed identical size and surface charge. The specific chemical contents inside PFC NP did not seem to affect the cellular update in macrophages.

3.3.4 Discussion

In this work, we have proposed and verified a paradigm for multi-chromatic ^{19}F MRI imaging. We validated this technique in a phantom containing five different PFC components, each one of which could be imaged via MRI individually. Using multi-chromatic ^{19}F MRI as a tool, we investigated the cellular update of two different PFC NPs in macrophages. We quantitatively defined the saturation level of macrophage endocytosis for PFC NP and confirmed that PFC component did not affect the internalization of these particles into cells. We also demonstrated our multi-chromatic ^{19}F MRI technique *in vivo* for visualizing two different intramuscularly injected PFC NPs.

Currently, multiple clinical and preclinical targeting mechanisms have been proved to be effective *in vivo* using functionalized PFC NP and associated imaging techniques. These PFC NPs with targeting ligands actively bind to various biomarkers in cancer and cardiovascular

disease, such as $\alpha_v\beta_3$ (14) and $\alpha_v\beta_5$ (15) in rabbit tumor and atherosclerotic angiogenesis (16), fibrin (17) and thrombin during acute coagulation (18), and VCAM during microvascular inflammation of chronic renal disease (8). Multi-chromatic ^{19}F MRI could provide a promising imaging approach for registering multiple disease biomarkers simultaneously and investigating the pathophysiological interaction between different disease epitopes.

3.4 References

1. Levitt MH. Spin dynamics : basics of nuclear magnetic resonance. Chichester, England ; Hoboken, NJ: John Wiley & Sons; 2008. xxv, 714 p., 717 p. of plates p.
2. Mason RP, Bansal N, Babcock EE, Nunnally RL, Antich PP. A novel editing technique for 19F MRI: molecule-specific imaging. Magn Reson Imaging 1990;8(6):729-736.
3. Babcock EE, Mason RP, Antich PP. Effect of homonuclear J modulation on 19F spin-echo images. Magn Reson Med 1991;17(1):179-188.
4. Sotak CH, Hees PS, Huang HN, Hung MH, Krespan CG, Raynolds S. A NEW PERFLUOROCARBON FOR USE IN F-19 MAGNETIC-RESONANCE-IMAGING AND SPECTROSCOPY. MagnResonMed 1993;29(2):188-195.
5. Stables LA, Kennan RP, Anderson AW, Gore JC. Density matrix simulations of the effects of J coupling in spin echo and fast spin echo imaging. J Magn Reson 1999;140(2):305-314.
6. Allerhand A. Analysis of Carr---Purcell Spin-Echo NMR Experiments on Multiple-Spin Systems. I. The Effect of Homonuclear Coupling. The Journal of Chemical Physics 1966;44(1):1-9.

7. Giraudeau C, Flament J, Marty B, Boumezbeur F, Meriaux S, Robic C, Port M, Tsapis N, Fattal E, Giacomini E, Lethimonnier F, Le Bihan D, Valette J. A new paradigm for high-sensitivity 19F magnetic resonance imaging of perfluorooctylbromide. Magn Reson Med 2010;63(4):1119-1124.

8. Southworth R, Kaneda M, Chen J, Zhang L, Zhang H, Yang X, Razavi R, Lanza G, Wickline SA. Renal vascular inflammation induced by Western diet in ApoE-null mice quantified by (19)F NMR of VCAM-1 targeted nanobeacons. Nanomedicine 2009;5(3):359-367.

9. Parhami P, Fung BM. Fluorine-19 relaxation study of perfluoro chemicals as oxygen carriers. The Journal of Physical Chemistry 1983;87(11):1928-1931.

10. Neubauer AM, Myerson J, Caruthers SD, Hockett FD, Winter PM, Chen J, Gaffney PJ, Robertson JD, Lanza GM, Wickline SA. Gadolinium-modulated 19F signals from perfluorocarbon nanoparticles as a new strategy for molecular imaging. Magn Reson Med 2008;60(5):1066-1072.

11. Yu JX, Kodibagkar VD, Cui W, Mason RP. 19F: a versatile reporter for non-invasive physiology and pharmacology using magnetic resonance. Curr Med Chem 2005;12(7):819-848.

12. Srinivas M, Cruz LJ, Bonetto F, Heerschap A, Figdor CG, de Vries IJ. Customizable, multi-functional fluorocarbon nanoparticles for quantitative in vivo imaging using 19F MRI and optical imaging. Biomaterials 2010;31(27):7070-7077.

13. Caruthers SD, Neubauer AM, Hockett FD, Lamerichs R, Winter PM, Scott MJ, Gaffney PJ, Wickline SA, Lanza GM. In vitro demonstration using 19F magnetic resonance to

augment molecular imaging with paramagnetic perfluorocarbon nanoparticles at 1.5 Tesla. Invest Radiol 2006;41(3):305-312.

14. Winter PM, Schmieder AH, Caruthers SD, Keene JL, Zhang H, Wickline SA, Lanza GM. Minute dosages of alpha(nu)beta3-targeted fumagillin nanoparticles impair Vx-2 tumor angiogenesis and development in rabbits. FASEB J 2008;22(8):2758-2767.

15. Schmieder AH, Caruthers SD, Zhang H, Williams TA, Robertson JD, Wickline SA, Lanza GM. Three-dimensional MR mapping of angiogenesis with alpha5beta1(alpha nu beta3)-targeted theranostic nanoparticles in the MDA-MB-435 xenograft mouse model. FASEB J 2008;22(12):4179-4189.

16. Winter PM, Morawski AM, Caruthers SD, Fuhrhop RW, Zhang H, Williams TA, Allen JS, Lacy EK, Robertson JD, Lanza GM, Wickline SA. Molecular imaging of angiogenesis in early-stage atherosclerosis with alpha(v)beta3-integrin-targeted nanoparticles. Circulation 2003;108(18):2270-2274.

17. Morawski AM, Winter PM, Yu X, Fuhrhop RW, Scott MJ, Hockett F, Robertson JD, Gaffney PJ, Lanza GM, Wickline SA. Quantitative "magnetic resonance immunohistochemistry" with ligand-targeted (19)F nanoparticles. Magn Reson Med 2004;52(6):1255-1262.

18. Myerson J, He L, Lanza G, Tollefsen D, Wickline S. Thrombin-inhibiting perfluorocarbon nanoparticles provide a novel strategy for the treatment and magnetic resonance imaging of acute thrombosis. J Thromb Haemost 2011;9(7):1292-1300.

4 Paramagnetic relaxation enhancement of PFC NP

4.1 Introduction

Molecular imaging with ligand-targeted ^{19}F nanoparticles (NP) is an emerging diagnostic approach for magnetic resonance imaging (MRI) and spectroscopic detection and classification of various diseases (1). When combined with conventional ^{1}H MRI, ^{19}F MRI yields high resolution anatomic information and enables spectroscopic quantification of disease biomarkers (2-4). Among the available ^{19}F MR contrast agents, perfluorocarbon (PFC) NPs have shown potential for imaging of cancer and atherosclerosis both as vehicles of paramagnetic agents (5-7) and as intrinsic fluorine signaling entities (8-11). The high concentration of ^{19}F in PFC NP, the lack of innate background ^{19}F signal in tissues, and the demonstrated safety of the basic agent (12), position targeted PFC NP as a promising contrast agent for molecular MRI with significant translational potential (4).

However, the ^{19}F MR signal intensity of PFC NP is limited by two factors that impose hurdles for clinical utilization. First, despite its high signal nucleus, the total amount of ^{19}F that can be injected still is much less than the natural abundance of ^{1}H in tissues (13), which challenges signal-to-noise requirements in clinical imaging scenarios. Second, the long ^{19}F T_1 for PFC NP, which is roughly equivalent to that of neat PFC liquid, challenges efficient data acquisition (14). Lee et al originally reported that Gd can function as a relaxation agent for fluorine under certain circumstances (15). Recently, Neubauer et al showed that coating PFC NP with paramagnetic Gd chelates markedly accelerates relaxation of PFC molecules and thus is indeed useful for enhancing the ^{19}F signal within the limited timeframe typically available for *in vivo* imaging (16). Nevertheless, in order to better facilitate its further application *in vivo* and

provide guidance for the chemical synthesis of this type of paramagnetic NP, a first-principle analysis of the special relaxation properties of ^{19}F spins in paramagnetic PFC NP is of great importance.

Previous investigations of water translational motion used models of pure outer-sphere relaxation to study spin dynamics of ^{1}H that are separated from free radicals by lipid bilayer membranes, silicon surfaces, or protein surfaces (17-19). In this report, we suggest similar applications to the specific case of assessing the paramagnetic relaxation enhancement of ^{19}F nuclei in the core of PFC NP. To do so, the Solomon, Bloembergen and Morgan theory (SBM theory) (20-22) was applied to the outer-sphere interaction between ^{19}F spins and Gd ions that are separated by lipid monolayer. The modeling framework for the paramagnetic relaxation enhancement recognizes that at clinical field strengths the zero field split effect can be neglected (23).

For aqueous solutions, the total paramagnetic relaxation enhancement is contributed by two compartments: inner-sphere and outer-sphere relaxation (24). The inner-sphere relaxation requires a direct coupling interaction between the imaging/signaling molecule (e.g., water for ^{1}H MRI, or PFC for ^{19}F MRI) and a paramagnetic ion (e.g., Gd^{3+}) over a short time interval to facilitate energy transfer. In contrast, outer-sphere relaxation is caused by the translational diffusion of the imaging molecule around the paramagnetic center without the need of direct binding (25-27). For most paramagnetic contrast agents, the inner-sphere relaxation (i.e., the direct binding effect) is the dominant mechanism for relaxation enhancement. However, inner-sphere relaxation does not exist in PFC NP because the PFC core is well separated from surface Gd ions by a lipid/surfactant monolayer (Fig. 4.1a). The relaxation enhancement in this case is

caused solely by the diffusion of encapsulated PFC molecules to the proximity of Gd on the outer lipid monolayer surface through an outer-sphere relaxation mechanism.

Based on this physical model, we sought to apply these observations to elucidate the interaction of a living cell with such a NP system after internalization into endosomal compartments, and to detect the actual break down of the particle into its component parts (28). We show that endocytosis results in an alteration in ^{19}F relaxation as Gd chelates are stripped from the NP surface, thus returning the ^{19}F T_1 to its native relaxation state without paramagnetic relaxation enhancement. These interactions reveal a "^{19}F relaxation switch" phenomenon that can track the activity of the endosome as it degrades the ingested material, which might be of use experimentally for dynamic monitoring of the function of such intracellular organelles.

4.2 Theory

4.2.1 Boundary conditions and physical parameters of PFC NP with Gd coating

The structure of paramagnetic PFC NP is illustrated in Figure. 4.1a. The NPs are the PFC droplets in a PFC-water emulsion system and exhibit diameters ranging 100-300 nm. Because the hydrophilic head groups of the lipid monolayer establish an ultimate boundary against the translational diffusion of PFC molecules toward the Gd on the outer surface, we follow the treatment in (29) to introduce the concept "distance *d* of closest approach", where *d* is defined as the smallest distance between a PFC molecule in the core of the NP and the Gd ion layer on the surface of NP. Practically, *d* is a parameter determined by the length of the linker attaching the Gd chelate to the hydrophilic surface of the lipid layer, as well as by the maximal penetration depth of PFC molecule into the hydrophobic tails of the lipid layer (5, 19). To simplify the modeling, the diffusion of the PFC molecule is assumed to be unrestricted with a diffusion

coefficient *D* as long as its distance to the Gd layer is greater than *d*. Finally, the Gd chelates on the lipid layer are assumed to be randomly distributed and the Gd concentration is described by a Gd/lipid molar ratio *[Gd]*. These physical properties of NP influence the enhancement of longitudinal relaxation rate ΔR_1 of PFC NP (30), which is defined as the difference between R_1 ($R_1=1/T_1$) of Gd-coated NP and non-Gd-coated NP,

$$\Delta R_1 = R_1(NP\,with\,Gd) - R_1(NP\,without\,Gd). \qquad [1]$$

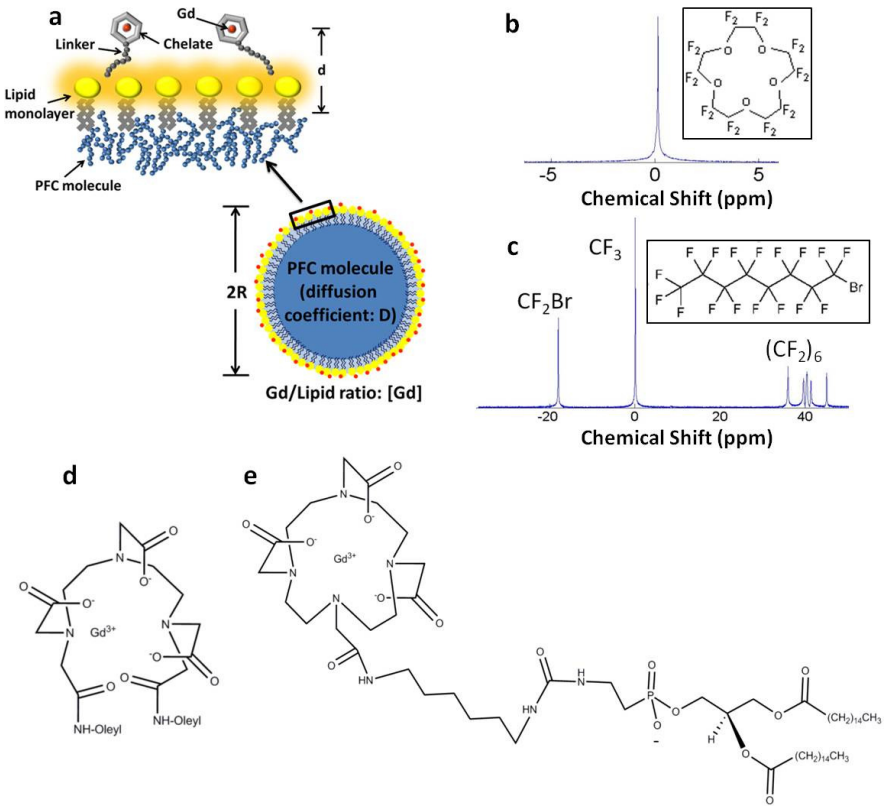

Figure 4.1 Chemical structure of paramagnetic PFC NP. (a) Illustration of configuration of paramagnetic PFC NP. Direct contact between Gd ions and PFC molecules is prevented by the lipid monolayer. (b) and (c), Chemical structure and NMR spectra of CE and PFOB. (d) and (e), Chemical structure of DTPA-BOA-Gd and DOTA-PE-Gd shows the longer linker chain of DOTA-PE-Gd as compared with DTPA-BOA-Gd.

4.2.2 Theoretical calculation of paramagnetic relaxation enhancement in PFC NP

Paramagnetic relaxation enhancement of PFC NP is caused by the fluctuation of dipolar energy between the electron spin $\vec{S}$ from the Gd ion and the nuclear spin $\vec{I}$ from the PFC molecule (21). Specifically, this dipolar interaction Hamiltonian takes the following form

$$H_{IS} = \frac{\hbar^2 \gamma_I \gamma_S}{r_{IS}^{\ 3}}[3(\vec{I} \bullet \vec{r})(\vec{S} \bullet \vec{r}) - \vec{I} \bullet \vec{S}] = F_0 A_0 [I_Z S_Z - \frac{1}{4}(I_+ S_- + I_- S_+)] + F_1 A_1 (I_+ S_Z + I_Z S_+) + F_1^* A_1 (I_- S_Z + I_Z S_-) + F_2 A_2 I_+ S_+ + F_2^* A_2 I_- S_-], \quad [2]$$

in which $F_0 = (1 - 3\cos^2\theta) / r_{IS}^{\ 3}$, $F_1 = \sin\theta\cos\theta e^{i\varphi} / r_{IS}^{\ 3}$, and $F_2 = \sin^2\theta e^{2i\varphi} / r_{IS}^{\ 3}$ represent three components of the dipolar interaction that are proportional to the second rank spherical harmonics; γ_I and γ_S are the gyromagnetic ratios for relevant nuclear and electron spin; and $A_0 = \hbar^2 \gamma_I \gamma_S$, $A_1 = -3/2\hbar^2 \gamma_I \gamma_S$ and $A_2 = -3/4\hbar^2 \gamma_I \gamma_S$ are three real constants. Based on the theoretical treatment proposed by Solomon (21), the relaxation enhancement of $\vec{I}$ contributed by a single nuclear-electron spin pair can be written as

$$\Delta r_1 = \hbar^2 \gamma_I^{\ 2} \gamma_S^{\ 2} S(S+1)[\frac{1}{12} J_{0,pair}(\omega_I - \omega_S) + \frac{3}{2} J_{1,pair}(\omega_I) + \frac{3}{4} J_{2,pair}(\omega_I + \omega_S)], \quad [3]$$

in which $J_{q,pair}(q = 0,1,2)$ is the spectral density of the correlation function for the q^{th} component of dipolar interaction F_q; S is the quantum number for the total electron spin; ω_I and ω_S are the Larmor precession angular frequencies for nuclear and electron spin, respectively. Specifically, the spectral density for correlation function of the q^{th} component of the dipolar interaction is defined as (29)

$$J_{q,pair}(\omega) = \int_{-\infty}^{\infty} \overline{F_q(t) F_q^{\ *}(t+\tau)} e^{-i\omega\tau} d\tau = \mathrm{F}[\overline{F_q(t) F_q^{\ *}(t+\tau)}], \quad [4]$$

in which F represents Fourier transform, and the average is taken over t with the τ and ω forming a Fourier transform pair.

The magnitude of a specific component of dipolar interaction F_q is modulated by two factors: 1) for a PFC molecule, the diffusion-induced change of the relative distance and angle θ, φ between a nuclear-electron spin pair (31); and 2) the propensity of the anchored Gd chelate on the lipid surface to undergo vibration, reorientation of the linker chain, and lateral diffusion across the membrane that might modulate nuclear-electron interactions (32). In the present study, the second mechanism is negligible because the lateral diffusion of Gd chelate on the lipid surface is restricted and much slower than is the Brownian diffusion of PFC inside the NP (32). Thus, we assume that the diffusion of PFC molecules represents the major source for the fluctuation of dipolar interactions. The probability for a single PFC molecule to move from position $\overrightarrow{R_0}$ to $\vec{R}$ after time τ was modeled as a Gaussian function (33)

$$P(\tau,\vec{R};\overrightarrow{R_0}) = (4\pi D\tau)^{-3/2} e^{-\frac{(\vec{R}-\overrightarrow{R_0})^2}{4D\tau}}, \qquad [5]$$

where D is the diffusion coefficient of PFC molecule.

The coordinate system used in Eq. 2 to define F_q is centered at the electron spin. The z-axis is along the direction of the external magnetic field. To facilitate modeling in a symmetric way, an alternative coordinate system, the "NP reference frame", was defined with the origin positioned at the center of the NP and the z-axis aligned in the direction of external field. The expression of F_q in the NP reference frame then depends on the position of the electron spin. Taking into account all possible positions of a nuclear spin interacting with a single electron spin at position $(\theta_{Gd},\varphi_{Gd})$ on the surface of NP, the spectral density can be rewritten in the following form

$$J_q(\theta_{Gd},\varphi_{Gd},\omega)=\mathrm{F}[\iint P(\tau,\vec{R};\vec{R}_0)F_q(\theta_{Gd},\varphi_{Gd},\vec{R}_0)F_q^{*}(\theta_{Gd},\varphi_{Gd},\vec{R})d\vec{R}d\vec{R}_0]/\frac{4}{3}\pi r^3, \quad [6]$$

where the integral is taken over the space inside the NP. Considering the spherical symmetry of the NP and summing up the contribution from all the Gd ions and following the calculation proposed by Abragam (29), the spectral densities including all the electron spins are in the form of

$$J_{q,total}(\omega)=\sum_{Gd\ Positions} J_q(\theta_{Gd},\varphi_{Gd},\omega)=C_q\frac{[Gd]}{r}\int_0^{\infty}\frac{Dk^3}{\omega^2+(Dk^2)^2}[\int_d^{\infty}\frac{J_{5/2}(kx)}{x^{3/2}}(1-\frac{d}{x})dx]^2dk, \quad [7]$$

in which $J_{5/2}(kx)$ is the Bessel function and C_q's are real constants with the relationship $C_0:C_1:C_2=6:1:4$ due to normalization factors for F_q's (21). The absolute value of C_q's is determined by the separation of surface Gd ions (16). Because the gyromagnetic ratio of the electron spin is more than 1000x greater than that of the nuclear spin, both $\omega_I-\omega_S$ and $\omega_I+\omega_S$ would be much greater than ω_I. Careful examination reveals that $J_{0,total}(\omega_I-\omega_S)$ and $J_{2,total}(\omega_I+\omega_S)$ are negligible compared to $J_{1,total}(\omega_I)$, so that the final form for the relaxation enhancement for the NP is:

$$\Delta R_1=\frac{3}{2}\hbar^2\gamma_I{}^2\gamma_S{}^2S(S+1)C_1\frac{[Gd]}{r}\int_0^{\infty}\frac{Dk^3}{\omega_I{}^2+(Dk^2)^2}[\int_d^{\infty}\frac{J_{5/2}(kx)}{x^{3/2}}(1-\frac{d}{x})dx]^2dk. \quad [8]$$

Thus, enhanced relaxation is due primarily to the dipolar interaction terms $I_{\pm}S_Z$ and $I_ZS_{\pm}$ corresponding to $q=1$ in Eq. 2.

4.3 Material and Methods

4.3.1 NP formulation and characterization

The actual PFC NP emulsion is composed of 20% (v/v) of perfluoro-15-crown-5 ether (CE; Exfluor Research Corp., USA) or perfluorooctylbromide (PFOB; Minnesota Manufacturing and Mining, USA), a 2.0% (w/v) surfactant commixture, and 1.7% (w/v) glycerin, with water comprising the balance. CE has twenty chemically equivalent fluorine atoms and produces a single ^{19}F NMR peak (Figure 4.1b); PFOB exhibits seven different chemical shifts and J-coupling splitting (Figure 4.1c). For incorporating the paramagnetic ions, the surfactant commixture is comprised of lecithin (Avanti Polar Lipids Inc, USA), dipalmitoyl-phosphatidylethanolamine (Avanti Polar Lipids Inc., USA) and two possible lipophilic gadolinium chelates, namely Gd-DTPA-BOA (Gateway Chemical Technologies, USA) and Gd-DOTA-PE (Dow Chemical Co., USA) with the concentration of 30 mol% Gd. The relevant difference between the two Gd chelates is that Gd-DTPA-BOA has shorter linker arm length than does Gd-DOTA-PE, which causes the DTPA-BOA linked Gd to abut the surface of the NP (34) (Figure 4.1d and e), whereas the DOTA-PE linked Gd is more remote. The particle sizes were determined at room temperature with a dynamic light scattering particle sizer (Brookhaven Instruments Corp., USA). Diffusion coefficients of the neat liquid CE and PFOB were measured at room temperature with a pulsed gradient spin echo sequence on a 4.7 T Varian INOVA small-bore imaging system (35).

4.3.2 Monte-Carlo simulation

To confirm the non-uniform field distribution in the PFC core, a Monte-Carlo simulation of the Gd-induced magnetic field inside the PFC NP was performed. We chose 1,800 randomly sampled points on the surface of NP (diameter, 200 nm) as the locations for Gd ions, and set the

distance between Gd to the surface of NP at 2 nm. For each point inside the NP, the contributions from all dipolar magnetic fields produced by Gd ions were summed. In the simulation, the magnitude of magnetizations of Gd ions was set to be constant and their directions set along the external magnetic field, i.e., the z-direction (because of the short relaxation of electron spin, the magnetic moment of a single spin was treated as in a thermal equilibrium state).

4.3.3 T_1 measurement and experimental data fitting

T_1 of NP samples was measured with an inversion recovery sequence on a 3 T Philips imaging system, a 4.7 T Varian imaging system, a 7 T Varian NMR spectrometer, and an 11.7 T Varian imaging system. For PFOB, the T_1 was measured on the CF_3 peak in its NMR spectrum (36-38). According to Eq. 8, the undetermined constant C_1 notwithstanding, four definite parameters contribute to the relaxation enhancement ΔR_1: 1) diffusion coefficient D, 2) Larmor frequency ω_I, 3) particle size r, and 4) distance of closest approach d. The only parameter that cannot be measured directly is the distance of closest approach d. Therefore, based on the NP structural parameters and the measured relaxation enhancement, we opted to fit the experimental data to Eq. 8 and test if it gave a reasonable estimate for d. The nonlinear fitting of the experimental data to the theoretical prediction was executed in Mathematica (Wolfram Inc, USA) based on the least squares principle.

4.3.4 In vitro demonstration of "^{19}F relaxation switch" after cell internalization

$\alpha_v\beta_3$-integrin expressing RAW 267.7 murine macrophages (passage 4 or 5) were used for all experiments to elicit active endocytosis of PFC NP. Incubations were carried out in gelatin-coated T75 cell culture flasks with $\alpha_v\beta_3$-integrin targeted CE NP anchored with Gd-DTPA-BOA (2 μl/ml). After being incubated for 2, 24 or 48 hour, cells were washed with PBS three times

and then centrifuged to obtain pellets. ^{19}F spectroscopic quantification was performed at an 11.7 T Varian small animal imaging scanner using previously reported methods (39). The ^{1}H and ^{19}F longitudinal relaxation properties of the cells were measured on a 4.7 T Varian small animal imaging scanner with an inversion recovery sequence. To confirm that other factors (e.g. intracellular oxygen gradient) did not contribute to the change of ^{19}F T_1 after internalization, the ^{19}F T_1 of internalized plain CE NP , i.e., without Gd chelates, was also measured.

For fluorescent microscopy of internalized PFC NP, another group of cells were incubated with $\alpha_v\beta_3$-integrin targeted PFC NP colabeled with Alexa Fluor 594. Subsequently, cells were fixed with 4% paraformaldehyde for 30 mins, mounted with DAPI media [VECTASHIELD Inc., USA], and imaged with Olympus BX61 fluorescent microscope.

4.4 Results

4.4.1 Inhomogeneous magnetic field in NP

As shown in Figure 4.2, the magnetic field fluctuates considerably near the surface of NP but is relatively homogeneous in the central part of NP. In addition, since the direction of external field is the z-direction, the Gd-induced magnetic field is not isotropic and exhibits slightly different distributions on the xy and xz-plane.

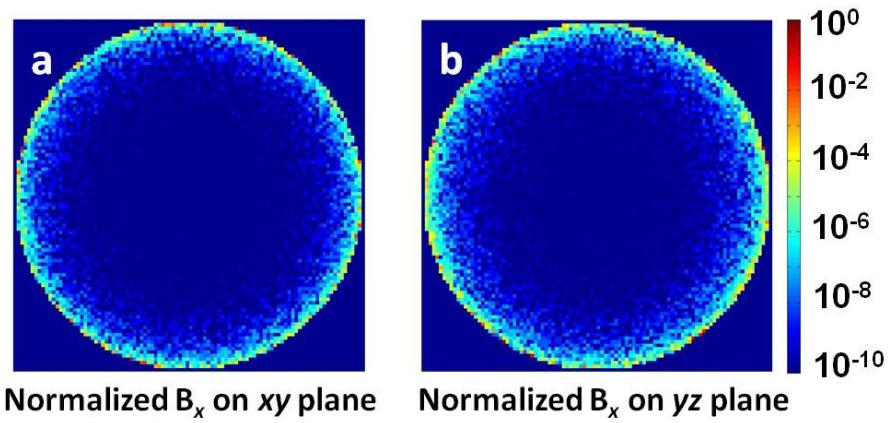

Figure 4.2 Monte-Carlo simulation of Gd-induced magnetic field inside NP. X-component of the field strength on the xy-plane and xz-plane of the NP are depicted in (a) and (b), respectively. Inhomogeneous field distribution is visually appreciable close to the surface of the PFC NP.

4.4.2 Effect of the structural parameters on ^{19}F ΔR_1

Figure 4.3a illustrates the dependence of ^{19}F ΔR_1 on the radius of the NP according to Eq. 8. Because the paramagnetic ions are located only on the surface of the PFC NP instead of mixing in the PFC core, the surface to volume ratio of the PFC NP results in the $1/r$ dependence of ΔR_1. This result agrees with the classical paramagnetic relaxation enhancement phenomenon for an aqueous solution, in which ΔR_1 is proportional to the volume concentration of paramagnetic ions (14). Figure 4.3b plots ΔR_1 as a function of the distance of closest approach d. Selected combinations of diffusion coefficient D and external magnetic field B were examined. In comparison to the $1/d^6$ dependence for pure inner-sphere relaxation scenarios, e. g. immersion depth measurements (40) and protein structure determinations (41), it is evident in Figure 4.3b that the decay of ΔR_1 for paramagnetic NP relative to d is slower, in agreement with previous results found by Polnaszek et al (18). Figure 4.3c depicts the relation between ^{19}F ΔR_1

and the external field strength B_0. Selected combinations of distance of closest approach d and diffusion coefficient D are shown in different line styles. The longitudinal relaxation enhancement of NP decreases monotonically when the external magnetic field increases over the range of the field strengths plotted. Figure 4.3d illustrates the dependence of ΔR_1 on the diffusion coefficient D of the PFC molecule. The effect of D is complex and non-monotonic: the maximal relaxation enhancement occurs for certain optimal combinations of d, D and Larmor frequency ω_I. The potential underlying mechanism for this non-monotonic behavior is considered in detail in the Discussion.

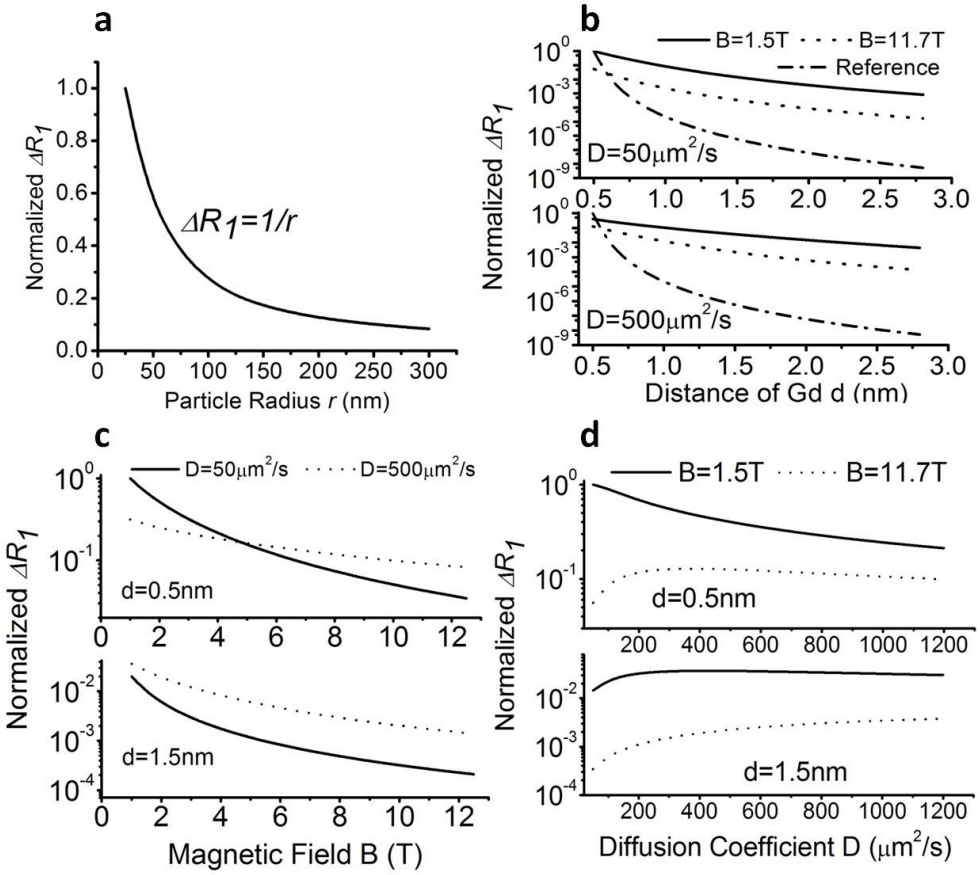

Figure 4.3 Theoretical predication of relaxation enhancement as a function of particle configuration. (a) Normalized relaxation enhancement ΔR_1 as a function of particle radius. The

value of ΔR_1 is normalized to that when r=25 nm. ΔR_1 is inversely proportional to the radius of NP. (b) ΔR_1 as a function of closest distant of approach. The radius of NP r is fixed to be 100 nm. The value of ΔR_1 when D=50 $\mu m^2/s$, d=0.5 nm and B=1.5 T is normalized to one. The curve $1/d^6$ was plotted as the reference. (c) ΔR_1 as a function of external magnetic field. r was set to be 100 nm. The value of ΔR_1 when D=50 $\mu m^2/s$, d=0.5 nm and B=1.5 T is normalized to one. (d) ΔR_1 as a function of diffusion coefficient of PFC. The radius of NP r is fixed to be 100 nm. The value of ΔR_1 is normalized to the maximum value in the graph.

4.4.3 Experimental validation

Diffusion coefficients of neat CE and PFOB measured at room temperature were 210 $\mu m^2/s$ and 200 $\mu m^2/s$, respectively. The mean diameters of three types of paramagnetic NP were: 382 nm (polydispersity, 0.177) for PFOB NP with Gd-DOTA-PE, 270 nm (polydispersity, 0.082) for PFOB NP with Gd-DTPA-BOA, and 150 nm (polydispersity, 0.081) for CE NP with Gd-DTPA-BOA. Figure 4.4a illustrates the longitudinal relaxation rates of CE NP, CE NP with Gd-DTPA-BOA, PFOB NP, PFOB NP with Gd-DTPA-BOA, and PFOB NP with Gd-DOTA-PE at different magnetic fields. For comparison with the theoretical prediction (see Figure 4.4b), we used the relaxation enhancement of CE NP loaded with Gd-DTPA-BOA at 3 T as the reference to eliminate the effect of the constant C_1. The ratio between ΔR_1 of CE NP with DTPA-BOA-Gd and that of all NP at various fields were fitted to Eq. 8. The fitting variable, the distance of closest approach *d*, was the only parameter that varied among NPs due to the different chelate linker lengths and penetration depths. The fitting results for the distances of closest approach are: CE NP with Gd-DTPA-BOA, d = 0.9 nm; PFOB NP with Gd-DTPA-BOA, d =1.0 nm; and

PFOB NP with Gd-DOTA-PE, d = 1.4 nm. Note that according to the chemical structure, the length of all these linker chain is on the order of 1 nm, and that the Gd-DTPA-BOA has a shorter linker than does Gd-DOTA-PE (34). Therefore, the experiment illustrates that the theoretic prediction is qualitatively accurate. Additionally, the fitting result for d also provides a realistic experimentally measured range for the distance between the diffusing ^{19}F spins and the anchored Gd ions.

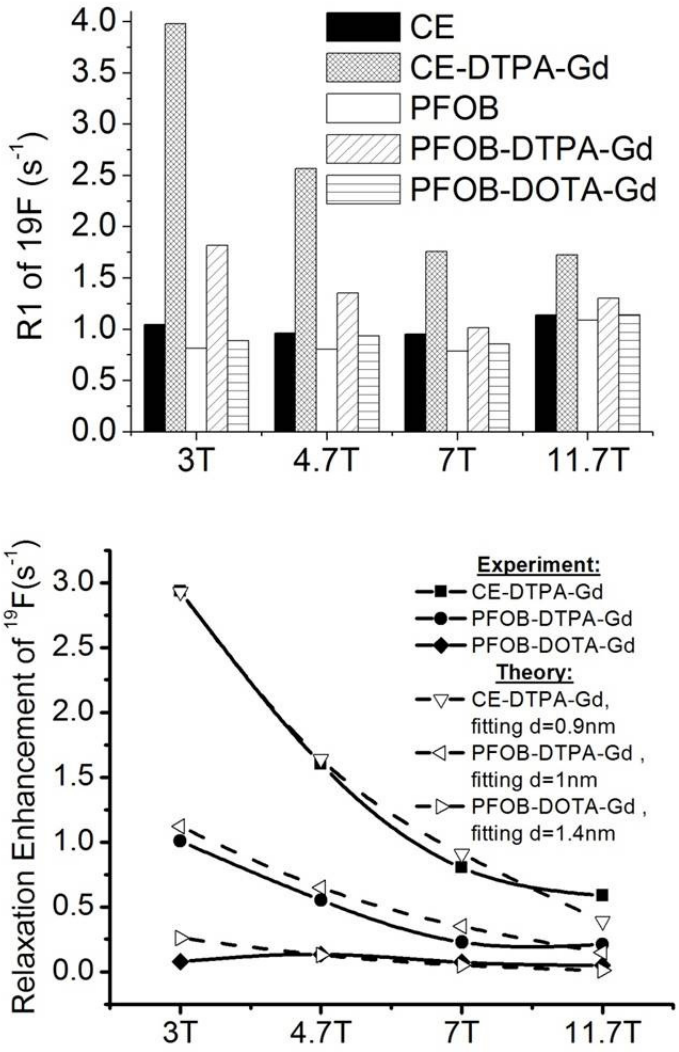

Figure 4.4 Theoretically predicted and experimentally measured relaxation of paramagnetic PFC NP. (a) Experimentally measured R_1 at various magnetic field strengths. (b) Relaxation enhancement ΔR_1 was extracted from the experimental data and compared with the theoretical fitting. Fitting result gives reasonable estimate of closest distant of approach d for PFC NP with DTPA-BOA-Gd and DOTA-PE-Gd.

4.4.4 Biological application for tracking endosome function

Fluorescent microscopy confirmed the intracellular localization of Alexa Fluor 594 in treated macrophages, suggesting internalization of PFC NP (Figure 4.5). Quantitative ^{19}F MR spectroscopy (Figure 4.6a) showed that the number of PFC NP per macrophage increased progressively within the first 48 hours following treatment with Gd-DTPA-BOA coated PFC NP. The delivery of Gd chelates on PFC NP to macrophage cells was confirmed by the progressively decreasing ^{1}H T_1 (or alternatively, increasing relaxation rate, $1/T_1$) (Figure 4.6b), reflecting the local paramagnetic effect of Gd. However, after endocytosis, the ^{19}F T_1 of PFC NP rapidly recovered to the baseline value of plain PFC NP (i.e., without Gd coating) within 2 hours (Figure 4.6c). The ^{19}F T_1 of internalized PFC NP remained at that level despite the continuous cellular uptake of PFC NP. Based on the theoretical prediction of Eq. 8, the shortened ^{1}H T_1 but fully recovered ^{19}F T_1 suggested that Gd chelates were rapidly separated from PFC NP upon endocytic ingestion.

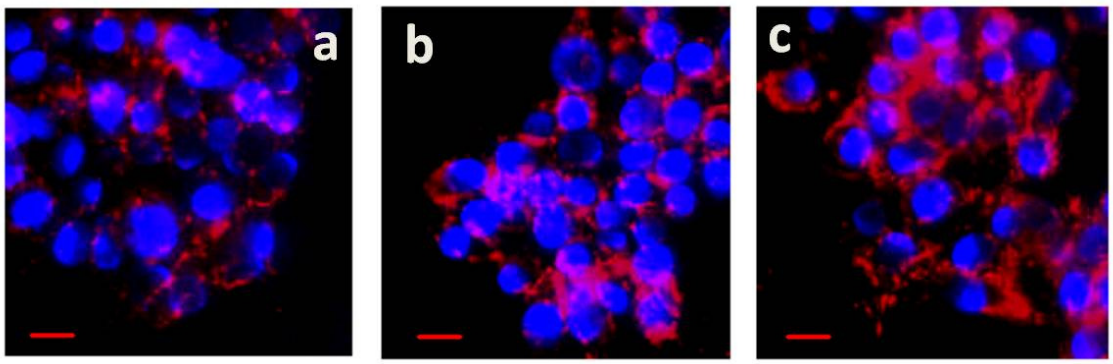

Figure 4.5 Fluorescent microscopy of PFC-NP treated macrophages with incubation time (a) 2 hours, (b) 24 hours, and (c) 48 hours. Blue=DAPI, red= Alexa Fluor 594, red scale bar = 10 μm.

4.5 Discussion

Targeted paramagnetic PFC NPs represent a promising construct for quantitative molecular imaging with magnetic resonance methods (4). In order to optimize such contrast agents for use in biological environments that can present multiple variables that might influence ^{19}F relaxivity such as oxygen tension, pH, temperature, blood flow, and imaging field strength, it is critical to understand ^{19}F relaxation phenomena from first principles. This requirement is also applicable to the relationship between relaxation properties and the physical composition of the NP itself which can vary in size, shape, and lipid and PFC composition.

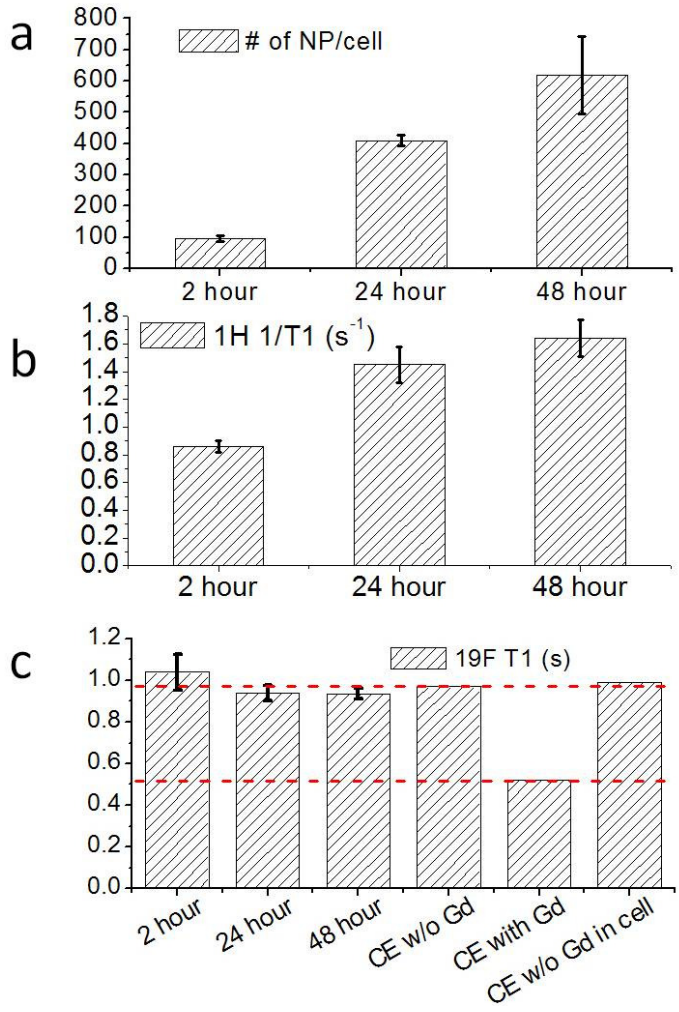

Figure 4.6 Quantitative ^{19}F spectroscopy of internalized paramagnetic PFC NP. Number of paramagnetic PFC NP per cells (a), proton longitudinal relaxation time (b), and fluorine longitudinal relaxation time (c) after 2, 24, 48 hour incubation. Data represent mean ± SD (n=4).

In this work, we have developed a theoretical framework for understanding these interactions and demonstrated the first order concordance between theory and measurement. Several novel conclusions can be stated. Firstly, paramagnetic relaxation enhancement of ^{19}F nuclei is observed in PFC NP because of the discrete distribution of Gd ions on the microscopic scale that gives rise to an inhomogeneous magnetic field when closely opposed to the particle surface. Secondly, the existence of a lipid monolayer barrier prevents the direct binding between

Gd ions and PFC molecules resulting in a pure outer-sphere relaxation mechanism that is the basis for the concordant predicted and observed relaxation behavior. Lastly, when Gd chelates are stripped from the nanoparticle surface after cell internalization, a "^{19}F relaxation switch" occurs, revealing the transition from intact bound particle to processed constituents, which is indicative of the intracellular endosomal material processing function.

According to SBM theory (29), paramagnetic relaxation enhancement of a PFC molecule with nuclear spin $\vec{I}$ inside the NP is attributed to the time-dependent dipolar interactions between the ^{19}F nuclear spin and the superposition of the magnetic fields produced by all electron spins $\vec{S}$ from the Gd ions (21). Interestingly, considering classical electromagnetism, a sphere with an ideally polarized magnetic shield should manifest a homogeneous internal magnetic field distribution (42) wherein the dipolar interactions remains constant as PFC molecules diffuse. However, because of the limited thickness of the lipid monolayer (around 1.5 nm), the distribution of Gd ions on the surface of PFC NP should be treated as discrete once the point of interest is close enough to the surface (i.e., on the same order of the distance between two neighboring Gd ions on the NP surface, which is around 1.4 nm for a NP with a diameter of 170 nm (16)).

It is notable that the distance of closest approach fitted from the experimental data is smaller than 1.5 nm, which approximates the length of the hydrophobic tail of the lipid molecule (16). The PFC molecules are known to penetrate the membrane lipid layer through diffusion and act to reduce membrane tension, which explains their ability to come into sufficiently close proximity to the Gd atoms on the NP surface to experience relaxation enhancement (37-38,43). Despite departing from the traditional $1/d^6$ dependence (Figure 4.3b) for outer sphere interactions, the paramagnetic relaxation enhancement effect still decreases dramatically with

increasing d , demonstrating that a Gd coating situated close to the surface of the PFC NP favorably enhances the relaxation of NP. These data are consistent with previous works from our group that have shown that when a relatively larger d has been achieved by simply mixing of the PFC NP emulsion and standard soluble Gd chelates that are not bound to the NP, the freely diffusible Gd ions around the NP exert no effect on the relaxation property of PFC NP (16). These results suggest that chelates with short linker chains would be preferred to form the paramagnetic coating.

With respect to the outer-sphere relaxation mechanism, two time scales are involved in the relaxation process for PFC nuclear spins: the time scale of diffusive motion d^2 / D, and the period of the Larmor precession $1/\omega_I$ (44). From the expression of ΔR_1 (Eq. 8), a close match between these two time scales is needed to achieve the optimal relaxation enhancement (Figure 4.3d). However, recognizing that it could be difficult to change the diffusion coefficient of the PFC molecules (constant at a given temperature), an appropriate choice of external field strength for imaging would be important to achieve the desired relaxation enhancement effect. Thus, a relatively low magnetic field strength would be favored for ^{19}F imaging with paramagnetic PFC NP, not only because the longitude relaxation is greater under low field conditions, but also because at high field the T_2^* of the PFC molecule tends to shorten significantly (16).

Together, these observations suggested an approach to tracking the function of intracellular organelles such as endosomes, based on their expected roles as processors of ingested materials. Upon endocytosis of the PFC NP by professional scavengers such as macrophage cells, the paramagnetic PFC NP structures are rapidly unpacked into PFC components and separate Gd chelates. This result also explains similar previous experimental observations in human umbilical vein derived endothelial cells (45). Because the ^{19}F longitudinal

relaxation is highly sensitive to the "distance of closest approach", in the present study we only observed two states for the paramagnetic PFC NP under the time constraints of the data sampling: the fully intact form and fully unpacked form. However, in the future, it would be of great interest to experimentally observe the dynamic change of ^{19}F T_1 during the process of endocytosis and then excretion, as a potential novel method for in vitro and even *in vivo* assessment of NP uptake and cellular function.

There are several limitations to the proposed model and calculations that are worth mentioning. First, the derivation was based on the theoretic treatment proposed by Solomon, in which the zero field split energy has been neglected. Thus, our expression for ΔR_1 does not hold at low magnetic field when the spin orbit coupling is of the same order at the Zeeman energy. Second, we have not considered the radial distribution of PFC molecule on the lipid monolayer (46) and the electron relaxation time that might also affect the simulation result (44,47-48). Third, although the internalization of Gd chelates was confirmed by intracellular ^1H relaxation enhancement using cultured cells, neutron activation would provide a more quantitative measurement (16). Finally, the shielding effect of the chelate on the Gd electron spin has been neglected by assuming the same magnetic moment of Gd ions for DOTA and DTPA. Nevertheless, this theoretical framework might be expected to facilitate future chemical modifications and applications of such agents with the goal of optimizing their sensitivity and utility in clinical molecular imaging with unique, no background, and quantifiable readouts of physiological and pathological biomarkers.

4.6 References

1. Kaneda MM, Caruthers S, Lanza GM, Wickline SA. Perfluorocarbon nanoemulsions for quantitative molecular imaging and targeted therapeutics. Ann Biomed Eng 2009;37(10):1922-1933.
2. Yu JX, Cui W, Zhao D, Mason RP. Non-invasive physiology and pharmacology using 19f magnetic resonance. In: Tressaud A, Haufe G, eds. Fluorine and health: Elsevier B.V., 2008; 198-276.
3. Thomas S. The biomedical applications of fluorine-19 nmr. In: Partain C, Price R, Patton J, Kulkarni M, James A, eds. Magnetic resonance imaging. London: W.B. Saunders Co., 1988; 1536-1552.
4. Wickline SA, Mason RP, Caruthers SD, et al. Fluorocarbon agents for multimodal molecular imaging and targeted therapeutics. In: Weissleder R, Ross BD, Rehemtulla A, Gambhir SS, eds. Molecular imaging: Principles and practice: Peoples Medical Publishing House-USA, 2010; 542-573.
5. Winter PM, Schmieder AH, Caruthers SD, et al. Minute dosages of alpha(nu)beta3-targeted fumagillin nanoparticles impair Vx-2 tumor angiogenesis and development in rabbits. FASEB J 2008;22(8):2758-2767.
6. Winter PM, Morawski AM, Caruthers SD, et al. Molecular imaging of angiogenesis in early-stage atherosclerosis with alpha(v)beta3-integrin-targeted nanoparticles. Circulation 2003;108(18):2270-2274.
7. Winter PM, Caruthers SD, Kassner A, et al. Molecular imaging of angiogenesis in nascent Vx-2 rabbit tumors using a novel alpha(nu)beta3-targeted nanoparticle and 1.5 tesla magnetic resonance imaging. Cancer Res 2003;63(18):5838-5843.

8. Partlow KC, Chen J, Brant JA, et al. 19F magnetic resonance imaging for stem/progenitor cell tracking with multiple unique perfluorocarbon nanobeacons. FASEB J 2007;21(8):1647-1654.

9. Neubauer AM, Caruthers SD, Hockett FD, et al. Fluorine cardiovascular magnetic resonance angiography in vivo at 1.5 T with perfluorocarbon nanoparticle contrast agents. J Cardiovasc Magn Reson 2007;9(3):565-573.

10. Caruthers SD, Neubauer AM, Hockett FD, et al. In vitro demonstration using 19F magnetic resonance to augment molecular imaging with paramagnetic perfluorocarbon nanoparticles at 1.5 Tesla. Invest Radiol 2006;41(3):305-312.

11. Morawski AM, Winter PM, Yu X, et al. Quantitative "magnetic resonance immunohistochemistry" with ligand-targeted (19)F nanoparticles. Magn Reson Med 2004;52(6):1255-1262.

12. Flaim SF. Pharmacokinetics and side effects of perfluorocarbon-based blood substitutes. Artif Cells Blood Substit Immobil Biotechnol 1994;22(4):1043-1054.

13. Waters EA, Chen J, Yang X, et al. Detection of targeted perfluorocarbon nanoparticle binding using 19F diffusion weighted MR spectroscopy. Magn Reson Med 2008;60(5):1232-1236.

14. Parhami P, Fung BM. F-19 Relaxation Study of Perfluoro Chemicals as Oxygen Carriers. J Phys Chem-Us 1983;87(11):1928-1931.

15. Lee H, Price RR, Holburn GE, Partain CL, Adams MD, Cacheris WP. In vivo fluorine-19 MR imaging: relaxation enhancement with Gd-DTPA. J Magn Reson Imaging 1994;4(4):609-613.

16. Neubauer AM, Myerson J, Caruthers SD, et al. Gadolinium-Modulated F-19 Signals From Perfluorocarbon Nanoparticles as a New Strategy for Molecular Imaging. Magnetic Resonance in Medicine 2008;60(5):1066-1072.

17. Hodges MW, Cafiso DS, Polnaszek CF, Lester CC, Bryant RG. Water translational motion at the bilayer interface: An NMR relaxation dispersion measurement. Biophys J 1997;73(5):2575-2579.

18. Polnaszek CF, Bryant RG. Self-Diffusion of Water at the Protein Surface - a Measurement. Journal of the American Chemical Society 1984;106(2):428-429.

19. Berner B, Kivelson D. Paramagnetically Enhanced Relaxation of Nuclear Spins - Measurement of Diffusion. J Phys Chem-Us 1979;83(11):1401-1405.

20. Bloembergen N. Proton Relaxation Times in Paramagnetic Solutions. J Chem Phys 1957;27(2):572-523.

21. Solomon I. relaxation processes in a system of two spins. Physical Review 1955;99(2):559-565.

22. Bloembergen N, Morgan LO. Proton Relaxation Times in Paramagnetic Solutions. Effects of Electron Spin Relaxation. J Chem Phys 1961;34:842-850.

23. Sharp RR. Nuclear-Spin Relaxation in Paramagnetic Solutions - Effects of Large Zero-Field Splitting in the Electron-Spin Hamiltonian. J Chem Phys 1990;93(10):6921-6928.

24. Kruk D, Nilsson T, Kowalewski J. Nuclear spin relaxation in paramagnetic systems with zero-field splitting and arbitrary electron spin. Phys Chem Chem Phys 2001;3(22):4907-4917.

25. Kruk D, Kowalewski J. General treatment of paramagnetic relaxation enhancement associated with translational diffusion. J Chem Phys 2009;130(17):174104.

26. Belorizky E, Fries PH, Helm L, et al. Comparison of different methods for calculating the paramagnetic relaxation enhancement of nuclear spins as a function of the magnetic field. J Chem Phys 2008;128(5):052315

27. Sharp R, Lohr L, Miller J. Paramagnetic NMR relaxation enhancement: recent advances in theory. Prog Nucl Mag Res Sp 2001;38(2):115-158.

28. Partlow KC, Lanza GM, Wickline SA. Exploiting lipid raft transport with membrane targeted nanoparticles: a strategy for cytosolic drug delivery. Biomaterials 2008;29(23):3367-3375.

29. Abragam A. The principles of nuclear magnetism. Oxford,: Clarendon Press; 1961. p 271-301.

30. Kodibagkar VD, Wang XH, Mason RP. Physical principles of quantitative nuclear magnetic resonance oximetry. Front Biosci 2008;13:1371-1384.

31. Korb JP, Ahadi M, Zientara GP, Freed JH. Dynamic Effects of Pair Correlation-Functions on Spin Relaxation by Translational Diffusion in Two-Dimensional Fluids. J Chem Phys 1987;86(3):1125-1130.

32. Cherry RJ. Rotational and Lateral Diffusion of Membrane-Proteins. Biochim Biophys Acta 1979;559(4):289-327.

33. Torrey HC. Citation Classic - Nuclear-Spin Relaxation by Translational Diffusion. Cc/Phys Chem Earth 1984(46):16-16.

34. Winter P, Athey P, Kiefer G, et al. Improved paramagnetic chelate for molecular imaging with MRI. J Magn Magn Mater 2005;293(1):540-545.

35. Seymour JD, Caprihan A, Altobelli SA, Fukushima E. Pulsed gradient spin echo nuclear magnetic resonance imaging of diffusion in granular flow. Physical Review Letters 2000;84(2):266-269.

36. Giraudeau C, Flament J, Marty B, et al. A new paradigm for high-sensitivity 19F magnetic resonance imaging of perfluorooctylbromide. Magn Reson Med 2010;63(4):1119-1124.

37. Xie W, Ludewig G, Wang K, Lehmler HJ. Model and cell membrane partitioning of perfluorooctanesulfonate is independent of the lipid chain length. Colloid Surface B 2010;76(1):128-136.

38. Xie W, Bothun GD, Lehmler HJ. Partitioning of perfluorooctanoate into phosphatidylcholine bilayers is chain length-independent. Chem Phys Lipids 2010;163(3):300-308.

39. Kaneda MM, Sasaki Y, Lanza GM, Milbrandt J, Wickline SA. Mechanisms of nucleotide trafficking during siRNA delivery to endothelial cells using perfluorocarbon nanoemulsions. Biomaterials 2010;31(11):3079-3086.

40. Buffy JJ, Hong T, Yamaguchi S, Waring AJ, Lehrer RI, Hong M. Solid-state NMR investigation of the depth of insertion of protegrin-1 in lipid bilayers using paramagnetic Mn2+. Biophys J 2003;85(4):2363-2373.

41. Liang B, Bushweller JH, Tamm LK. Site-directed parallel spin-labeling and paramagnetic relaxation enhancement in structure determination of membrane proteins by solution NMR spectroscopy. J Am Chem Soc 2006;128(13):4389-4397.

42. Jackson JD. Classical electrodynamics. New York,: Wiley; 1962. 641 p.

43. Ellena JF, Obraztsov VV, Cumbea VL, Woods CM, Cafiso DS. Perfluorooctyl bromide has limited membrane solubility and is located at the bilayer center. Locating small molecules in lipid bilayers through paramagnetic enhancements of NMR relaxation. J Med Chem 2002;45(25):5534-5542.

44. Freed JH. Dynamic Effects of Pair Correlation-Functions on Spin Relaxation by Translational Diffusion in Liquids .2. Finite Jumps and Independent T1 Processes. J Chem Phys 1978;68(9):4034-4037.

45. Kok MB, de Vries A, Abdurrachim D, et al. Quantitative (1)H MRI, (19)F MRI, and (19)F MRS of cell-internalized perfluorocarbon paramagnetic nanoparticles. Contrast Media Mol Imaging 2010. DOI:10.1002/cmmi.39

46. Lee S-J, Olsen B, Schlesinger PH, Baker NA. Characterization of Perfluorooctylbromide-Based Nanoemulsion Particles Using Atomistic Molecular Dynamics Simulations. Journal of Physical Chemistry B Accepted for publication.

47. Powell DH, NiDhubhghaill OM, Pubanz D, et al. Structural and dynamic parameters obtained from O-17 NMR, EPR, and NMRD studies of monomeric and dimeric Gd3+ complexes of interest in magnetic resonance imaging: An integrated and theoretically self consistent approach. Journal of the American Chemical Society 1996;118(39):9333-9346.

48. Grebenkov DS. NMR survey of reflected Brownian motion. Rev Mod Phys 2007;79(3):1077-1137.

5 Noninvasive blood oxygenation measurement using ^{19}F MRI

5.1 Introduction

Blood oxygen tension (pO_2) is an essential pathophysiological index of circulatory and respiratory health that is useful for characterizing various disorders such as congenital heart disease (1), arteriovenous malformations (2), atherosclerotic dysfunction (3), and overt or occult heart failure in general (4). The current gold standard for pO_2 measurement entails direct blood sampling using arterial puncture, or invasive catheterization when A-V O_2 differences, or cardiac output and oxygen consumption data are needed.

MRI has been exploited as an alternative tool for non-invasive assessment of blood oxygenation based on blood-oxygenation-level-dependant (BOLD) MRI determined ^{1}H R2* (5), susceptibility (6), or T2 and T1 contrast (7-8). Among these methods, R2* and susceptibility contrast generated by deoxygenated-hemoglobin (deoxy-Hb) can be used to estimate deoxy-Hb concentration and blood saturation (SO_2) because deoxy-Hb is highly paramagnetic. Nevertheless, the readout of BOLD and susceptibility-dependent contrast is qualitative, or otherwise requires organ-specific prior knowledge to build complex mathematical models (5-6). Blood flow imaging with global T2 preparation has also been employed to measure blood oxygenation because of its linear correlation with blood ^{1}H R2. However, for *in vivo* studies, B_1 and B_0 inhomogeneity and pulsatile flow artifacts pose major obstacles for effective spin preparation and consistent R2 estimation (8). Additionally, blood ^{1}H R1 is also linearly responsive to dissolved pO_2 and thus may also be employed as a quantitative marker for blood oxygenation. However, because of the limited solubility of O_2 in plasma, the slope of ^{1}H R1 as a

function of pO_2 is as low as $2\times10^{-4}s^{-1}$/mmHg, resulting in significant uncertainty for *in vivo* pO_2 quantification (7).

Perfluorocarbon nanoparticles (PFC NPs) have been proposed as an ^{19}F MR pO_2 sensor (9-10) as a consequence of two attributes: (a) O_2 is a weakly paramagnetic molecule with unpaired electrons and net magnetization; (b) O_2 exhibits high solubility in PFC; (c) the linear O_2 release response curve of PFC and the free O_2 diffusion between PFC and surrounding environment render PFC as a reliable pO_2 probe for *in vivo* applications of measuring vascular pO_2 (11-12) and tissue oxygenation (9,13-14). Previous reports have demonstrated that the slope of ^{19}F R1 of PFC as a function of pO_2 could be ten-fold greater than the dependence of ^{1}H R1 on pO_2 (12-13,15). Additionally, because the lipid monolayer of PFC NPs is impermeable to macromolecules and ions, free paramagnetic macromolecules and ions in the blood stream do not affect the measurement of ^{19}F R1 emanating from PFC NPs, or its dependency on pO_2 (16). Finally, as a FDA-approved oxygen delivery vehicle, PFC NPs exhibit an acceptable bio-safety profile for ultimate clinical use (17-18).

Similar to ^{1}H MRI (19-22), one major obstacle of intravascular pO_2 measurements based on ^{19}F T1 of PFC NPs is the blood pulsatile motion artifact and in-flow effect. Other limitations include relatively low signal-to-noise ratio (SNR) due to limited amount of injected PFC NPs in the blood pool, and the inhomogeneity of spin preparation due to the movement of arterial blood through a large portion of body during the relaxation measurement. Therefore, the implementation of novel ^{19}F MRI strategies to minimize these artifacts would be critical to blood pO_2 measurements obtained by ^{19}F MRI relaxometry.

In the present work, we have first demonstrated the feasibility of imaging blood vasculature using ^{19}F MRI of circulating PFC NP. We have developed a novel Blood flow-

Enhanced-Saturation-Recovery (BESR) sequence for measuring ^{19}F T1 of flowing PFC NPs in blood pool. The BESR sequence preserves the time efficiency of the classical Look-Locker sequence and the high SNR of saturation recovery sequence. We first performed a computer simulation to illustrate the homogeneity of spin preparation in the BESR sequence, and to define the effect of limited SNR on the precision of the pO_2 measurement. The accuracy of BESR sequence measured T1 was tested on a phantom and evaluated *in vivo* by measuring arterial ^{1}H T1 in carotid arteries and cardiac ventricles. Finally, we optimized scan times and PFC NPs doses in conjunction with the BESR sequence for ^{19}F imaging of circulating PFC NPs to provide a quantitative estimate of arterial and venous pO_2 in mouse heart ventricles under both normoxia and hyperoxia conditions.

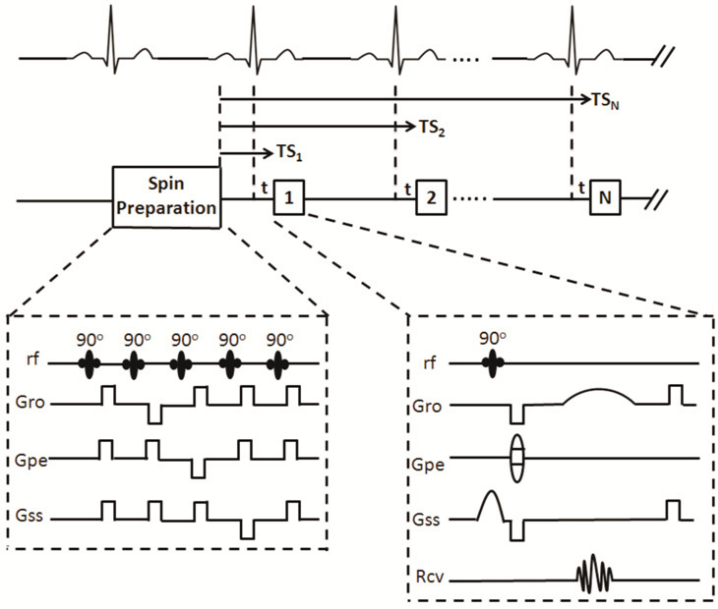

Figure 5.1 Illustration of the Blood flow-Enhanced-Saturation-Recovery (BESR) sequence. Spin preparation is achieved with multiple non-selective saturation pulses; image acquisition uses a gradient echo approach with cardiac triggering; saturation pre-pulse train and gradient echo imaging are both triggered by ECG. Each image acquisition is acquired at the same trigger delay time t but corresponds to different saturation delay time TS.

5.2 Material and Methods

The BESR sequence was implemented and all images were acquired on a 4.7 T Varian INNOVA scanner. All procedures in this study conformed to the guidelines and approvals by the Animal Studies Committee of Washington University in St. Louis.

5.2.1 Blood vessel imaging using ^{19}F MRI of circulating PFC NP

A healthy Swiss Webster mouse was anesthetized with ketamine/xylazine followed by intravenous injection of 40% v/v perfluoro-15-crown-5-ether (CE) NP (5ml/kg). A ^{19}F gradient echo imaging in the transverse plane of the neck region was performed to visualize the blood vasculature in this region. Detailed imaging parameters were TR = 500 ms, flip angle = 90°, TE = 2.5 ms, thickness = whole projection, in plane resolution = 0.3 mm × 0.3 mm. Another Swiss Webster mouse underwent unilateral carotid artery thrombotic injury induced by $FeCl_3$. The aforementioned ^{19}F MRI and conventional 2D time-of-flight ^{1}H angiography were performed to evaluate the void of flow at the injured site.

5.2.2 Pulse sequence and imaging setup

The BESR pulse sequence is designed for measurement of pO_2 in pulsatile blood flow. It is composed of two parts: homogeneous spin preparation and time-of-flight image acquisition (Figure 5.1). The spin preparation is achieved with a non-selective whole body saturation pulse train and the image acquisition is realized with gradient echoes at high repetition rate. Both the pre-pulses and imaging excitation pulses are gated to the ECG with appropriate trigger delay to minimize the motion artifact associating with the beating heart and vascular contraction and dilation.

In contrast to measuring the T1 of solid tissues, the spin preparation for measuring T1 of flowing blood should be non-selective and homogenous over the entire subject because spins in

the blood that will be excited for imaging might arise from a variety of locations during the spin preparation step (22-23). To achieve homogeneous spin preparation, an actively-decoupled transmit-only saddle coil (O.D. = 7cm, length = 12 cm) that covers the entire mouse body and a composite RF saturation pulse train comprising five constitutive 90° sinc-shaped pulses are employed. The bandwidth of each saturation pulse is 12 kHz and the time delay between two adjacent saturation pulses is 2 ms, during which crusher gradients are applied along different directions. The homogeneity of spin preparation is expected to improve progressively with the number of 90° pulses in the saturation pulse train. Specifically, $s(x, y, z)$, the percentage residual magnetization along z direction in a voxel positioned at (x, y, z) after n closely spaced saturation pulses followed by crusher gradients can be written as

$$s(x, y, z) = [\cos(\varphi(x, y, z))]^n, \qquad [1]$$

where $\varphi(x, y, z)$ is the flip angle at (x, y, z) and is determined by the B_1 field profile according to $\varphi(x, y, z) = B_1(x, y, z)\tau\gamma$, where γ is the Larmor frequency and τ is the pulse width. To confirm the homogenous saturation over the region of interest (ROI), we first acquired a flip angle mapping of our transmit coil on a water phantom (D = 6 cm, length = 10 cm) using a dual angle B1 mapping approach with α = 30° (24). Quantitative residual magnetization mapping after various number of saturation pulses (NSP) was then obtained by adjusting NSP in the BESR sequence.

In traditional ^{1}H saturation recovery T1 mapping, only one imaging excitation pulse is allowed within a single TR to avoid partial saturation effects arising from frequent repetitive excitations (25). In contrast, because of relatively fast blood flow in major blood vessels (>1 cm/s) and the "time-of-flight" effect, we anticipate that excited spins in the previous echo will flow out of the imaging slice as long as the time interval between two temporally adjacent

excitation pulses is sufficiently long (e.g., >0.2 s for 2 mm slice). Within a single TR of the BESR sequence, multiple 90° excitations, each followed by a same phase encoding gradient, are applied for gradient echo imaging. Thus, all echoes acquired in a single TR correspond to the same k-space line at different saturation delays (TS). All the imaging excitation pulses are synchronized with the ECG to minimize the effect of heart rate variations during imaging (26). Finally, to achieve an optimal SNR with BESR sequence, a dedicated actively-decoupled receive-only surface coil (diameter ≈ 3 cm) is placed close to the region of interest for signal reception.

5.2.3 Estimating the effect of SNR on the accuracy of pO_2 measurement

The uncertainty of the pO_2 estimation caused by random noise in saturation recovery imaging was evaluated using computer simulations in Matlab (Mathworks, USA) and conventional saturation recovery imaging on PFC NPs phantoms. A region of interest (ROI) containing 100 pixels was defined to simulate the number of pixels in heart ventricles. Normally distributed Gaussian noise was imposed on the ^{19}F signal intensity in each pixel to achieve variable SNR. The average noise-contaminated signal in entire ROI was used for non-linear fitting of T1 values. The conversion between T1 and pO_2 values was based on the pre-acquired calibration curve. In the simulation, the following saturation delays were used: TS = 0.25, 0.5, 0.75, 1, 1.25, 1.5, 1.75, 2 and 10 s. Simulation was repeated 10000 times and the standard deviation of the fitted pO_2 was calculated to represent the measurement uncertainty propagated from imaging noise through non-linear fitting. For phantom imaging, three PFC NPs phantoms with volume concentration of 5%, 10% and 20% were sequentially bubbled with N_2, room air and O_2 for 10 minutes. The phantom temperature was maintained at 37°C with a circulating water bath. A saturation recovery fast spin echo sequence was used for T1 mapping: TR=3 s,

FOV=25 cm × 25 cm, TE = 8.6 ms, echo train length = 16, Matrix size=128 × 128. The standard deviation of the fitted pO_2 values for each single pixel was used to calculate the uncertainty of pO_2 estimate in an ROI containing 100 pixels.

5.2.4 *In vitro* and *in vivo* validation of BESR sequence

The accuracy and precision of the BESR sequence was tested by measuring ^{1}H T1 of circulating water in a tube phantom, which simulated the *in vivo* setting of ^{19}F MRI with all signal contributed only by intravascular PFC NPs devoid of tissue background. Briefly, approximately 80 cm silicon tubing (1/8" inner diameter) was twisted and coiled to form an 8-cm long phantom with multiple loops. The phantom was then connected to a pump to generate constant 5 cm/s flow velocity to mimic blood flow. The special design of the phantom together with the carefully chosen flow velocity simulate the blood flow situation *in vivo*, such that the flowing water could experience a homogenous spin preparation at the beginning of each TR (5 s) , but is moving rapidly enough to generate the desired "time-of-flight" effect to replenish the imaging slice with unexcited spins before each gradient-echo (10 echoes in each TR ranging from 0.1 s to 4.6 s time interval between consecutive imaging acquisitions = 0.5 s). Upon the completion of BESR measurement, the pump was turned off and the ^{1}H T1 of stationary water was measured with a saturation recovery fast spin echo sequence. The image parameters of fast spin echo were TR=5 s, TE = 8.6 ms, echo train length =16, TS=0.1 to 4.6 s with intervals of 0.5 s.

To confirm that the BESR sequence can achieve reproducible T1 measurements *in vivo*, ^{1}H T1 measurements of flowing arterial blood in carotid arteries and heart ventricles were acquired in Swiss Webster mice (n=5) at 4.7 T. Mice were anesthetized through inhalation of 1.5% isoflurane ventilated by pure O_2 (2 L/min). Body temperature was maintained at 37°C and

ECG was monitored with a small animal monitor system (SAI Inc., USA). During MRI, the isoflurane level was adjusted to maintain mouse heart rate at around 350 bpm. Imaging parameters were: TR=2.5 s, TE = 2.8 ms, FOV=25 cm×25 cm, matrix size=96×96 and number of TS=7. After *in vivo* imaging, mice were sacrificed and blood was collected from LV. T1 of the collected stationary blood was measured using a custom-built solenoid coil and traditional inversion recovery spectroscopy at 37°C after saturating with pure O_2.

5.2.5 PFC NP formulation and in vitro T1 calibration

Perfluoro-15-crown-5-ether (CE) nanoparticles were formulated as previously described. Briefly, the CE emulsion was composed of 40% (v/v) of CE (Exfluor Research Corp., USA), 2.0% (w/v) of a surfactant commixture, and 1.7% (w/v) glycerin, with water comprising the balance. In vitro calibration of ^{19}F R1 as a function of pO_2 was performed at three different O_2 concentrations (0%, 21%, and 100% O_2 balanced with N_2) by bubbling gas mixture into a CE emulsion sample for 30–60 min at both room temperature and 37°C. ^{19}F T1 measurements were made using inversion recovery spectroscopy with TR=10 s, and 10 inversion delays (TI) ranging from 3 ms to 5 s. To confirm that the linear response curve of CE NP on pO_2 was preserved in the blood, mouse blood (Bioreclamation, LLC, USA) containing 10% volume/volume ratio of CE NP was placed in a gas chamber to allow gas exchange through semi-permeable silicon tubing for 30 minutes. Blood was transferred to a sealed vial and the sample temperature was maintained at 37°C. For the linear fitting, the conversion of partial percentage of oxygen to mmHg was based on the assumption that 100% oxygen is equivalent to 713 mmHg (considering the vapor pressure at 37°C is 47 mmHg).

5.2.6 Noninvasive intravascular pO_2 measurement with BESR ^{19}F imaging

Swiss Webster mice (n=5) were anesthetized with 1-2% isoflurane mixed with room air or O_2 followed by intravenous injection of CE NP (5 ml/kg) via the tail vein. The ^{19}F signal from isoflurane was barely detectable by MRI in contrast to the strong ^{19}F single emanating from CE NP in the blood stream, which is likely due to low blood/tissue retention and the short T2* of isoflurane (27).^{1}H gradient-echo cine images were acquired initially to position the slices to cover both left and right ventricles (LV and RV). Blood ^{19}F T1 measurements were carried out under separate conditions of room air and then pure oxygen ventilation. The saddle coil and the surface coil were re-tuned as needed to the proper frequency of 201.5 MHz and 189.6 MHz for ^{1}H and ^{19}F imaging, respectively. Parameters for ^{19}F BESR T1 measurement were: TR, 2.5 s; TE, 2.2 ms; number of points along recovery curve, 8; number of averages, 16; in plane resolution, 1.5 mm × 0.75 mm; slice thickness, 2 mm. In order to optimize non-linear fitting for ^{19}F T1 of less-oxygenated venous blood exhibiting T1 > 2 s, another set of BESR images acquired with identical imaging parameters but without pre-saturation pulses were used as fully recovered signal. The previously measured ^{19}F R1 vs pO_2 calibration curve was used for quantifying intravascular pO_2 *in vivo*.

5.2.7 Data analysis and statistics

The left and right ventricles and vessel lumen were manually segmented on ^{1}H and ^{19}F images. ROI was defined as the region exhibiting > 3 SD higher ^{19}F signal intensity, i.e., signal contributed by PFC NPs in the blood, as compared with that of surrounding tissues. The average intensity in each ROI was used for fitting data to a 3-parameter saturation recovery curve:

$$S(TS) = A - Be^{-TS/T_1}. \qquad [2]$$

All statistical analysis was performed using Origin software (OriginLab, USA). Metrics for precision and accuracy of T1 measurements with the BESR sequence were assessed based on ^{1}H image of the tubing phantom. The precision error was calculated as the root-mean-square of 5 individual measurement normalized by the mean value, and the accuracy error was considered to be the relative difference between the T1 mean value measured using a reference method and the BESR sequence. A two sample paired *t*-test was used for statistical analysis to test the difference between BESR measured ^{1}H T1 values and reference ^{1}H T1 values *in vivo*, and the difference of ^{19}F MRI determined pO_2 between hyperoxic and normoxic conditions. A significance threshold of $p < 0.05$ was used for hypothesis testing.

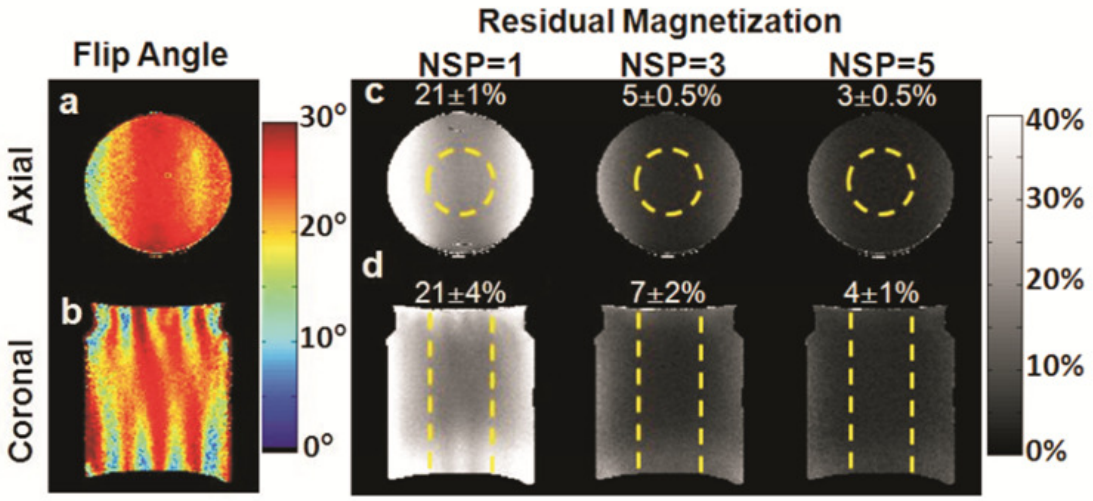

Figure 5.2 Saturation profile of saturation pulse train of BESR sequence. (a, b) Flip angle mapping of a water phantom in axial and coronal plane. (c, d) Measured residual magnetization after different number of saturation pulses (NSP = 1, 3, 5) in axial and coronal plane. The yellow dashed lines represent the border of the ROI for *in vivo* study. The residual magnetization inside the ROI is presented as mean ± standard deviation.

5.3 Results

5.3.1 Measurement of the homogeneity of pulse train saturation

The flip angle mapping of the transmit coil and the percentage residual magnetization intensity after different number of saturation pulses (1, 3, and 5) were measured experimentally and shown in Figure 5.2. As the number of saturation pulses increased, spin nulling in the whole FOV became more uniform despite the inhomogenity of the B1 profile. After five consecutive 90° pulses, the residual magnetization within the ROI where mice were placed for *in vivo* experiments (border marked by yellow dash line) was < 4%, substantially lower than the > 20% residual magnetization after a single saturation pulse.

5.3.2 ^{19}F MRI of PFC NP in the blood pool

PFC NP in blood vessels at the neck region was readily visualized using ^{19}F MRI (Figure 5.3). The angiograms generated from whole projection of ^{19}F MRI and maximal intensity projection (MIP) of ^{1}H angiography automatically co-registered with each other. Void of blood flow in the left carotid artery caused by the external injury was detected by both ^{19}F and ^{1}H angiography. It is notable that compared to ^{1}H MIP, ^{19}F angiography features a non-background delineation of blood vasculature.

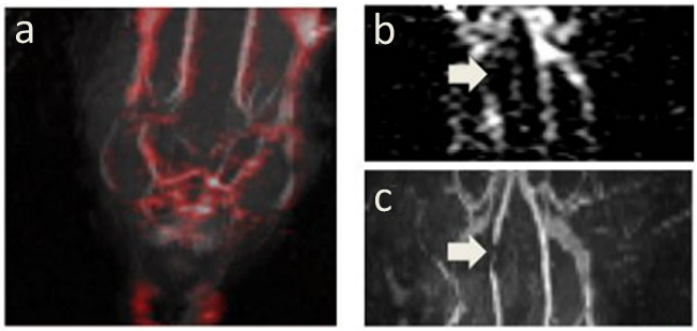

Figure 5.3 ^{19}F angiography in mouse. (a) shows a "maximal intensity projection" of the ^{1}H and ^{19}F angiograms at the neck of mouse, where blood vessel geometry is clearly depicted. The thrombus site in the carotid artery is visually appreciable in ^{19}F angiography (b), which is consistent with the time-of-flight ^{1}H imaging (c).

5.3.3 Validation of BESR sequence determined T1

The ^{1}H T1 measured in the tube phantom and in arterial blood flow is summarized as follows: BESR sequence determined ^{1}H T1 of circulating water (2.96 ± 0.43 s) was comparable to that of stationary water measured with a traditional saturation recovery sequence (3.30 ± 0.17 s, N.S.). The precision and accuracy errors were 13.0% and 10.3%, respectively. The precision and accuracy errors provide quantitative estimates for the potential measurement bias and uncertainty, respectively. The *in vivo* measured ^{1}H T1 in arterial blood (on 100% O_2) in left and right carotid arteries and left ventricle were 1.62 ± 0.12 s, 1.59 ± 0.2 s, and 1.67 ± 0.14 s, respectively. The corresponding in vitro T1 of sampled arterial blood saturated with 100% O_2 was 1.78 ± 0.18 s (N.S. compared to all *in vivo* measurements).

5.3.4 In vitro calibration of ^{19}F R1 as a function of pO_2

In vitro measurements validated the linear dependence of ^{19}F R1 on pO_2 (Figure 5.4). At 37°C,

$$R1(s^{-1}) = (0.396 \pm 0.014) + (0.0024 \pm 0.0003) \times pO_2(mmHg). \quad [3]$$

Deoxy-Hb did not exhibit any observable paramagnetic relaxation enhancement effect on ^{19}F T1, because ^{19}F R1 vs pO_2 curve was identical in aqueous solution and mouse blood.

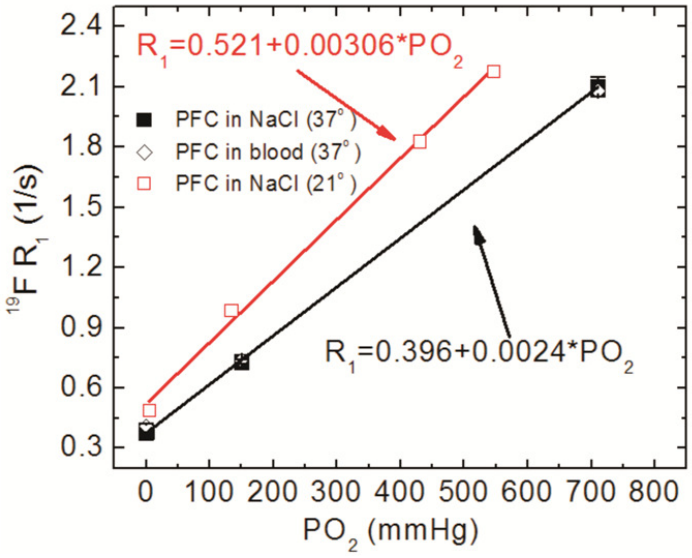

Figure 5.4 Calibrated linear relationship between ^{19}F R1 and pO_2 at room temperature and 37°. The calibration curve at 37° is used for the *in vivo* study. Error bars represent standard deviation.

5.3.5 *In vivo* measurement of blood oxygenation

Figure 5.5 shows representative BESR images of a mouse heart under hyperoxia and normoxia. After spin saturation, blood in the left ventricle (LV) exhibited a faster recovery of signal intensity than that in the right ventricle (RV), which was further accelerated when the mouse was breathing pure O_2 (i.e., hyperoxia). The fitted ^{19}F R1 confirmed the faster relaxation of the more oxygenated blood. Based on the calibrated correlation between ^{19}F R1 and pO_2 (Eq. 3), ^{19}F MRI-measured LV blood pO_2 was 458 ± 133 mmHg under hyperoxia and 96 ± 21 mmHg under normoxia; significantly higher than RV blood pO_2, which was 103 ± 21 mmHg under hyperoxia and 49 ± 15 mmHg under normoxia (Figure 5.6, $p < 0.05$ for all comparisons).

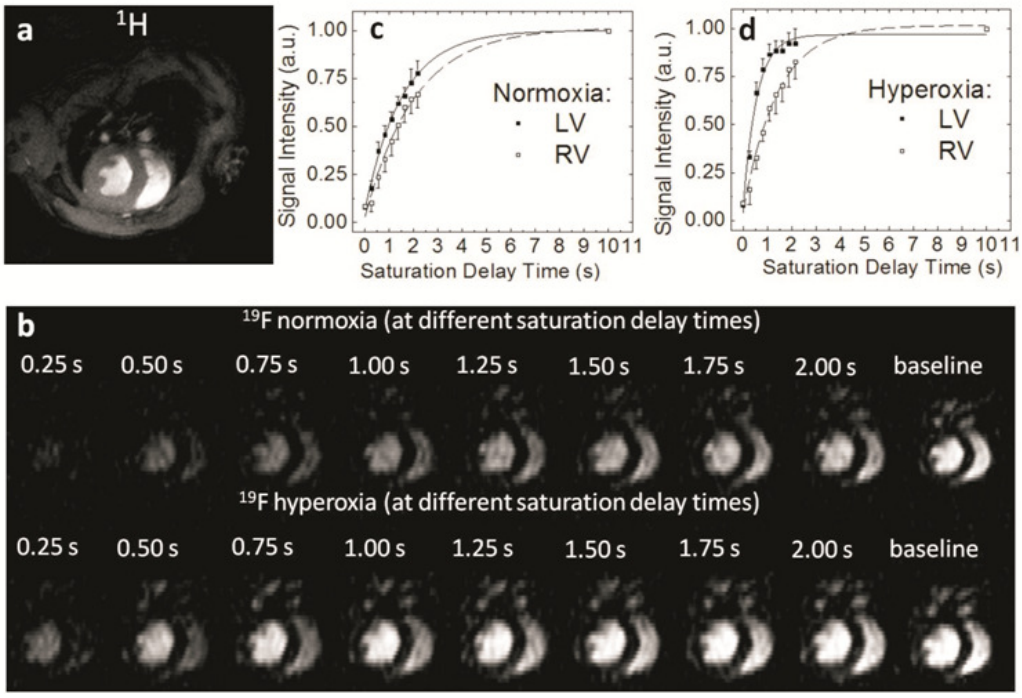

Figure 5.5 *In vivo* ^{19}F BESR MRI of heart ventricles. (a) A short-axis ^{1}H image shows the left and right ventricles. (b) ^{19}F BESR images of the same mouse heart under hyperoxia and normoxia. (c-d) Fitted ^{19}F saturation recovery curve for LV and RV blood under normoxia and hyperoxia. Error bars represent standard deviation.

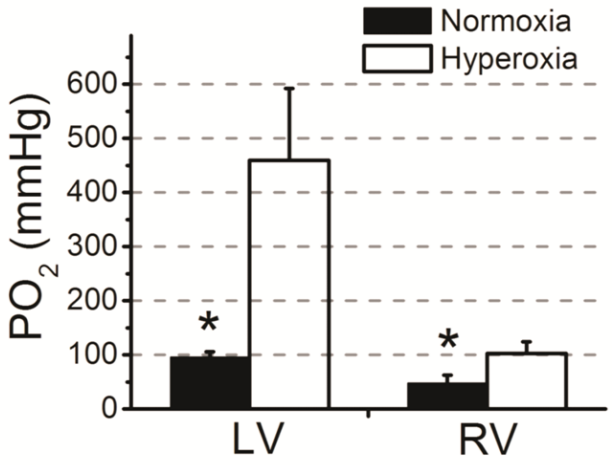

Figure 5.6 Ventricular pO_2 estimated using BESR sequence. Measured blood pO_2 based on measured ^{19}F T1 of PFC NPs showed pO_2 difference between LV and RV, and between normoxic and hyperoxic conditions for each ventricle, *, $p<0.05$.

5.3.6 Accuracy of pO_2 measurements at different SNR

Since low SNR is a common problem in ^{19}F MRI, the effect of SNR on ^{19}F BESR determined pO_2 was evaluated by mathematical simulation (Figure 5.7). As expected, the accuracy of ^{19}F MRI measurements of pO_2 increased with SNR. However, the pO_2 measurement was less susceptible to noise (in the sense of absolute measurement uncertainty) at lower oxygen tension. When image SNR = 9, the measurement error of ^{19}F MRI determined pO_2 was <10 mmHg under hypoxic condition (pO_2 <50 mmHg) and <40 mmHg under hyperoxic condition (pO_2 > 500 mmHg). Phantom studies with varying concentrations of PFC NPs (Figure 5.7b) confirmed the simulation result. Higher imaging SNR substantially reduced the uncertainty and increased the precision of the ^{19}F R1 measurements.

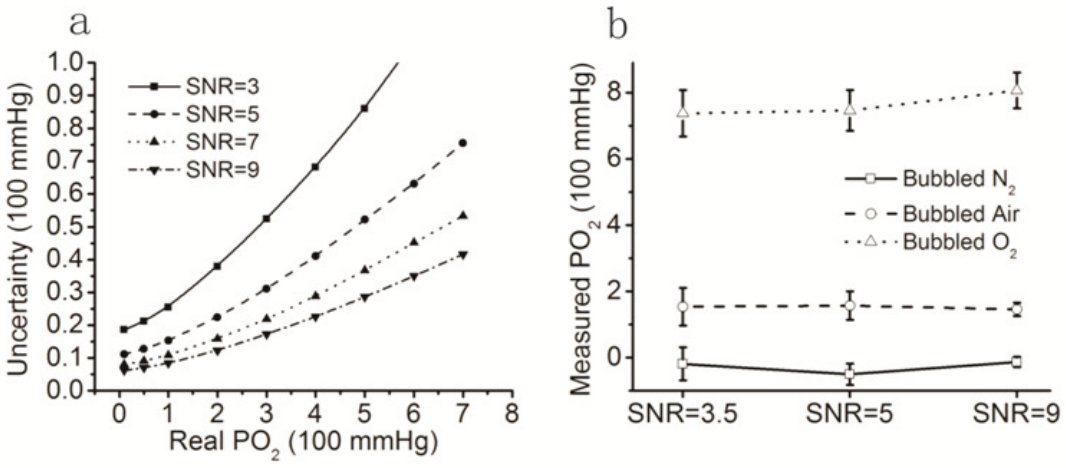

Figure 5.7 Effect of SNR on the accuracy of pO_2 measurement. (a) Simulation result shows measurement accuracy improves as SNR increases. pO_2 measurement uncertainty is higher under hyperoxic condition. (b) Measured pO_2 for three PFC NPs samples with different NP concentration bubbled with N_2, Air and O_2, respectively. The mean value of measured pO_2 is independent of PFC NPs concentration but measurement uncertainty (error bars) is suppressed by increased SNR.

5.4 Discussion

In the present work, we experimentally demonstrated the feasibility of ^{19}F angiography in mouse. We have implemented a novel BESR sequence to quantify blood pO_2 based on ^{19}F R1 of circulating PFC NPs. Because ^{19}F R1 of PFC NPs is not affected by the paramagnetic effect of deoxy-Hb and manifests a linear association/release curve as a function of dissolved $[O_2]$, it represents a promising probe to quantify blood pO_2. Our results demonstrate that the BESR sequence: 1) achieves a consistent T1 measurement for pulsatile blood flow, 2) differentiates blood pO_2 in the LV and RV, and 3) depicts the response of ventricular blood oxygenation to hyperoxic challenge.

One concern regarding the use of any oxygen sensing probe *in vivo* is whether other molecules or ions will affect the chemical properties of the probe. In this study, we observed that pO_2 - ^{19}F R1 relationship remained unchanged for PFC NPs in salt solution and blood sample. This is consistent with our previous findings that ^{19}F R1 of PFC NPs is not affected by surrounding free paramagnetic ions (16,28) since their direct interactions are prevented by the lipid monolayer of PFC NPs, which is permeable to O_2 but not to macromolecules. The observed linear pO_2 response curve of PFC NP agreed with that observed in previous reports despite the difference in the fitted coefficient at different magnet field strength (12,29-30).The observed temperature dependence of ^{19}F R1 has also been previously reported (15).

The long circulating half life time of PFC NPs and high ^{19}F spin density are advantageous to use PFC NPs as a blood pool pO_2 probe. The mean half life of PFC NPs in the blood plasma is ~180 minutes in mouse and even longer in humans (31). Thus, the slow clearance of intravascular PFC NPs allows a relatively wide temporal window for quantitative pO_2 assessment with ^{19}F MRI. In addition, even though PFC has high affinity for O_2, the modest administered dose is small enough such that the total amount of dissolved O_2 carried by PFC NPs is orders of magnitude less than that carried by plasma and red blood cells (dissolved plus oxy-hemoglobin) (32-34). Therefore, the blood-pool PFC NPs acted as a pO_2 sensor rather than a primary O_2 reservoir and the ^{19}F MRI measured pO_2 values reflects pO_2 in blood stream.

In major arteries (or ventricles), and veins, the velocity of blood flow is > 10 cm/s and 1 cm/s, respectively. For a typical imaging slice thickness (1-2 mm), the minimal time required for blood to flow through the slice is approximately 100-200 ms. By setting the time interval between two consecutive excitation pulses greater than 200 ms and selecting imaging slices

perpendicular to the flow direction, the previously excited spins should not affect the subsequent image acquisitions. Thus, gradient echo imaging with 90° excitation pulses can achieve maximal SNR without partial saturation effects. On the other hand, because the blood flow is rapid in major blood vessels, during the recovery process of the T1 measurement the real "imaged" spins within the region of interest may originate from distant locations. This requires homogeneous spin pre-saturation over a large volume of the imaged subject. Consistent with previous studies that utilized pre-saturation pulse trains (33,35), our result suggests that a non-selective saturation pulse train with crusher gradients was robust for reducing both B_0 and B_1 inhomogeneity while achieving a satisfactory uniform spin saturation profile. By implementing multiple saturation recovery acquisitions in each TR, the BESR sequence achieved higher SNR than traditional saturation recovery or inversion recovery T1 measurement sequences.

The novelty of BESR resides in the utilization of a homogenous RF pre-saturation and a train of ECG gated excitation/readouts in a single TR for fast T1 quantification. Due to the refreshing of intravascular PFC NP in the imaging slice (thickness = 2 mm) between adjacent heart beats, the acquired blood-pool ^{19}F signal by each readout directly represents the ^{19}F T1 recovery at corresponding delay times after saturation. In contrast, the conventional saturation pulse sequence only acquires one echo after each RF saturation, and the different T1 recovery weighting is achieved by varying TR (36). Thus, the BESR sequence provides a faster imaging method for quantifying blood ^{19}F T1 by taking advantage of the time-of-flight effect of blood-flow in conjunction with intravascular PFC NP contrast agent. Although multiple 90° pulses were used in this study, other pulse shapes such as adiabatic or composite pulses also could be employed as long as homogeneous whole-body saturation is achieved (37). Similarly, fast

imaging techniques like EPI could replace the single echo to further accelerate image acquisition (36).

The BESR sequence is optimized for ^{19}F MRI because: (a) the PFC NP is an intravascular agent; (b) there is no ^{19}F background in soft-tissue; (c) O_2 dissolving and release from PFC NP (~250 nm) operates through free diffusion that occurs in milliseconds (38). In capillaries, the measured pO_2 may directly reflect tissue pO_2 if the O_2 exchange between tissue and microvasculature is rapid (39). In ventricles and major blood vessel that experiencing no blood-tissue O_2 exchange, the measured pO_2 would represent venous or arterial blood pO_2. Finally, although the BESR sequence could be applied to quantify ^{1}H T1 in blood pool, the small correlation coefficient between ^{1}H R1 and pO_2 may be problematic for accurate pO_2 determination. Additionally, the O_2 release response curve of hemoglobin is non-linear, therefore the accuracy of ^{1}H MRI measured blood pO_2, as well as its relationship with tissue pO_2, remains to be defined.

The proposed ^{19}F imaging methodology has direct translational potential. The technique might be readily adapted to evaluate arteriovenous pO_2 difference for selected organs, e.g. renal arteries and veins for kidney, carotid arteries and jugular veins for brain, aorta and coronary sinus for heart, among others. Further integration of ^{19}F MRI determined A-V pO_2 with phase-contrast ^{1}H or ^{19}F MRI determined blood flow velocity may enable assessment of oxygen consumption in individual organs as a critical pathological marker for evaluating injury at a cellular level.

Based on the accuracy profile of ^{19}F-determined pO_2, imaging noise significantly affects the measurement uncertainty of pO_2 through non-linear T1 fitting. Therefore, the acquisition of ^{19}F images with sufficient SNR is crucial to accurately estimate intravascular pO_2, which also

was reported previously by Barker et al (14). In the present study, all images exhibited SNR > 7, and according to our simulation (Figure 5.6a), pO_2 estimates from these images could achieve a measurement uncertainty as low as 10 mmHg under normoxia and 30 mmHg under hyperoxia depending on real pO_2.

Several limitations of the current pO_2 measurement paradigm should be mentioned. Even though the blood flow in major blood vessels is fast enough to create "time-of-flight" phenomenon, the velocity profile of blood flow is laminar, where the velocity close to the blood vessels walls is virtually zero. This portion of the blood may contribute to ^{19}F signal resulting in reduced accuracy of pO_2 measurement in such regions (22). In the cardiac ventricles and major vessels, non laminar blood flow (e.g., turbulence) also may cause errors in T1 estimation due to spin de-correlation, which is not unexpected and can be visualized on ^{1}H images for proper data interpretation (40). Because the ejection fraction of normal ventricle is around 60%, after two heart beats around 16% residual blood still remains in the same ventricle. The residual blood may suffer from partial saturation from previous excitation and cause errors in T1 measurement. The systematic error (about 6% of T1 measured in phantom experiments) caused by these factors may be corrected by flow dynamical modeling in the future. The relative error of ^{19}F BESR MRI determined blood pO_2, (i.e., 50 mmHg) in well oxygenated arterial blood or in venous blood (10 mmHg), could limit the application of this technique for measurement of tumor oxygenation, but there are other uses that offer insights into myriad pathophysiologies. Finally, for human imaging, where sampling once per cardiac cycle is too slow because of lower heart rate, the sequence should be modified to image more than once per cardiac cycle.

5.5 References

1. Rudolph AM. Congenital diseases of the heart : clinical-physiological considerations. Armonk, NY: Futura Pub. Co.; 2001. viii, 808 p.

2. Terry PB, White RI, Barth KH, Kaufman SL, Mitchell SE. Pulmonary arteriovenous-malformations - physiologic observations and results of therapeutic balloon embolization. N Engl J Med 1983;308(20):1197-1200.

3. Fedele FA, Gewirtz H, Capone RJ, Sharaf B, Most AS. Metabolic response to prolonged reduction of myocardial blood flow distal to a severe coronary artery stenosis. Circulation 1988;78(3):729-735.

4. Grossman W. Cardiac catheterization and angiography. Philadelphia: Lea & Febiger; 1986. xiii, 562 p.

5. Silvennoinen MJ, Clingman CS, Golay X, Kauppinen RA, van Zijl PC. Comparison of the dependence of blood R2 and R2* on oxygen saturation at 1.5 and 4.7 Tesla. Magn Reson Med 2003;49(1):47-60.

6. Fujima N, Kudo K, Terae S, Hida K, Ishizaka K, Zaitsu Y, Asano T, Yoshida D, Tha KK, Haacke EM, Sasaki M, Shirato H. Spinal arteriovenous malformation: evaluation of change in venous oxygenation with susceptibility-weighted MR imaging after treatment. Radiology 2010;254(3):891-899.

7. Kershaw LE, Naish JH, McGrath DM, Waterton JC, Parker GJ. Measurement of arterial plasma oxygenation in dynamic oxygen-enhanced MRI. Magn Reson Med 2010;64(6):1838-1842.

8. Nield LE, Qi X, Yoo SJ, Valsangiacomo ER, Hornberger LK, Wright GA. MRI-based blood oxygen saturation measurements in infants and children with congenital heart disease. Pediatr Radiol 2002;32(7):518-522.

9. Mason RP, Jeffrey FM, Malloy CR, Babcock EE, Antich PP. A noninvasive assessment of myocardial oxygen tension: 19F NMR spectroscopy of sequestered perfluorocarbon emulsion. Magn Reson Med 1992;27(2):310-317.

10. Shukla HP, Mason RP, Bansal N, Antich PP. Regional myocardial oxygen tension: 19F MRI of sequestered perfluorocarbon. Magn Reson Med 1996;35(6):827-833.

11. Fishman JE, Joseph PM, Floyd TF, Mukherji B, Sloviter HA. Oxygen-sensitive 19F NMR imaging of the vascular system in vivo. Magn Reson Imaging 1987;5(4):279-285.

12. Duong TQ, Kim SG. In vivo MR measurements of regional arterial and venous blood volume fractions in intact rat brain. Magn Reson Med 2000;43(3):393-402.

13. Eidelberg D, Johnson G, Barnes D, Tofts PS, Delpy D, Plummer D, McDonald WI. 19F NMR imaging of blood oxygenation in the brain. Magn Reson Med 1988;6(3):344-352.

14. Barker BR, Mason RP, Bansal N, Peshock RM. Oxygen tension mapping with F-19 echo-planar MR imaging of sequestered perfluorocarbon. J Magn Reson Imaging 1994;4(4):595-602.

15. Liu S, Shah SJ, Wilmes LJ, Feiner J, Kodibagkar VD, Wendland MF, Mason RP, Hylton N, Hopf HW, Rollins MD. Quantitative tissue oxygen measurement in multiple organs using (19) F MRI in a rat model. Magn Reson Med 2011; 66(6):1722-30.

16. Hu L, Zhang L, Chen J, Lanza GM, Wickline SA. Diffusional mechanisms augment the fluorine MR relaxation in paramagnetic perfluorocarbon nanoparticles that provides a "relaxation

switch" for detecting cellular endosomal activation. J Magn Reson Imaging 2011; 34(3): 653-661.

17. Cohn CS, Cushing MM. Oxygen therapeutics: perfluorocarbons and blood substitute safety. Crit Care Clin 2009;25(2):399-414.

18. Wickline SA, Mason RP, Caruthers SD, Chen J, Winter PM, Hughes MS, Lanza GM. Fluorocarbon agents for multimodal molecular imaging and targeted therapeutics. In: Weissleder R, Ross BD, Rehemtulla A, Gambhir SS, editors. Molecular imaging: Principles and practice: Peoples Medical Publishing House-USA; 2010. p 542-573.

19. Wu WC, Jain V, Li C, Giannetta M, Hurt H, Wehrli FW, Wang DJ. In vivo venous blood T1 measurement using inversion recovery true-FISP in children and adults. Magn Reson Med 2010;64(4):1140-1147.

20. Thomas DL, Lythgoe MF, Gadian DG, Ordidge RJ. In vivo measurement of the longitudinal relaxation time of arterial blood (T1a) in the mouse using a pulsed arterial spin labeling approach. Magn Reson Med 2006;55(4):943-947.

21. Zheng J, Venkatesan R, Haacke EM, Cavagna FM, Finn PJ, Li D. Accuracy of T1 measurements at high temporal resolution: feasibility of dynamic measurement of blood T1 after contrast administration. J Magn Reson Imaging 1999;10(4):576-581.

22. Guo JY, Kim SE, Parker DL, Jeong EK, Zhang L, Roemer RB. Improved accuracy and consistency in T1 measurement of flowing blood by using inversion recovery GE-EPI. Med Phys 2005;32(4):1083-1093.

23. Dumoulin CL, Buonocore MH, Opsahl LR, Katzberg RW, Darrow RD, Morris TW, Batey C. Noninvasive measurement of renal hemodynamic functions using gadolinium enhanced magnetic resonance imaging. Magn Reson Med 1994;32(3):370-378.

24. Cunningham CH, Pauly JM, Nayak KS. Saturated double-angle method for rapid B1+ mapping. Magn Reson Med 2006;55(6):1326-1333.

25. Bernstein MA, King KF, Zhou ZJ. Handbook of MRI pulse sequences. Amsterdam ; Boston: Academic Press; 2004. xxii,1017 p.

26. Roth DM, Swaney JS, Dalton ND, Gilpin EA, Ross J, Jr. Impact of anesthesia on cardiac function during echocardiography in mice. Am J Physiol Heart Circ Physiol 2002;282(6):H2134-2140.

27. Chen M, Olsen JI, Stolk JA, Schweizer MP, Sha M, Ueda I. An in vivo 19F NMR study of isoflurane elimination as a function of age in rat brain. NMR Biomed 1992;5(3):121-126.

28. Neubauer AM, Myerson J, Caruthers SD, Hockett FD, Winter PM, Chen JJ, Gaffney PJ, Robertson JD, Lanza GM, Wickline SA. Gadolinium-Modulated F-19 Signals From Perfluorocarbon Nanoparticles as a New Strategy for Molecular Imaging. Magnetic Resonance in Medicine 2008;60(5):1066-1072.

29. Fan X, River JN, Muresan AS, Popescu C, Zamora M, Culp RM, Karczmar GS. MRI of perfluorocarbon emulsion kinetics in rodent mammary tumours. Phys Med Biol 2006;51(2):211-220.

30. Kadayakkara DK, Janjic JM, Pusateri LK, Young WB, Ahrens ET. In vivo observation of intracellular oximetry in perfluorocarbon-labeled glioma cells and chemotherapeutic response in the CNS using fluorine-19 MRI. Magn Reson Med 2010;64(5):1252-1259.

31. Spahn DR. Blood substitutes. Artificial oxygen carriers: perfluorocarbon emulsions. Crit Care 1999;3(5):R93-97.

32. Thomas SR, Pratt RG, Millard RW, Samaratunga RC, Shiferaw Y, Clark LC, Jr., Hoffmann RE. Evaluation of the influence of the aqueous phase bioconstituent environment on

the F-19 T1 of perfluorocarbon blood substitute emulsions. J Magn Reson Imaging 1994;4(4):631-635.

33. Mason RP, Shukla H, Antich PP. In vivo oxygen tension and temperature: simultaneous determination using 19F NMR spectroscopy of perfluorocarbon. Magn Reson Med 1993;29(3):296-302.

34. Lai C-S, Stair SJ, Miziorko H, Hyde JS. Effect of oxygen and the lipid spin label TEMPO-laurate on fluorine-19 and proton relaxation rates of the perlluoroehemical blood substitute, FC-43 emulsion. Journal of Magnetic Resonance (1969) 1984;57(3):447-452.

35. Evelhoch JL, Ackerman JJH. NMR T1 measurements in inhomogeneous B1 with surface coils. Journal of Magnetic Resonance (1969) 1983;53(1):52-64.

36. Le D, Mason RP, Hunjan S, Constantinescu A, Barker BR, Antich PP. Regional tumor oxygen dynamics: 19F PBSR EPI of hexafluorobenzene. Magn Reson Imaging 1997;15(8):971-981.

37. Tannus A, Garwood M. Adiabatic pulses. NMR Biomed 1997;10(8):423-434.

38. O'Brien RN, Langlais AJ, Seufert WD. Diffusion coefficients of respiratory gases in a perfluorocarbon liquid. Science 1982;217(4555):153-155.

39. Diepart C, Magat J, Jordan BF, Gallez B. In vivo mapping of tumor oxygen consumption using (19) F MRI relaxometry. NMR Biomed 2011;24(5):458-463.

40. Ehman RL, Felmlee JP. Flow artifact reduction in MRI: a review of the roles of gradient moment nulling and spatial presaturation. Magn Reson Med 1990;14(2):293-307.

6 Functional ^{19}F renal MRI

6.1 Introduction

In healthy kidneys, the countercurrent design of blood vessels and tubules maintains the necessary osmolar gradient to permit efficient urinary concentration, yet the system operates under conditions of a relatively hypoxic environment in some regions requiring extensive extraction of oxygen from flowing blood (1-4). During acute and chronic kidney injury, ischemia further hampers effective O_2 delivery to the capillary bed of renal tubules, as extraction of extra oxygen is marginal, resulting in exquisite susceptibility to ischemic damage to the renal medulla culminating in renal failure, hypertension from chronic kidney disease, and even death (5). Because acute kidney injury (AKI) is increasing in the hospitalized patient population, the development of quantitative and repeatable measurements of renal circulatory function (e.g. blood volume, perfusion, and regional oxygen tension) could enhance pathophysiological staging of the early disease process and its response to therapy (6). To this end, we sought to design and implement multiparametric quantifiable noninvasive imaging approaches that avoid the use of nephrotoxic contrast agents.

The current standard approaches for imaging renal perfusion entails bolus injection of exogenous contrast agents (e.g. iodinated compounds for CT, gadolinium chelates for MRI, etc.) following by a series of image acquisitions (e.g. X-ray, SPECT, PET, MRI) to capture the first-pass dynamics of contrast agents flowing through the kidney (7-9). Despite the general acceptance of these methods, heightened concern persists regarding their application in patients with potentially compromised kidney function (10). Indeed, the potential for contrast-induced nephropathy that can dramatically accelerate renal damage calls for great caution or even

avoidance of their use in the patients with acute and/or chronic kidney disease (11-14). Even with the use of gadolinium agents formerly thought to be devoid of such toxic side effects, slow and incomplete clearance can enhance susceptibility to untreatable conditions such as nephrogenic systemic fibrosis (15-16). Over the past two decades, the development of noncontrast MRI techniques has lead to promising new image-based measures of kidney function (17-19). Among these, Blood-Oxygenation-Level-Dependent (BOLD) MRI has demonstrated potential for correlating intrarenal oxygenation with ^{1}H susceptibility (T2*) measures (20). Arterial Spin Labeling (ASL) MRI also has been touted as a clinically available technique for defining renal perfusion without the need for exogenous contrast media (21). However, the lack of widespread adoption of available BOLD and ASL MRI methods raises questions as to their ultimate clinical utility (22-24).

Alternatively, Perfluorocarbon (PFC) based Nanoparticles (NPs) are a class of clinically approved vehicles recently applied *in vivo* for targeted molecular imaging and non-invasive oxygen tension (pO_2) assessment (25-26). As compared with iodinated or Gd contrast agent, PFC NPs may be especially suited to patients with kidney disease. As approved blood substitutes, PFC NPs are biologically inert and exhibit a good safety profile with no renal toxicity reported in both animals or human (27). Because PFC NPs (nominal size = 250 nm) are not cleared through glomerular filtration (28), they do not increase kidney workload, which is a major risk factor for kidney failure with other agents that undergo renal clearance (14). For imaging purposes, the unique ^{19}F MR signal emanating from the fluorine core of PFC NPs can be measured directly *in vivo* in rather sparse concentrations (picomolar) with no background signal as might be the case for other paramagnetic or superparamagnetic moieties that exert indirect contrast effects on circulating protons (29-30). PFC NPs have been demonstrated as effective functional probes for

both blood volume and pO_2 determination. Specifically, the detected ^{19}F signal intensity directly reflects the actual quantity of PFC NPs within a voxel. Furthermore, the ^{19}F longitudinal relaxation rate (R1) responds directly to local oxygen content in a linear manner (31-32).

Inflammation-coagulation interaction induced capillary non-perfusion is a primary pathology of AKI (33). Inflammation activates coagulation through three major pathways: thrombin generation mediated by tissue factor; fibrin deposition after fibrinolysis inhibition; and down-regulation of the protein C. The pro-coagulant effect could be further enhanced by the activated platelets (34-36). PPACK is a potent anti-coagulation agent that inhibits thrombin activation and interrupts fibrin formation (36). The binding of PPACK-thrombin complex to platelets inhibits their activation. We have recently demonstrated that PPACK loaded PFC NPs could function as an *in vivo* anti- coagulation agent that effectively delays arterial thrombosis in mice (37).

The objective of this study is to develop a ^{19}F MRI contrast paradigm for functional renal imaging. Here we demonstrate in healthy kidneys the feasibility of using ^{19}F MRI to directly register renal blood volume (RBV) and intrarenal oxygen tension pO_2. As compared with BOLD and ASL MRI, the^{19}F MRI method requires no model-based assumptions for absolute quantification of renal physiological indexes. To evaluate the diagnostic capability of kidney ^{19}F MRI, we tested the approach in an established mouse model of ischemia-reperfusion AKI (38). Based on the results, we propose that the functional readouts generated by ^{19}F MRI in concert with PFC NP, alone or perhaps combined with traditional BOLD MRI, could facilitate comprehensive quantitative assessment of micro-circulatory status in AKI.

6.2 Material and Methods

All procedures, including treatment, MRI imaging and animal surgery, in this study conformed to the guidelines of and with the approval of the Animal Studies Committee of Washington University in St. Louis.

6.2.1 Nanoparticle formulation and calibration of ^{19}F R1 vs pO_2

Perfluoro-15-crown-5-ether (CE) nanoparticles (NPs) were formulated as previously described (30). Briefly, the CE emulsion was composed of 40% (v/v) of CE (Exfluor Research Corp., USA), 2.0% (w/v) of a surfactant commixture, and 1.7% (w/v) glycerin, with water comprising the balance. CE NP was also co-labeled with Alexa Fluor 594 to enable *ex vivo* fluorescence microscopy examination. In vitro calibration of ^{19}F R1 as a function of pO_2 was performed at three different O_2 concentrations (0%, 21%, and 100% O_2 balanced with N_2) by bubbling gas mixtures into a CE emulsion sample for 30 minutes at 37°C. ^{19}F T1 measurements were made with inversion recovery spectroscopy at TR=10 s, with 10 inversion delays (TI) ranging from 3 ms to 5 s.

6.2.2 *In vivo* ^{19}F and BOLD MRI of kidney

Mice were anesthetized with a continuous intramuscular infusion of ketamine/xylazine. Body temperature was monitored and maintained at 37 ± 1°C during the MRI scans with the use of a small animal monitoring system (SAI Inc., USA) and a feedback controlled heated fan system. Mice were restrained in a custom-built holder and allowed to breathe pure oxygen through a nose cone. The respiratory signal was acquired from additional tubing connected to the nose cone and used as the gating trigger for *in vivo* imaging.

All *in vivo* imaging was performed on an 11.7 T Varian scanner with a custom-built actively decoupled coil pair. The transmit coil (5 cm by 10 cm) was built to cover the entire

imaging field of view, and optimized for superior field homogeneity and power transmit efficiency. Mice were imaged in a supine position and the surface receive coil (1 cm by 2 cm) was adjusted to match the mouse body curvature. Because of the strong magnetization originating from the high field strength, the ^{1}H signal was sufficient to generate high quality anatomical image within a minimal scan time (< 5 minutes) despite being slightly off-resonance. Thus, both transmit and receive coils were tuned and matched at ^{19}F frequency for both ^{19}F and ^{1}H imaging.

Before *in vivo* MRI, 0.1 mL (~ 5mL/Kg) CE NP was administrated intravenously through the tail vein. A ^{1}H gradient echo sequence was employed to locate the region of interest (ROI) followed by a ^{1}H multi-echo gradient echo BOLD scan with: TR = 100 ms, TE = 1.96 ms with 1.75 ms increment for every echo, flip angle = 10°, field of view = 26 mm × 26 mm, voxel size = 0.2 mm × 0.2 mm × 2 mm. Two sets of ^{19}F MRI scans (spin density weighted and T1-weighted images) were performed using a respiration-gated fast spin echo sequence. TR was set to 4 s for the spin density weighted ^{19}F MRI whereas the TR was set to two respiration periods for the T1-weighted imaging. All other imaging parameters are identical in these two sets of ^{19}F MRI: ETL = 4, TE = 11.5 ms, receive bandwidth =20 kHz, voxel size = 0.4 mm × 0.4 mm × 2 mm, and the field of view identical for ^{1}H scout and BOLD imaging.

6.2.3 Quantification of renal blood volume and intrarenal pO_2 (n = 5)

In order to quantify intrarenal blood volume and oxygenation, an external standard with known concentration of CE NP was placed at the edge of animal holder for all *in vivo* ^{19}F imaging. The CE NP reference comprised $[NP_{std}]$ =5 ml/L CE in agarose gel to avoid NP aggregation. We performed spatial sensitivity mapping of the RF coils on a saline phantom placed into the mouse holder and positioned at the intended imaging location. The imaging

parameters were: TR = 100 ms, TE = 1.96 ms, and flip angle = 10°. The phantom image provided a pre-determined correction factor $R(x, y, z)$, which was the inverse of the absolute signal, to normalize all *in vivo* measured ^{19}F signal intensities, which compensated for the effect of sensitivity profile inhomogeneity on received signal (39).

Immediately after *in vivo* ^{19}F imaging, blood was drawn from the left ventricle and the blood sample was placed beside the external standard for *ex vivo* ^{19}F imaging using a custom-built ^{19}F solenoid coil. The average signal intensity ratio between the blood sample and external standard offered a direct measurement of the CE NP concentration in the circulating blood $[NP_{blood}]$ (ml/L). The detailed scan parameters for *ex vivo* imaging were identical to the spin density weighted ^{19}F MRI *in vivo*.

By combining *ex vivo* calibration and *in vivo* ^{19}F MRI, we calculated the renal blood volume (% of voxel volume or tissue weight) in each imaging voxel based on the following equation:

$$RBV(x, y, z) = \frac{S_{long}(x, y, z) \times R(x, y, z) \times [NP_{std}]}{S_{long}(x_0, y_0, z_0) \times R(x_0, y_0, z_0) \times [NP_{blood}]}, \quad [1]$$

where $S_{long}(x, y, z)$ and $S_{long}(x_0, y_0, z_0)$ are the signal intensities at the kidney and the external standard in the ^{19}F spin density weighted images. $R(x, y, z)$ and $R(x_0, y_0, z_0)$ are the correction factors at the location of kidney and the external standard.

In vivo renal T1 quantification and pO_2 measurement were based on the fundamental assumption that image signal intensity in a fast spin echo sequence depends on TR and follows a saturation-recovery process:

$$S(TR) = S_0(1 - e^{-TR/T1}), \quad [2]$$

where S_0 is a TR-independent baseline parameter. Such a formalism is accurate to the first order when TE << TR in a fast spin echo sequence (40). In the present study, TR for spin density and T1-weighted images were 4 s and ~1 s respectively (or ~400 and ~100 times longer than TE = 11.5 ms, respectively). Therefore, Eq. [2] was applicable for approximating the signal intensity in renal ^{19}F images.

Because T1-weighed ^{19}F MRI was gated with respiration, the real TR might vary from animal to animal. Therefore, the real TR was determined retrospectively from the ratio of the signal intensities of the external standard in the spin density weighted ^{19}F MRI and T1-weighted ^{19}F MRI *in vivo*:

$$TR_{short} = -T1_{std} \times \ln\left(\frac{S_{short}(x_0, y_0, z_0)}{S_{long}(x_0, y_0, z_0)}\right), \qquad [3]$$

where $T1_{std}$ is the ^{19}F T1 in the external standard that is directly measured in vitro, $S_{short}(x_0, y_0, z_0)$ and $S_{long}(x_0, y_0, z_0)$ are the signal intensities of the external standard in T1-weighted and spin-density weighted ^{19}F MRI. Here we also accounted for the fact that in the spin density weighted image, TR > 4 s could be assumed to be sufficiently long that there was no T1 effect in this image because it was over 3 times longer than the normal ^{19}F T1 in kidneys. With real TR acquired from external standard, voxel-wise T1 mapping of the kidney could be calculated as

$$T1(x, y, z) = \frac{TR_{short}}{\ln(S_{long}(x, y, z)) - \ln(S_{short}(x, y, z))}. \qquad [4]$$

Finally, T1 values were translated into corresponding pO_2 levels according to the pre-determined calibration curve relating ^{19}F relaxation and oxygen tension.

6.2.4 Mouse acute kidney injury (AKI) model

C57/Bl mice (n=10) underwent laparotomy and a standard procedure to produce warm ischemia-reperfusion injury (41). Briefly, mice were anesthetized with ketamine/xylazine followed by a mid-line incision on the abdomen. After exposing the vasculature of the left kidney, we induced ischemia by ligating both renal artery and vein with a suture. Cessation of renal blood flow and restoration of perfusion after releasing the ligatures were confirmed visually by noting the color change of the kidneys. Mice with incomplete ischemia or reperfusion were excluded prospectively from the study. Ischemia was maintained for 60 minutes, during which mice were kept warm with a water-circulating blanket at 37°C. To avoid dehydration of exposed organs, warm saline was added to the abdominal cavity during ligation. 24 hours after surgery, both injured and contralateral kidneys were scanned with functional ^{19}F and BOLD MRI *in vivo* as described previously. After *in vivo* MRI, 10 μl FITC-lectin (Vector Laboratory, USA) was injected into the left ventricle and allowed to circulate for 5 minutes. Both kidneys were harvested and frozen in OCT media (Tissue-Trek, Japan) for fluorescence microscopic imaging and histological preparation.

6.2.5 Histology and fluorescence imaging

Frozen tissues were sectioned into 8 μm slices for histology and fluorescence imaging. Briefly, hematoxylin and eosin were used to stain kidneys to confirm tissue damage caused by ischemia-reperfusion. Fluorescence images were digitized with an Olympus BX61 fluorescent microscope after mounting with DAPI mount media (Vectashield Inc., USA). DAPI, Texas Red and FITC channels were selected to image the nucleus, CE NP, and perfused blood vessels respectively. All fluorescence images were color coded and co-registrated in IMAGEJ (NIH, USA).

6.2.6 Treatment evaluation for PPACK NPs in AKI

PPACK NPs was prepared using our previously described protocol to achieve an average loading of 13,650 PPACK on each particle. Animals were injected with PPACK NPs (N = 3) or plain NPs (N =3) at 15 minutes before experiencing 45 minutes ischemia (dose: 1 mL/Kg). At 3-hour after reperfusion, animals were euthanized and perfused with saline to washout blood-pool NPs in perfused vessel. Ev vivo spectroscopic quantification of retained NP concentration was performed using a standard single pulse ^{19}F spectroscopy sequence and a sample of 10 µl trifluoroacetic acid (TFA, 0.1% volume concentration) as external reference standard. *Ex vivo* ^{19}F spin density weighted imaging was also performed for all kidneys using the identical protocol as *in vivo* ^{19}F imaging as described earlier.

6.2.7 Data processing and statistics

All MRI images and signal analyses were processed with a custom-designed program written in Matlab (MathWorks, USA). Segmentation for different regions in healthy kidneys was performed manually based on ^{19}F spin density weighted and ^{1}H T2* weighted images. All statistical analyses were conducted in Origin (OriginLab, USA): paired t-tests and repeated measures ANOVA were used for hypothesis testing as indicated.

6.3 Results

6.3.1 ^{1}H and ^{19}F MRI of healthy kidneys

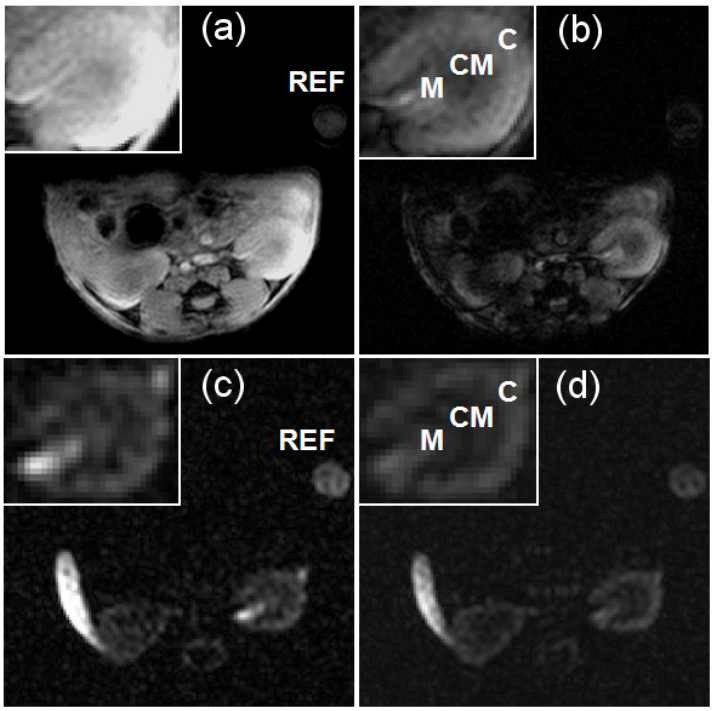

Figure 6.1 *In vivo* ^{1}H and ^{19}F images of healthy kidneys. (a & b) Representative T1-weighted and T2*-weighted ^{1}H MRI of mouse kidneys in the transverse plane. (c & d) Representative spin density weighted and T1-weighted ^{19}F MRI of mouse kidneys in the transverse plane. Slice planning is identical for ^{1}H and ^{19}F images and kidneys were zoomed in for better visualization. (C: cortex, CM: cortico-medullary junction, M: medulla, REF: external reference standard).

Representative ^{1}H T1-weighted, ^{1}H T2*-weighted, ^{19}F spin density weighted, and ^{19}F T1-weighted images are shown in Figure 6.1. Contrast between the renal cortex and medulla could be visualized in all images. The high rate of oxygen consumption under physiological conditions further reduced the signal intensity at the region of the cortico-medullary junction in ^{1}H T2*-weighted images. It is notable that the ^{1}H T2*-weighted image (i.e., BOLD) could not accurately depict the relative oxygenation at the renal medulla because most of the blood volume in this

region is contributed by large blood vessels, which do not create a detectable field inhomogeneity at the microscopic level, a necessary condition for BOLD signal imaging (42-43). ^{19}F spin density weighted images directly represented the relative perfusion within different regions of the kidneys. Specifically, ^{19}F signal intensity decreased from the cortex to the cortico-medullary junction and increased again at the medulla. In the inner portion of kidney where both medullary microvasculature and major renal artery/vein are present, relatively higher ^{19}F signal was detected that correlated directly with local blood concentration. Finally, in ^{19}F T1-weighted images, ^{19}F signal intensity throughout the entire kidney was affected by the incomplete magnetization recovery. However, it is evident that the signal intensity at the renal medulla was further suppressed because of the lower oxygenation and longer ^{19}F T1 in this region.

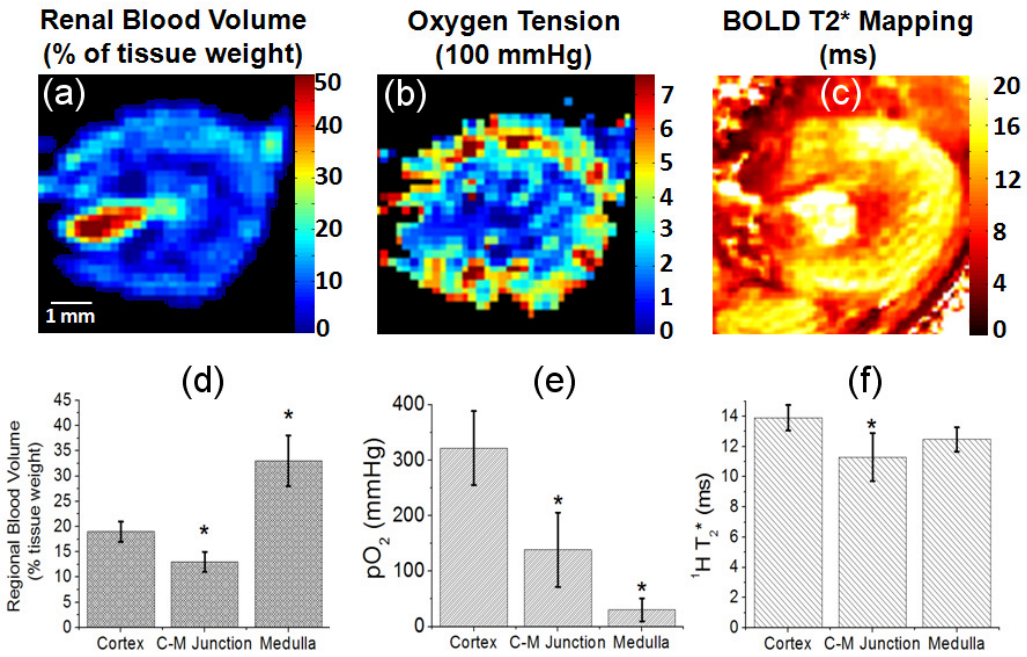

Figure 6.2 ^{19}F MRI determined functional mapping and quantification in healthy kidneys. (a-b) Representative quantitative renal blood volume and oxygen tension mapping generated from ^{19}F MRI of healthy kidneys. (c) Representative ^{1}H T2* mapping of healthy kidneys. (d-f)

Quantification of functional indexes in different anatomical regions. Data are presented as mean ± std. (C-M: cortico-medullary, *: $p<0.05$).

6.3.2 Quantitative blood volume and oxygenation mapping in healthy kidneys

Heterogeneous distribution of renal blood volume and intrarenal oxygenation was confirmed in the quantitative parametric mapping of ^{1}H T2*, RBV and pO_2 as illustrated in Figure 6.2 (a-c). Absolute quantification of these functional indexes in different regions of kidneys is summarized in Figure 6.2 (d-f). Specifically, with ^{1}H BOLD MRI, both the renal cortex and medulla exhibited significantly longer ^{1}H T2*, suggesting higher tissue oxygenation, than did the cortico-medullary junction. This inaccurate BOLD readout of high oxygenation in the hypoxic inner medulla has previously been recognized as a technical limitations of BOLD MRI in the kidney (43).

^{19}F MRI of renal blood volume revealed inhomogeneous blood supply to different anatomical regions of the kidney. To wit, the measured renal blood volumes (in units of volume fraction per voxel or tissue weight) were: 19 ± 2 % in the cortex, 13 ± 2 % in the cortico-medullary junction and 33 ± 5% in the medulla, respectively ($p<0.05$, for all different regions). The vascular pattern detected with ^{19}F MRI is consistent with previous studies that have employed *ex vivo* micro CT (44). With the use of the measured *ex vivo* calibration curve relating ^{19}F R1 and oxygen tension:

$$R1(s^{-1}) = 0.0032 \times pO_2(mmHg) + 0.72, \qquad [5]$$

oxygen tension mappings were acquired under conditions of ventilation with pure oxygen. The cortical pO_2 (361± 67 mmHg) was significantly higher than that in the cortico-medullary junction (138 ± 66 mmHg) or medulla (30 ± 20 mmHg) ($p<0.05$, for comparison among all three regions).

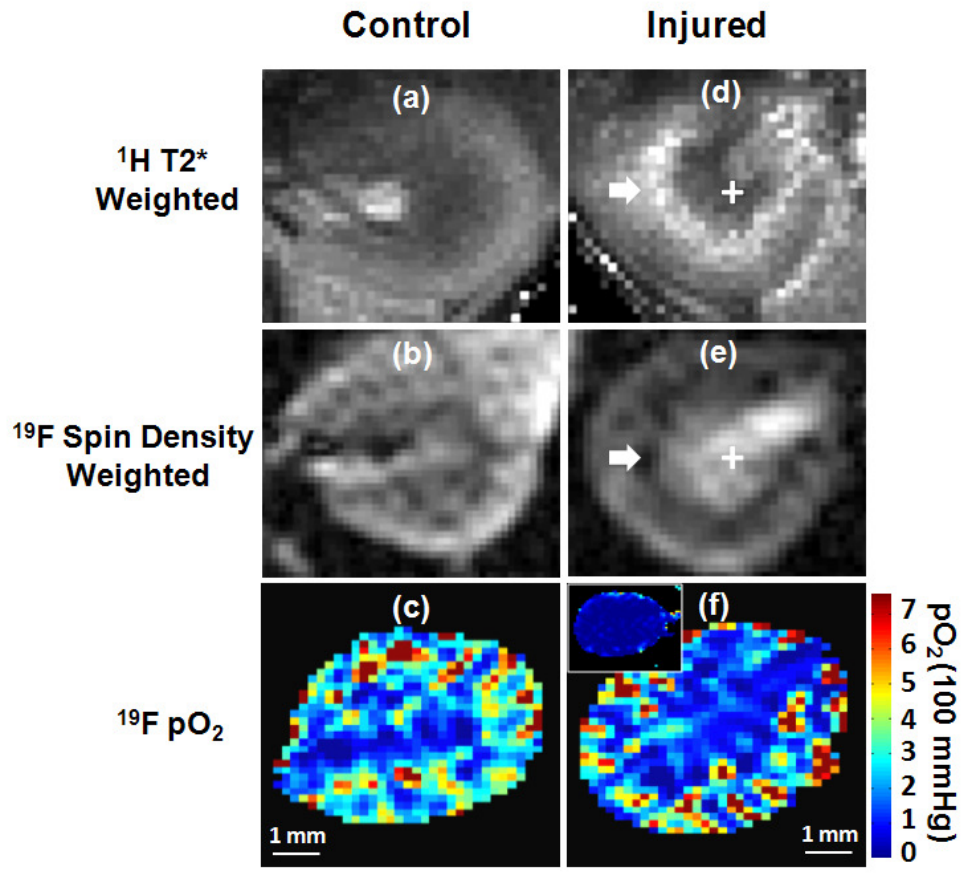

Figure 6.3 Representative ^{1}H T2*-weighted image, ^{19}F spin density weighted image and pO_2 mapping in contralateral and injured kidneys. The inserted panel in (f) represents the ^{19}F oxygenation mapping during ischemia. White arrow points to the cortico-medullary junction and the white cross identifies the renal medulla.

6.3.3 ^{1}H and ^{19}F MRI of kidneys after ischemia-reperfusion AKI

Figure 6.3 shows representative ^{1}H T2*-weighted images,^{19}F spin density weighted images and ^{19}F pO_2 mapping of injured and contralateral kidneys. At 24 hours after ischemia-reperfusion, ^{19}F MRI revealed a complete recovery of ^{19}F signal intensity (reflecting restoration of blood volume), pO_2 and ^{1}H T2* in the cortex region of injured kidneys (Figure 6.4a-c). In the cortico-medullary junction of injured kidneys, ^{19}F signal intensity decreased approximately 25% ($p < 0.05$) and ^{1}H T2* increased approximately 70% ($p<0.01$), which is likely a consequence of

edema and thrombosis (Figure 6.4a&c). In the renal medulla region, ^{19}F and BOLD MRI detected 71% higher ^{19}F signal intensity ($p<0.01$) and 40% lower ^{1}H T2* value ($p<0.05$) in the injured kidneys as compared with contralateral kidneys, which may be associated with vascular leakage and hemorrhage-induced intrarenal retention of PFC NPs (Figure 6.4a&c). As for the intrarenal oxygenation defect, even though we did observe complete desaturation during ischemia (Figure 6.3f, insert), at 24 hours after transient ischemia-reperfusion, ^{19}F MRI revealed that intrarenal oxygenation had recovered to normal level (Figure 6.4b).

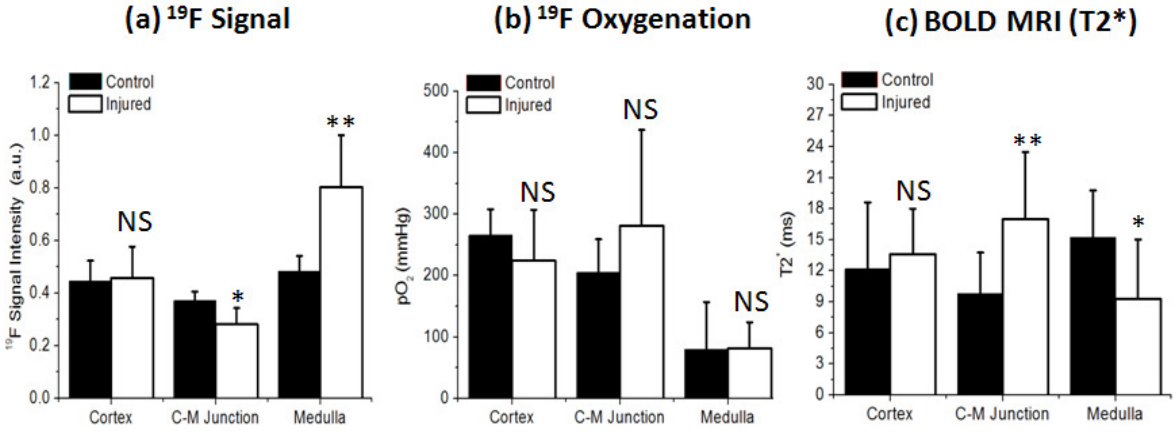

Figure 6.4 Absolute quantification of ^{19}F signal intensity (a), pO_2 (b) and ^{1}H T2* (c) in different anatomical regions of both contralateral and injured kidneys at 24 hours after injury. Data are presented as mean ± std. (*: $p<0.05$ and **: $p<0.01$).

6.3.4 Histology and fluorescence image

Endothelial staining with FITC-lectin demonstrated the reduced perfused micro-blood vessel density at the cortico-medullary junction (Figure 6.5a). Fluorescence microscopy of PFC NP confirmed the accumulation of PFC NP within the renal medulla in comparison to the uninjured contralateral kidneys (Figure 6.5b). By co-registering the FITC-lectin endothelial staining with the fluorescent PFC NP (Figure 6.5c), we observed that PFC NP accumulated within extravascular spaces in injured kidneys, suggesting that the high PFC NP concentration at

the renal medulla could be attributed to the vascular leakage expected under conditions of severe endothelial injury. H&E staining revealed extensive tissue damage and necrosis at the cortico-medullary junction and in the medulla regions of injured kidneys (Figure 6).

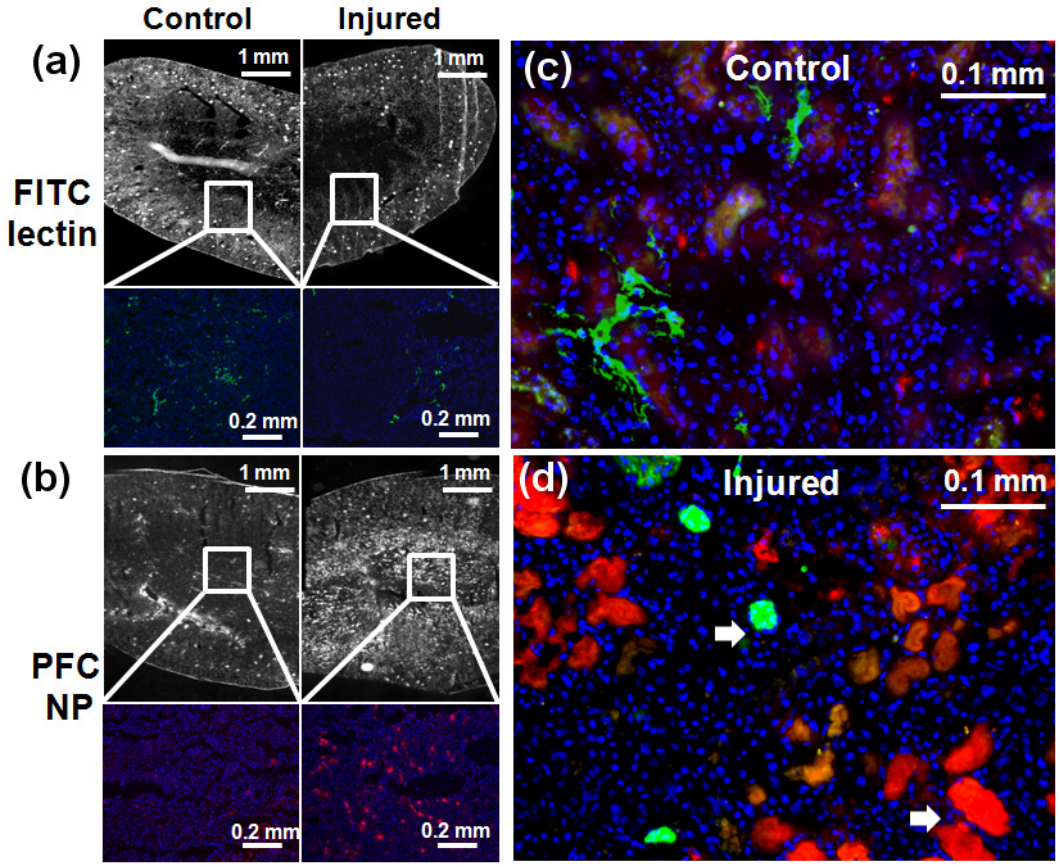

Figure 6.5 Fluorescence image of injured and contralateral kidneys. (a) Top row: overview fluorescence image of FITC-lectin for visualizing perfused blood vessels in contralateral and injured kidneys. Bottom row: zoomed-in view of FITC-lectin fluorescence image in the cortico-medullary junction. (b) Top row: overview fluorescence image of PFC NP in contralateral and injured kidneys. Bottom row: zoomed-in view of PFC NP fluorescence image in the renal medulla. (c & d) Merged FITC-lectin and PFC NP fluorescence image of renal medulla confirmed that PFC NP leaked out from blood vessels and accumulated in the extravascular

space of injured kidneys as indicated by white arrows. (Red: PFC NP, Blue: DAPI, Green: FITC-lectin).

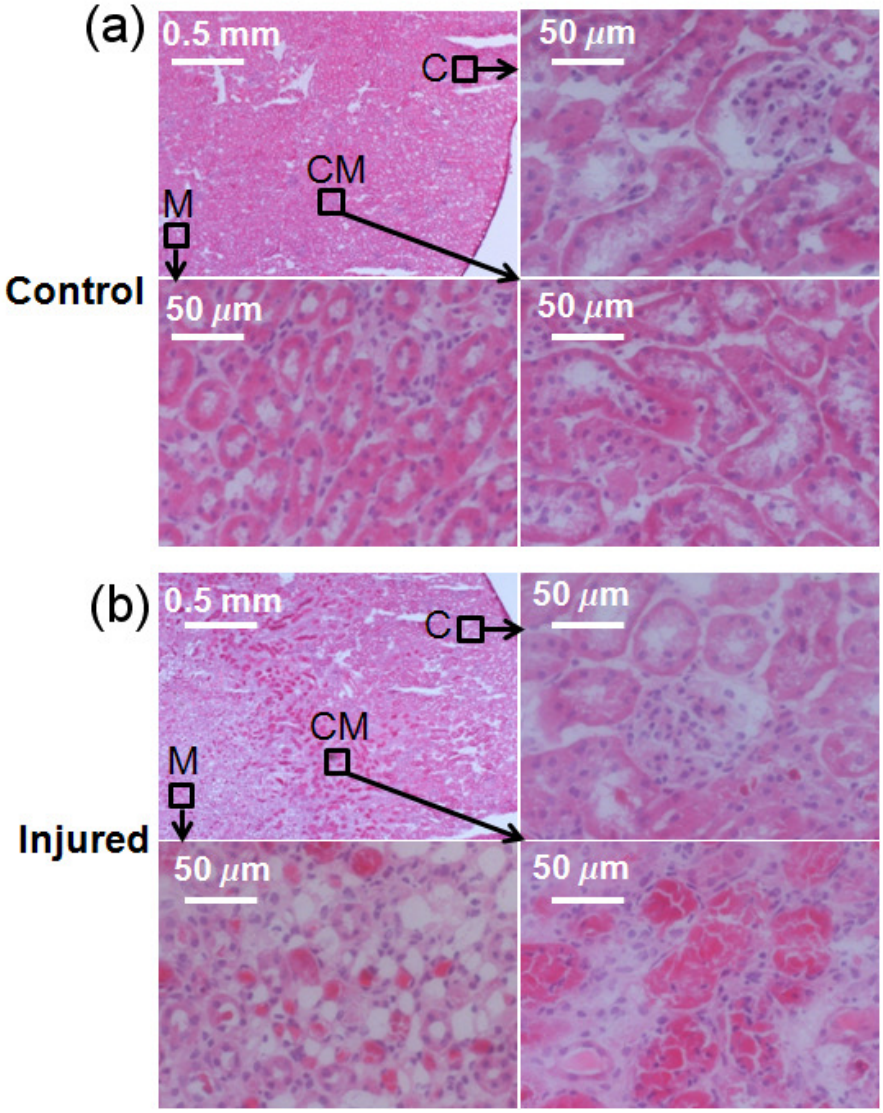

Figure 6.6 H&E staining of contralateral and injured kidneys. In both sub-figures, the top left panel is an overview of the kidney tissue and the other three panels are the high resolution pictures in different anatomical regions as indicated by dark arrows. H&E staining revealed extensive tissue damage and necrosis in the cortico-medullary junction and in the medulla (C: cortex, CM: cortico-medullary junction, M: medulla).

6.3.5 Treatment effect of PPACK NPs evaluated with 19F MRI

At 3-hour after reperfusion, composite $^{1}H/^{19}F$ images (Figure 6.7a&b) showed less ^{19}F signal (color coded) emanating from trapped NPs in an injured kidney treated with therapeutic PPACK PFC NPs versus an injured kidney treated with plain PFC NPs (mostly concentrated at the renal medulla region). ^{19}F spectroscopic quantification (Figure 6.7c) confirmed a higher number of trapped blood pool NPs, reflecting intrarenal coagulation, in I/R injured kidneys than that in contralateral uninjured kidneys of the same mice. Among I/R injured kidneys, however, substantially fewer NPs were detected in those treated with PPACK NPs reflecting its positive effect on inhibiting intrarenal coagulation.

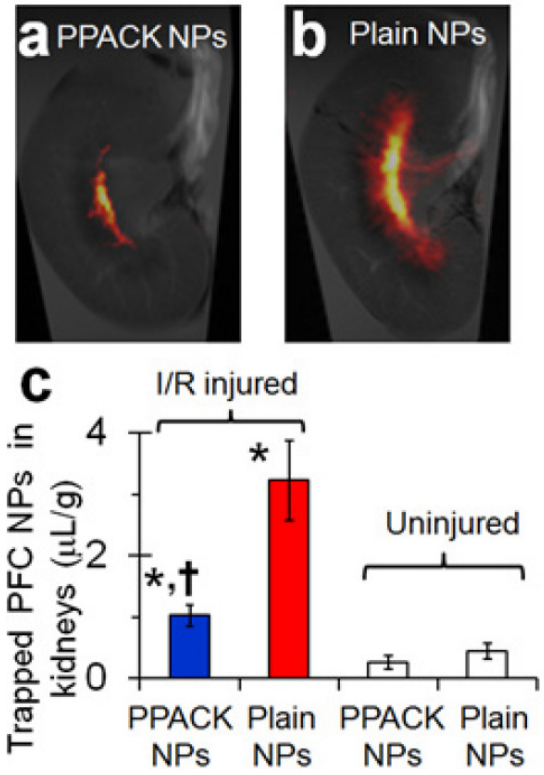

Figure 6.7 Ev vivo ^{19}F image and quantification for retained PFC NP in ischemia-reperfusion injured kidneys with PPACK NPs and plain NPs pre-treatment. *, $p<0.05$ compared to contralateral uninjured kidneys; †, $p< 0.05$ compared to plain NP treated kidneys.

6.4 Discussion

Renal endothelial damage is a primary pathology of AKI. It leads to persistent inflammation and coagulation that hampers effective oxygen delivery, resulting in sustained injury to tubular cells even after the resumption of renal blood flow in the "extension phase" of AKI (45). The extent of non-perfusion is more severe in the renal medulla and cortico-medullary junction than in the cortex (33,46-47). Unfortunately, the interplay between inflammation and coagulation in AKI remains incompletely understood, due in part to the lack of appropriate multiparametric approaches for accurate staging of the disease process *in vivo* that might contribute to more accurate risk assessment and prognostication (48).

To that end, in the present study we have developed a new ^{19}F MRI approach for functional kidney imaging that takes advantage of the quantifiable properties of circulating PFC NP. As an initial proof of concept, we have demonstrated the feasibility of combining spin density weighted and T1-weighted ^{19}F images of circulating PFC NP for quantification of renal blood volume and oxygenation. We further demonstrated that by integrating parametric mappings generated from ^{19}F MRI and conventional BOLD MRI, a more comprehensive diagnostic matrix for evaluating renal function and physiology is possible. The diagnostic capability of the proposed multi-function imaging method was evaluated in an experimental renal ischemia-reperfusion model of AKI. In this animal model, ^{19}F MRI clearly delineated the anticipated medullary vascular leakage as a pathophysiological consequence of severe endothelial damage. Moreover, ^{19}F MRI successfully defined the expected reduced blood volume at the cortico-medullary junction, indicating vessel occlusion as evidenced by lower density of perfused blood vessels detected with fluorescence imaging. Finally, the reduced blood volume

was associated with increased regional ^{1}H T2* in the cortico-medullary junction as revealed by BOLD MRI.

These clinically translatable renal imaging techniques should expand the armamentarium for functional renal imaging in patients with existing or new onset kidney disease. The use of traditional functional imaging schemes, such as iodine contrast based CT and Gd based MRI, are significantly restricted in patients with renal insufficiency (11). Indeed, the use of such contrast media accounts for 10% of hospital acquired renal failure in the United States (13,20). Circulating PFC NP may offer a safer contrast agent for functional kidney imaging for several reasons. Firstly, PFC NP has been clinically approved as a blood substitute for decades, and to date no renal toxicity has been reported, owing in part to clearance through liver and lung portals instead of renal filtration. Therefore, intravenous PFC NPs are not expected to exert additional toxic strain on kidneys. Secondly, the unique ^{19}F signal emanating from the PFC moieties in the core of the nanoparticle can be detected readily with ^{19}F MRI. As compared to other imaging nuclei, ^{19}F exhibits a high gyromagnetic ratio, and generates comparable magnetization to ^{1}H nuclei in an external magnetic field. We anticipate that fully optimized imaging protocols would enable the entire procedure of ^{19}F functional kidney imaging to be conducted within a clinically relevant time frame (<30 minutes in the present study). Thirdly, non-invasive estimates of intrarenal oxygen tension can be derived from ^{19}F R1, because ^{19}F R1 is linearly responsive to local oxygen tension over a wide range of values, and the oxygen exchange between blood and PFC occurs by free diffusion on a millisecond time scale (49).

Our non-invasive measurement of renal blood volume and oxygenation is consistent with previously reported ex-vivo (44) and invasive measurements (6,50-52). Accurate delineation of the distribution of renal blood volume and intrarenal oxygenation is important because of its

unique pattern and pathophysiological implications. In healthy kidneys, both the renal artery and vein branch into smaller blood vessels to perfuse the renal cortex, which is critical for maintaining a physiological glomerular filtration rate (GFR). It is notable that only a small portion of renal blood flow supports the capillary beds of the collecting ducts at the cortico-medullary junction and medulla. Despite this marginal blood supply, the epithelial cells of the collecting duct still must function at a high metabolic level to support the functioning of various ion channels for urine concentration, and thus must operate at the hypoxic margin even under physiological conditions, as evidenced by the steep oxygenation gradient from renal cortex to medulla. Accordingly, the use of noninvasive ^{19}F MRI to depict the inhomogeneous blood volume distribution and oxygenation gradient within the kidney could serve as a translational tool for future studies of renal pathophysiology in AKI.

We utilized the mouse ischemia-reperfusion AKI model for evaluating the proposed^{19}F functional kidney MRI techniques because endothelial damage of the renal micro-circulation is a key component in this model. Extensive interaction between inflammation and coagulation takes place in AKI (33) and the endothelial damage elicits persistent tubular epithelial dysfunction even after reperfusion (46), which mimics human pathophysiology. Because of the unique vascular geometry found in the kidney, coagulation is most severe at the cortico-medullary junction and the medulla region (53). Persistent ischemia here will disturb normal fluid filtration and re-absorption, leading to worsening renal dysfunction and/or failure (54). Our ^{19}F MRI results together with histological assessment and BOLD MRI confirmed the micro blood vessel non-perfusion in this region. Additionally, it has been observed that acute ischemic/hypoxic injury disrupts the normal blood vessel barrier, resulting in intrarenal hemorrhage and vascular leakage (55). PFC NPs, with a size of 250 nm, under normal circumstances function mostly as an

intravascular agent that does not permeate the physiological vascular barrier. However, in injured kidneys, a substantial accumulation of PFC NP was observed within the renal medulla in extravascular spaces as a consequence of severe endothelial damage. The comprehensive functional evaluation with ^{19}F MRI, BOLD, and fluorescence imaging offers an alternative approach for examining vascular barrier disruption *in vivo*, as we have shown previously for advanced atherosclerosis (56). This technique exhibits practical translational advantages over conventional optical imaging (e.g., Evans blue dye) that is not clinically utile (55). Finally, the measured improvement of renal oxygenation imaged after 24 hours of reperfusion in this model indicates potential utility for following kidney damage after AKI and quantifying its responses to therapeutic interventions.

Although PPACK is a potent thrombin-inhibitor with an excellent safety profile (LD50 > 50 mg/Kg), it has little *in vivo* effect because of the short elimination half-life (~3 minutes) (57). Conjugating PPACK to PFC NPs extended the drug elimination half-life to several hours. In addition, the deposited PPACK NPs on the clot surface manifested prolonged anticoagulation activity even after the systematic effect was diminished (37). Here we demonstrated PPACK PFC NPs effectively inhibit coagulation in AKI in small quantities, as evidenced by lesser accumulation of particles trapped by the clotting process, which suggests a new strategy for treating and evaluating kidney endothelial damage with thrombin targeted ^{19}F MRI.

With respect to limitations of ^{19}F functional renal imaging, because PFC NP that generate the ^{19}F signal for MRI are present in circulating blood, certain flow effects could distort the quantitative readout of perfusion metrics. Also, at higher field strengths, paramagnetic deoxygenated hemoglobin generates strong local field inhomogeneities that could significantly reduce the signal to noise ratio of ^{19}F MRI in the kidney. To mitigate this effect, quantitative

mapping of renal blood volume and oxygenation were performed only when mice were breathing pure oxygen. Further modifications of the imaging pulse sequences might be considered in the future to enable functional ^{19}F kidney MRI under normoxic conditions. Finally, the limited temporal resolution of ^{19}F MRI currently poses an obstacle for capturing the first pass of the contrast agent through the renal circulation. Therefore, certain dynamic parameters such as transient time and renal blood flow rate cannot be determined from these ^{19}F MRI measurements. Again, optimizations in pulse sequence and RF coil design and performance could ultimately enhance detection sensitivity and enable applications that require higher temporal resolution.

6.5 References

1. O'Connor PM. Renal oxygen delivery: matching delivery to metabolic demand. Clin Exp Pharmacol Physiol 2006;33(10):961-967.
2. Evans RG, Gardiner BS, Smith DW, O'Connor PM. Intrarenal oxygenation: unique challenges and the biophysical basis of homeostasis. Am J Physiol Renal Physiol 2008;295(5):F1259-1270.
3. Mattson DL. Importance of the renal medullary circulation in the control of sodium excretion and blood pressure. Am J Physiol Regul Integr Comp Physiol 2003;284(1):R13-27.
4. Sutton TA, Fisher CJ, Molitoris BA. Microvascular endothelial injury and dysfunction during ischemic acute renal failure. Kidney Int 2002;62(5):1539-1549.
5. Safian RD, Textor SC. Renal-artery stenosis. N Engl J Med 2001;344(6):431-442.
6. Brezis M, Rosen S. Hypoxia of the renal medulla--its implications for disease. N Engl J Med 1995;332(10):647-655.

7. Kalantarinia K. Novel imaging techniques in acute kidney injury. Curr Drug Targets 2009;10(12):1184-1189.

8. Prasad PV. Functional MRI of the kidney: tools for translational studies of pathophysiology of renal disease. Am J Physiol Renal Physiol 2006;290(5):F958-974.

9. Tsushima Y. Functional CT of the kidney. Eur J Radiol 1999;30(3):191-197.

10. Aparicio LS, Boggio GF, Waisman GD, Romero JC. Advances in noninvasive methods for functional evaluation of renovascular disease. J Am Soc Hypertens 2009;3(1):42-51.

11. Gleeson TG, Bulugahapitiya S. Contrast-induced nephropathy. AJR Am J Roentgenol 2004;183(6):1673-1689.

12. Wong PC, Li Z, Guo J, Zhang A. Pathophysiology of contrast-induced nephropathy. Int J Cardiol 2012;158(2):186-192.

13. Briguori C, Visconti G, Focaccio A, Airoldi F, Valgimigli M, Sangiorgi GM, Golia B, Ricciardelli B, Condorelli G. Renal Insufficiency After Contrast Media Administration Trial II (REMEDIAL II): RenalGuard System in high-risk patients for contrast-induced acute kidney injury. Circulation 2011;124(11):1260-1269.

14. Briguori C, Marenzi G. Contrast-induced nephropathy: pharmacological prophylaxis. Kidney Int Suppl 2006(100):S30-38.

15. Sadowski EA, Bennett LK, Chan MR, Wentland AL, Garrett AL, Garrett RW, Djamali A. Nephrogenic systemic fibrosis: risk factors and incidence estimation. Radiology 2007;243(1):148-157.

16. Boyd AS, Zic JA, Abraham JL. Gadolinium deposition in nephrogenic fibrosing dermopathy. J Am Acad Dermatol 2007;56(1):27-30.

17. Ries M, Basseau F, Tyndal B, Jones R, Deminiere C, Catargi B, Combe C, Moonen CW, Grenier N. Renal diffusion and BOLD MRI in experimental diabetic nephropathy. Blood oxygen level-dependent. J Magn Reson Imaging 2003;17(1):104-113.

18. Grenier N, Basseau F, Ries M, Tyndal B, Jones R, Moonen C. Functional MRI of the kidney. Abdom Imaging 2003;28(2):164-175.

19. Maril N, Rosen Y, Reynolds GH, Ivanishev A, Ngo L, Lenkinski RE. Sodium MRI of the human kidney at 3 tesla. Magnetic Resonance in Medicine 2006;56(6):1229-1234.

20. Prasad PV, Edelman RR, Epstein FH. Noninvasive evaluation of intrarenal oxygenation with BOLD MRI. Circulation 1996;94(12):3271-3275.

21. Detre JA, Zhang WG, Roberts DA, Silva AC, Williams DS, Grandis DJ, Koretsky AP, Leigh JS. TISSUE-SPECIFIC PERFUSION IMAGING USING ARTERIAL SPIN-LABELING. Nmr in Biomedicine 1994;7(1-2):75-82.

22. Wu WC, Su MY, Chang CC, Tseng WY, Liu KL. Renal perfusion 3-T MR imaging: a comparative study of arterial spin labeling and dynamic contrast-enhanced techniques. Radiology 2011;261(3):845-853.

23. Chandarana H, Lee VS. Renal Functional MRI: Are We Ready for Clinical Application? American Journal of Roentgenology 2009;192(6):1550-1557.

24. Evans RG, Leong CL, Anderson WP, O'Connor PM. Don't be so BOLD: Potential limitations in the use of BOLD MRI for studies of renal oxygenation. Kidney Int 2007;71(12):1327-1328.

25. Mason RP, Nunnally RL, Antich PP. Tissue oxygenation: a novel determination using 19F surface coil NMR spectroscopy of sequestered perfluorocarbon emulsion. Magn Reson Med 1991;18(1):71-79.

26. Wickline SA, Mason RP, Caruthers SD, Chen J, Winter PM, Hughes MS, Lanza GM. Fluorocarbon agents for multimodal molecular imaging and targeted therapeutics. In: Weissleder R, Ross BD, Rehemtulla A, Gambhir SS, editors. Molecular imaging: Principles and practice: Peoples Medical Publishing House-USA; 2010. p 542-573.

27. Spahn DR. Blood substitutes. Artificial oxygen carriers: perfluorocarbon emulsions. Crit Care 1999;3(5):R93-97.

28. Cohn CS, Cushing MM. Oxygen therapeutics: perfluorocarbons and blood substitute safety. Crit Care Clin 2009;25(2):399-414, Table of Contents.

29. Partlow KC, Chen J, Brant JA, Neubauer AM, Meyerrose TE, Creer MH, Nolta JA, Caruthers SD, Lanza GM, Wickline SA. 19F magnetic resonance imaging for stem/progenitor cell tracking with multiple unique perfluorocarbon nanobeacons. FASEB J 2007;21(8):1647-1654.

30. Neubauer AM, Caruthers SD, Hockett FD, Cyrus T, Robertson JD, Allen JS, Williams TD, Fuhrhop RW, Lanza GM, Wickline SA. Fluorine cardiovascular magnetic resonance angiography in vivo at 1.5 T with perfluorocarbon nanoparticle contrast agents. J Cardiovasc Magn Reson 2007;9(3):565-573.

31. Rottman GA, Judd RM, Yin FC. Validation of 19F-magnetic resonance determination of myocardial blood volume. Magn Reson Med 1995;34(4):628-631.

32. Mason RP. Non-invasive physiology: 19F NMR of perfluorocarbons. Artif Cells Blood Substit Immobil Biotechnol 1994;22(4):1141-1153.

33. Basile DP. The endothelial cell in ischemic acute kidney injury: implications for acute and chronic function. Kidney Int 2007;72(2):151-156.

34. Esmon CT. Role of coagulation inhibitors in inflammation. Thromb Haemost 2001;86(1):51-56.

35. Petaja J. Inflammation and coagulation. An overview. Thromb Res 2011;127 Suppl 2:S34-37.

36. Hanson SR, Harker LA. Interruption of acute platelet-dependent thrombosis by the synthetic antithrombin D-phenylalanyl-L-prolyl-L-arginyl chloromethyl ketone. Proc Natl Acad Sci U S A 1988;85(9):3184-3188.

37. Myerson J, He L, Lanza G, Tollefsen D, Wickline S. Thrombin-inhibiting perfluorocarbon nanoparticles provide a novel strategy for the treatment and magnetic resonance imaging of acute thrombosis. J Thromb Haemost 2011;9(7):1292-1300.

38. Paller MS, Murray BM. Renal dysfunction in animal models of cyclosporine toxicity. Transplant Proc 1985;17(4 Suppl 1):155-159.

39. Wijnen JP, van der Kemp WJ, Luttje MP, Korteweg MA, Luijten PR, Klomp DW. Quantitative (31) P magnetic resonance spectroscopy of the human breast at 7 T. Magn Reson Med 2012;68(2):339-348.

40. Meara SJ, Barker GJ. Evolution of the longitudinal magnetization for pulse sequences using a fast spin-echo readout: application to fluid-attenuated inversion-recovery and double inversion-recovery sequences. Magn Reson Med 2005;54(1):241-245.

41. Oostendorp M, de Vries EE, Slenter JM, Peutz-Kootstra CJ, Snoeijs MG, Post MJ, van Heurn LW, Backes WH. MRI of renal oxygenation and function after normothermic ischemia-reperfusion injury. NMR Biomed 2011;24(2):194-200.

42. He X, Yablonskiy DA. Quantitative BOLD: mapping of human cerebral deoxygenated blood volume and oxygen extraction fraction: default state. Magn Reson Med 2007;57(1):115-126.

43. Prasad PV. Evaluation of intra-renal oxygenation by BOLD MRI. Nephron Clin Pract 2006;103(2):c58-65.

44. Bentley MD, Ortiz MC, Ritman EL, Romero JC. The use of microcomputed tomography to study microvasculature in small rodents. Am J Physiol Regul Integr Comp Physiol 2002;282(5):R1267-1279.

45. Molitoris BA, Sutton TA. Endothelial injury and dysfunction: role in the extension phase of acute renal failure. Kidney Int 2004;66(2):496-499.

46. Basile DP, Donohoe D, Roethe K, Osborn JL. Renal ischemic injury results in permanent damage to peritubular capillaries and influences long-term function. Am J Physiol Renal Physiol 2001;281(5):F887-899.

47. Lameire NH, Vanholder R. Pathophysiology of ischaemic acute renal failure. Best Pract Res Clin Anaesthesiol 2004;18(1):21-36.

48. Bonventre JV. Pathophysiology of AKI: injury and normal and abnormal repair. Contrib Nephrol 2010;165:9-17.

49. O'Brien RN, Langlais AJ, Seufert WD. Diffusion coefficients of respiratory gases in a perfluorocarbon liquid. Science 1982;217(4555):153-155.

50. Welch WJ, Baumgartl H, Lubbers D, Wilcox CS. Nephron pO2 and renal oxygen usage in the hypertensive rat kidney. Kidney Int 2001;59(1):230-237.

51. Evans RG, Gardiner BS, Smith DW, O'Connor PM. Methods for studying the physiology of kidney oxygenation. Clin Exp Pharmacol Physiol 2008;35(12):1405-1412.

52. Leong CL, O'Connor PM, Eppel GA, Anderson WP, Evans RG. Measurement of renal tissue oxygen tension: systematic differences between fluorescence optode and microelectrode recordings in anaesthetized rabbits. Nephron Physiol 2008;108(2):p11-17.

53. Mason J, Torhorst J, Welsch J. Role of the medullary perfusion defect in the pathogenesis of ischemic renal failure. Kidney Int 1984;26(3):283-293.

54. Devarajan P. Update on mechanisms of ischemic acute kidney injury. J Am Soc Nephrol 2006;17(6):1503-1520.

55. Mizutani A, Okajima K, Uchiba M, Isobe H, Harada N, Mizutani S, Noguchi T. Antithrombin reduces ischemia/reperfusion-induced renal injury in rats by inhibiting leukocyte activation through promotion of prostacyclin production. Blood 2003;101(8):3029-3036.

56. Zhang H, Zhang L, Myerson J, Bibee K, Scott M, Allen J, Sicard G, Lanza G, Wickline S. Quantifying the evolution of vascular barrier disruption in advanced atherosclerosis with semipermeant nanoparticle contrast agents. PLoS One 2011;6(10):e26385.

57. Van Aken H, Bode C, Darius H, Diehm C, Encke A, Gulba DC, Haas S, Hacke W, Puhl W, Quante M, Riess H, Scharf R, Schellong S, Schror T, Schulte KL, Tebbe U. Anticoagulation: the present and future. Clin Appl Thromb Hemost 2001;7(3):195-204.

7 Conclusion

In this dissertation, we first revisited the general background of molecular and functional imaging via MRI with a special focus on ^{19}F MRI of PFC NP based contrast agents. We performed a thorough examination, both theoretically and experimentally, of the NMR/MRI properties of PFC NP, including chemical shifts, J-coupling and J-modulation, oxygenation and paramagnetic relaxation enhancement of ^{19}F nuclear spins through their interaction with Gd chelates. Regarding the fundamental MR engineering for *in vivo* ^{19}F MRI of PFC NP, we developed a generalized strategy for designing ^{1}H/^{19}F dual frequency RF coils, which laid the groundwork for subsequent ^{19}F MR pulse sequence development and preclinical applications. Based on an understanding of the NMR physics of ^{19}F MRI of PFC NP, we developed two novel functional imaging techniques for: (1) noninvasive measurement of the oxygenation of flowing blood; and (2) multi-parametric functional imaging for evaluating the renal microcirculation and its pathological changes in standard models of acute renal ischemic injury.

7.1 Summary of major findings

In Chapter 2, we used the coupled-resonator model to develop a single-input dual frequency strategy for building birdcage and saddle coils that function at both ^{1}H and ^{19}F frequencies on a 4.7 T MRI scanner. The excellent matching properties and the homogeneity of B1 field were confirmed by S11 and S21 test measurements and by *in vivo* imaging in the C57BL/6 mouse. To enhance sensitivity, we integrated an actively decoupled surface coil with the dual frequency volume coils and increased the local SNR by 10 fold. As the structure of the volume coil was preserved, the sensitivity profile of the new dual frequency RF coils was essentially identical at ^{1}H and ^{19}F resonant frequencies.

In Chapter 3, we calculated the relationship between J-modulation of a representative PFC molecule (PFOB) and the imaging RF pulse bandwidth. Density matrix and experimental analyses suggested that narrow band RF pulses could suppress the J-modulation in ^{19}F spin echo imaging. By employing Bloch equation modeling, we also simulated the oxygenation effect on ^{19}F quantification. We showed that absolute quantification of the ^{19}F MR signals from PFC NP is insensitive to the oxygen concentration as long as TR> 3* T1, and moreover that shorter TE always facilitate the achievement of greater ^{19}F sensitivities even in the presence of the J-coupling effect. In the end, we took advantage of the multiple and widely separated chemical shifts of PFC NP to implement a "multi-chromatic" ^{19}F MRI technique that is capable of imaging at least five different PFC components in the same phantom using ultra narrow band RF pulses. The feasibility of "multi-chromatic" ^{19}F was demonstrated in vitro in cellular imaging studies and *in vivo* with ^{19}F MRI of a mouse leg.

In Chapter 4, we demonstrated that the ^{19}F signal strength emanating from PFC NP could be enhanced by incorporating a large number of paramagnetic moieties (Gd) into a monolayer lipid membrane surrounding a ^{19}F core. Our results showed that ^{19}F T1 shortening can be attributed to the Brownian motion of core PFC molecules inside the NP. An explicit expression for the relaxation enhancement was derived to describe the physical mechanisms that lead to enhanced longitudinal relaxation of ^{19}F nuclear spins. The theoretical description was confirmed experimentally by field-dependent T_1 measurements. The interaction between ^{19}F nuclear spins and Gd electron spins was observed to be highly dependent on the separation distance between them, which results in a "relaxation switch" phenomenon, which could be used to detect cellular processing of the contrast agent by macrophage endosomal activation. Specifically, after paramagnetic PFC NP was internalized by macrophages through endocytosis, endosomal

processing stripped the lipid surfactant layer containing the Gd away from the PFC core, resulting in the separation of ^{19}F and Gd atoms beyond the point where the Gd could exert an outer sphere influence on ^{19}F relaxation, leading rapidly to complete elimination of the exogenous relaxation enhancement of ^{19}F T1.

In Chapter 5, we developed a novel Blood flow-Enhanced-Saturation-Recovery (BESR) sequence, which allowed rapid *in vivo* T1 measurement of blood for both ^{1}H and ^{19}F nuclei. BESR sequence was achieved by combining homogeneous spin preparation and time-of-flight image acquisition, which served to preserve both efficient imaging and SNR for ^{19}F imaging of circulating PFC NP. The consistency and accuracy of the BESR sequence for measuring T1 of blood was validated experimentally. After confirming the linear response of ^{19}F R1 to increasing oxygen tension in both salt solutions and blood samples in vitro, we demonstrated the utility of the BESR sequence for quantification of oxygen tension within the mouse left and right ventricles under both normoxic and hyperoxic conditions.

In Chapter 6, we developed a unique sensor-reporter approach for functional kidney imaging that employs circulating PFC NP and ^{19}F MRI. Our noninvasive *in vivo* ^{19}F MRI technique generated quantitative readouts of renal blood volume and intrarenal oxygenation to describe the renal circulation in healthy mouse kidneys. In a mouse model of acute kidney injury (AKI, warm ischemia-reperfusion), we sensitively delineated renal vascular damage and recovery with the use of the proposed ^{19}F functional MRI strategy, in conjunction with ^{1}H Blood-Oxygenation-Level-Dependant (BOLD) MRI. In the cortico-medullary junction region, we reported a 25% lower 19F signal ($p<0.05$) and 70% longer 1H T2* ($p<0.01$) in injured kidneys as compared with the contralateral kidneys by 24 hours after initial ischemia-reperfusion injury. We also detected 71% greater ^{19}F signal ($p<0.01$) and 40% lower ^{1}H T2* ($p<0.05$) in the renal

medulla region of injured kidneys compared to contralateral kidneys. Moreover, with the use of *ex vivo* ^{19}F MRI, we determined that PPACK PFC NPs effectively inhibit microvascular coagulation in AKI, as evidenced by reduced accumulation of particles trapped by the ongoing clotting process, which suggests a new strategy for treating and evaluating kidney endothelial damage with thrombin targeted ^{19}F MRI.

7.2 Future works

7.2.1 Applications of "relaxation switch"

The "Relaxation switch" phenomenon first reported in this work could serve as a new approach to evaluate the uptake and processing of PFC NP by myriad tissues. By measuring ^{19}F T1 of paramagnetic PFC NP, one might dynamically track the intracellular processing and disposition of these particles. In many applications, it is important but difficult to identify whether PFC NPs accumulate in intracellular environments or only are trapped locally in the extracellular matrix: if processed rapidly intracellularly, the "relaxation switch" approach could offer more direct insights into such cell processing mechanisms.

7.2.2 Tracking multiple biomarkers *in vivo*

The multi-chromatic ^{19}F technique could be readily applied to several clinically relevant disease models to elucidate the presence of multitudinous biomarkers. For example, in the coagulation process, thrombin cleaves fibrinogen to fibrin, which deposit in thrombi along with platelets that are activated by thrombin. Many thrombin-inhibiting drugs, including the PPACK PFC NP that was investigated in this dissertation, diminish the coagulation process by actively binding to and irreversibly inactivating thrombin. Therefore, to better evaluate the treatment effect and investigate the clotting pathology, it might be helpful to quantify both the presence of

the anti-thrombin drugs and the molecular target itself, fibrin, in the clot, which would facilitate pharmacokinetic and pharmacodynamic assessment over time. Such applications could be realized in a non-invasive manner by combing the multi-chromatic ^{19}F imaging technique with fibrin-targeted PFC NPs and anti-thrombin PFC NPs which are already available.

7.2.3 Relation between cellular pO_2, tissue pO_2 and vascular pO_2

Because of the relatively large size of PFC NPs, which remain intravascular, the oxygenation measurements reported in this dissertation actually represent the pO_2 in micro and macro vasculature. However, because of the limited diffusivity of O_2 in biological tissues, the pO_2 in soft tissues remote from the flowing blood supply could be dramatically different from vascular oxygen levels. Likewise, local interstitial pO_2 also would exceed intracellular pO_2. For example, in many tumor models, most cancer cells might function under highly hypoxic environment especially in under-perfused regions. However, many observations have suggested that intravascular pO_2 in tumor tissue might be even higher than in normal microvasculature; possibly due to the special arrangement of blood vessels in solid tumors that hinders effective diffusion of O_2 from blood to hypoxic tumor tissues. It is possible then by using different PFC NPs to label tumor cells themselves, tumor vasculature, and extracellular tissue space, we could fully delineate the pO_2 differences in various compartments by imaging each PFC NP component individually.

7.2.4 Dynamic monitor of functional change in AKI kidneys

We have demonstrated the feasibility of using ^{19}F MRI to evaluate endothelial damage in AKI kidneys. As a next step, it would be germane to perform follow-up imaging studies at different time points after the initial surgery to fully map out the recovery process. Also,

investigation of more severe extents of injury by extending the ischemia time could be useful for developing methods more predictive of ultimate recovery or failure.

7.2.5 *In vivo* evaluation of treatment effect of PPACK NP for AKI

We also demonstrated *in vivo* ^{19}F functional imaging of ischemia-reperfusion injured kidney and *ex vivo* ^{19}F imaging for evaluating the treatment effect of PPACK NP on injured kidneys. Going forward, it would be critical to perform *in vivo* ^{19}F MRI to evaluate treatment effects in this disease model. In particular, delivering one PFC NP as drug delivery vehicle and a different type of PFC NP as a contrast agent could utilize multi-chromatic ^{19}F MRI techniques to generate both a parametric mapping of renal microcirculation and quantitative readout of the concentration of the anti-thrombosis drug.

7.2.6 Combining ^{19}F oxygenation and ^{1}H phase contrast imaging for oxygen consumption measurements

The new ^{19}F BESR sequence might find other uses for measuring blood oxygenation in large blood vessels. For example, in combination with ^{19}F oxygenation mapping, ^{1}H phase contrast angiography could provide a quantitative estimate of blood velocity. Together, the pO_2 and blood flow information would allow the calculation of tissue oxygen consumption, which is an important metabolic index of organ viability and functionality. This technique could be tested in brain, lung, kidneys, heart and other organs for proof of concept, under normoxic and ischemic conditions.

7.2.7 Combining VCAM targeted scheme with PPACK NP for targeted imaging and treatment

It is known that the interplay between inflammation and coagulation plays a pivotal role in the persistence of renal endothelial damage in AKI. By functionalizing anti-thrombin PPACK NP with an anti-VCAM-1 peptide, we might enhance the focal accumulation of therapeutic PPACK NPs in inflammatory vessels that manifest upregulated VCAM-1 as a part of the inflammatory process. The VCAM-1 targeted PPACK NP might be especially beneficial for therapy of evolving AKI, because a large component of the inflammatory responses ensues after reperfusion. Again, *ex vivo* ^{19}F quantification and *in vivo* functional ^{19}F imaging techniques might prove useful for following the treatment effect of this new nanodrug approach.